CZECH TECHNICAL UNIVERSITY IN PRAGUE

Faculty of Nuclear Sciences and Physical Engineering

Department of Physics

Master thesis

Study of the top quark in the experiment ATLAS

Bc. Ota Zaplatílek

Supervisor: Mgr. Marek Taševský, Ph.D.

Consultants: RNDr. Roman Lysák, Ph.D.; Ing. Petr Jačka

Praha, 2019

ČESKÉ VYSOKÉ UČENÍ TECHNICKÉ
V PRAZE
Fakulta Jaderná a Fyzikálně Inženýrská
Katedra Fyziky

Diplomová práce

Studium top kvarku v experimentu ATLAS

Bc. Ota Zaplatílek

Vedoucí práce: Mgr. Marek Taševský, Ph.D.

Konzultanti: Mgr. Roman Lysák, Ph.D.; Ing. Petr Jačka

Prague, 2019

NASCANOVAT PODEPSANE ZADANI A ULOZIT DO DVOU EPS SOUBORU ZADANI1.EPS a ZADANI2.EPS

NASCANOVAT PODEPSANE ZADANI A
ULOZIT DO DVOU EPS SOUBORU
ZADANI1.EPS a ZADANI2.EPS

Prohlášení:

Prohlašuji, že jsem svou diplomovou práci vypracoval samostatně a použil jsem pouze podklady (literaturu, software, atd.) uvedené v přiloženém seznamu.

Nemám závažný důvod proti užití tohoto školního díla ve smyslu 60 Zákona .121/2000 Sb., o právu autorském, o právech souvisejících s právem autorským a o změně některých zákonu (autorský zákon).

V Praze ....

Title: **Study of the top quark in the experiment ATLAS**

Author: Bc. Ota Zaplatílek

Specialization: Experimental nuclear and particle physics

Sort of project: Master thesis

Supervisor: Mgr. Marek Taševský, Ph.D
Consultants: RNDr. Ronan Lysák, Ph.D; Ing. Petr Jačka

Abstract: The master thesis deals with properties of the top quark and briefly describes the measurement of the $t\bar{t}$ pair production in the so called all-hadronic decay channel at 13 TeV in proton-proton collisions using data collected by the ATLAS experiment at LHC. The measurement is based on the boosted topology when all decay products of the $t\bar{t}$ system can be collected by only two jets with large radii R. The main task of this thesis is an implementation of the so called re-clustering procedure with the aim to improve systematic uncertainties of the top quark measurements. The method of reconstructing jets with large radii ($R \sim 1.0$) is based on clustering jets with small radii ($R \sim 0.4$). Since small-R jets usually have smaller systematic uncertainties than the large-R jets, one expected an improvement in this respect for re-clustered large-R jets. This thesis documents that both the total systematic uncertainty and the dominant one, the so called jet energy scale, have decreased by $10-20$ % in all studied variables, when large-R jets are re-clustered using small-R jets. Also a better agreement of Monte Carlo predictions with data was achieved for re-clustered jets. The second task of this thesis was to compare Monte Carlo predictions with a signal of New Physics with data to see if a better description is attained. By studying Pythia8 predictions for several mass points of an implemented hypothetical Z' boson which is predicted to decay fully hadronically as our studied signal, we conclude that adding this signal of New Physics on top of the Standard Model prediction does not improve the agreement with data.

Key words: top quark, $t\bar{t}$ system, Z' boson, all-hadronic decay channel, jet, large-R jet, re-clustering

Název práce: **Studium top kvarku v experimentu ATLAS**

Autor: Bc. Ota Zaplatílek

Zaměření: Experimentální jaderná a částicová fyzika

Druh závěrečné práce: Diplomová práce

Vedoucí práce: Mgr. Marek Taševský, Ph.D
Konzultanti: RNDr. Ronan Lysák, Ph.D; Ing. Petr Jačka

Abstrakt: Tato diplomová práce pojednává o vlastnostech top kvarku, zvláště pak o měření párové produkce top-antitop v plně hadronovém kanále při těžišťové energii 13 TeV v proton-proton srážkách na experimentu ATLAS. Měření využívá tzv. boostované topologie, kdy je možné obsáhnout veškeré rozpadové produkty $t\bar{t}$ systému do dvou jetů s velkými poloměry. Cílem práce je implementovat do již existujícího frameworku nový přístup k konstrukci velkých jetů ($R \sim 1.0$), tzv. re-clustering, a následně prozkoumat vliv re-klastrovaných jetů na systematické chyby měření v uvedené fyzikální analýze. Re-klastrovací metoda je založena na aplikaci anti-k_t algoritmu na již existující jety s malými poloměry ($R \sim 0.4$). Protože malé jety mívají obvykle nižší systematické chyby něž jety velké, pak můžeme očekávat zlepšení systematických chyb v případě velkých re-klastrovaných jetů. Tato práce dokumentuje pokles celkové i dominantní systematické neurčitosti spojené s jet energy scale velkých re-klastrovaných jetů. Jmenované nejistoty se snížily o 10 – 20 % u všech studovaných veličin. Re-klastrované jety dále poskytují lepší soulad mezi daty a predikcí. Dále je zde uvedena studie, která uvažuje rozpad hypotetického Z' bosonu na dvojici top-antitop v plně hadronovém kanále jako aditivní signál Nové Fyziky ke stávající predikci $t\bar{t}$ událostí, zda lze dosáhnout lepší shody mezi daty a predikcí. Studie obsahuje srovnání několika hmotnostních vzorků Z' bosonu generovaných MC generátorem Pythia8. Při zohlednění signálu, který obsahuje Novou Fyziku Z' bosonu, k predikci Standardního Modelu nezískáváme lepší souhlas mezi daty a predikcí.

Klíčová slova: top-kvark, $t\bar{t}$ system, Z' boson, plně hadronový rozpad, jet, jety s velkými poloměry, re-clustering

Acknowledgement

I would like to express my gratitude to all people who supported me and gave me an opportunity to complete this thesis. My profound thanks go to my supervisor Marek Taševský for his willingness, patience, understanding and text correction. I would líke to thank to my consultants Roman Lysák and Petr Jačka for their technical support.

Contents

1 The Standard Model of particle physics **11**

1.1 The cross-section in quantum field theory . . . 12

1.1.1 The S matrix element . . . 13

1.1.2 The decay rate and the cross section . . . 13

1.1.3 The invariant amplitude $\mathcal{M}_{fi}$ . . . 15

1.2 Introduction to quantum chromodynamic . . . 17

1.2.1 QCD Lagrangian . . . 17

1.2.2 Additional gluon emission . . . 18

1.2.3 The running coupling parameter . . . 18

1.2.4 Color number . . . 19

1.2.5 String hadronization model . . . 20

1.3 Top quark physics . . . 20

1.3.1 Top quark prediction . . . 21

1.3.2 Top quark decay . . . 21

1.3.3 Top quark production . . . 23

1.4 Variables in high energy physics . . . 23

2 LHC and ATLAS detector **25**

2.1 Large hadron collider . . . 25

2.2 ATLAS detector . . . 26

2.2.1 Inner detector . . . 27

2.2.2 Calorimeters . . . 27

2.2.3 Muon spectrometer . . . 27

2.2.4 Trigger system . . . 28

3 Data analysis techniques **29**

3.1 Theory of jets . . . 29

3.1.1 Jet algorithms . . . 29

3.1.2 Trimming . . . 31

3.2 Unfolding . . . 31

3.2.1 Motivation for the unfolding procedure . . . 31

3.2.2 The Bayesian theorem . . . 33

3.2.3 Bayesian iterative unfolding . . . 33

3.2.4 Fiducial cross section at the experiment . . . 35

3.3 Jet and jet substructure variables . . . 35

3.3.1 Jet mass . . . 35

3.3.2 k_t splitting scale . . . 35

3.3.3 N-subjettiness τ_N . . . 36

3.3.4 Top tagging . . . 36

3.3.5 B-tagging . . . 37

3.4 Background estimation for $t\bar{t}$ production . . . 37

3.4.1 Multijet background estimation . . . 37

3.4.2 ABCD method in 16 regions . . . 38

4 Measurement of all-hadronic $t\bar{t}$ differential cross section **41**
4.1 Event selection 41
4.1.1 Data selection criteria 41
4.1.2 Particle level definition 42
4.1.3 Data modelling and the background estimation 43
4.2 Systematic uncertainties 44
4.2.1 Object reconstruction and calibration 44
4.2.2 Signal modelling uncertainties 44
4.2.3 Propagation of systematic uncertainties 44
4.3 Detector level plots 44
4.4 Analysis of re-clustered jets 47
4.4.1 The re-clustering 47
4.4.2 The selection criteria modifications 47
4.4.3 Comparison of plots at detector level 49
4.4.4 Comparison at particle level 50
4.4.5 Comparison of systematic uncertainties at particle level 51

5 Z' sample analysis **63**

6 Summary **69**

Chapter 1

The Standard Model of particle physics

The Standard Model of particle physics describes our picture about the structure of matter at the most elementary base very successfully. This fundamental theory includes three of four well known fundamental interactions: strong, weak and electromagnetic interaction. Such interactions are described by a renormalised quantum field theory with gauge invariance. Unlike the gravity, which is not included in the Standard Model.

Nowadays it is possible to study the quantum processes at a scale of 10^{-18} m. Considering objects at such short dimension and low masses of elementary particles in the Standard Model, gravity can safely be neglected. Let us note, however, that gravity has to be considered for description of quantum effects at the Planck scale, which is $l_P = 1.616 \times 10^{-35}$ m. In other words, gravity is necessary for description of quantum objects at an energy scale $\sim 10^{19}$ GeV. Such an energy is almost 15 orders of magnitude higher than the maximum central mass energy reached at the LHC accelerator. Note that the most energetic particles observed on the Earth had energies $\sim 10^{11}$ GeV. Such particles are coming probably from the outer universe approximately once a century. Consequently, such advanced theories like quantum gravity can not be verified experimentally on the Earth, while Standard Model underwent numerous stringent tests.

Let us start with the description of the elementary particles in the Standard Model. All those particles are shown and shortly described in Fig 1.1. There are three generations of quarks and leptons, which interact with intermediate gauge bosons γ, $W^{\pm}$, Z^0, g. The Higgs boson H is presented, too. All mentioned elementary particles are not only predicted by the theory, but also verified experimentally.

There are three charged massive leptons (e^-, μ^-, τ^-), three neutral massless neutrinos $(\nu_e, \nu_\mu, \nu_\tau)$ and the corresponding antiparticles in the Standard Model. The presented leptons can be put together to three lepton generations with similar properties:

$$\begin{pmatrix} e \\ \nu_e \end{pmatrix}, \begin{pmatrix} \mu \\ \nu_\mu \end{pmatrix}, \begin{pmatrix} \tau \\ \nu_\tau \end{pmatrix}.$$

Since the spin magnitude of all the above mentioned leptons is $s = \frac{1}{2}$, they can be also classified as fermions, which follow the Pauli's exclusion principle. The up-type massive leptons carry a negative electric charge, consequently they interact by electromagnetic interaction. Further, all the leptons interact weakly but not strongly. The measurement of partial decay width of Z^0 boson supports the existence of three possible neutrinos as well as three lepton generations in the Standard Model.

The Standard Model predicts neutrinos as massless. However it is observed, that the neutrinos can change its nature into another neutrino in lower lepton generation. This phenomenon is called the neutrino oscillation. In addition, the shape of the final area of energetic spectra of the electron from the β-decay, so called Curie plots, also supports the ideas of massive neutrinos.

Let us continue with the quarks. There are six quarks in the Standard Model namely (u, d, c, s, t, b) and corresponding anti-quarks. All quarks dispose with spin magnitude of $\frac{1}{2}$. All of them can also be categorized to three generations similarly as the leptons.

$$\begin{pmatrix} u \\ d \end{pmatrix}, \begin{pmatrix} c \\ s \end{pmatrix}, \begin{pmatrix} t \\ b \end{pmatrix}$$

All quarks are subject to the electromagnetic, weak as well as strong interaction. Quarks can be merged together to compose particles called hadrons. A meson arises combining a quark with an anti-quark and similarly baryons can be born from three quarks. Since quarks interact electromagnetically, they carry an electric charge. A fractional electric charge was introduced for up-type quarks $\frac{2}{3}$ and $-\frac{1}{3}$ for down-type quarks because of the integer electric charge of the hadrons. Such a choice of quark electric charges was verified by measurement. Further, multiple bound states of the same quarks were observed, for example Δ^{++} baryon, which involves three up quarks (u, u, u). Consequently, it is necessary to introduce a new degree of freedom for quarks, the color charge, because of the Pauli's exclusion principle.

Additionally, there are massless gluons, which mediate the strong interaction of color charged particles. Each gluon carries one of eight physical combinations of color and anti-color. Gluons do not have any electric charge and its spin is unity. The gluon is able to change the color charge of the quark because of the gluon color-anti-color charge despite the color charge is conserved in the strong interaction.

The four particles in the last but one column in Fig. 1.1 are gauge bosons: while massive Z and W bosons mediate electro-weak interactions responsible for particle dacys and dominant at middle-range distances, massless photon γ mediates electromagnetic interaction dominant at large distances, gluon g is a mediator of the strong force active only at very small distances. The last ingredient of the Standard Model is the scalar Higgs boson H with zero electric and color charge. The Higgs boson represents a key particle for explanation of the origin of mass in the theory. Thanks to the non-zero Higgs mass and the Higgs mechanism, masses of almost all fundamental fermions and bosons can be explained. The discovery of the Higgs boson is dated to 2012 by CMS and ATLAS experiments at the LHC, only 50 years after the theoretical prediction by P. Higgs [1], R. Brout and F. Englert [2].

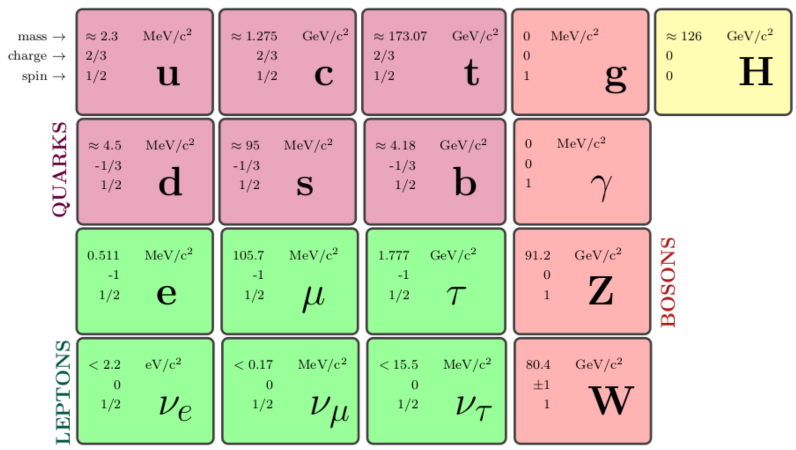

Figure 1.1: The elementary particles in the Standard Model with their basic properties: invariant mass, electric charge in the units of the elementary charge e and the spin magnitude.

1.1 The cross-section in quantum field theory

The quantum mechanic as well as the quantum field theory is based on probability interpretation of the studied process. The fundamental basis of common used variables will be introduced in this section.

1.1.1 The S matrix element

The section introduces a basic measurable quantity in the quantum field theories[1], the cross section.

The derivation of the cross section is based on the computation of the transition probability. Thus, it is necessary to evaluate the form of the time evolution operator first in a suitable Dirac picture. The time evolution operator $U_D(t,t_0)$ propagates the initial quantum field $|i> \equiv |i(t_0)>$ at time t_0 to another time t as $|i(t)> = U_D(t,t_0)|i>$. So $|i(t)>$ represents an outgoing state. Now, let us assume a state $|f>$ as an expected final state. Then $|<f|U_D(t,t_0)|i>|^2$ determines the probability, that the field particles $|i>$ will interact with another field in time interval from t_0 to t and the final state $|f>$ will be observed. However, the interaction can happen at any time, not only in $<t_0,t>$, thus it is introduced the S operator as $S = U(+\infty,-\infty)$. The definition of the S matrix operator also employs ingeniously the quantised field variables, which behave as free at the initial time $t_0 = -\infty$. Now, the S matrix element S_{fi} can be defined.

$$S_{fi} = <f|S|i> = <f|U_D(+\infty,-\infty)|i> = <f|i(+\infty)> \tag{1.1}$$

Let us consider the form of the Dirac time evolution operator $U_D(t,t_0)$ or the S operator respectively, which was obtained as a solution of an operator integral equation for a time evolution operator at the Dirac picture. The solution of S matrix can be expanded to a perturbative Dayson series, so the S matrix element S_{fi} can be recast as follows.

$$S_{fi} = <f|T\exp\left(-i\int dt H_{int}(\vec{x},t)\right)|i> \tag{1.2}$$

$$= <f|T\exp\left(i\int d^4x\mathcal{L}_{int}(x)\right)|i> \tag{1.3}$$

$$= \delta_{fi} + i\int d^4x <f|\mathcal{L}_{int}(x)|i> + \frac{(i)^2}{2!}\int\int d^4x d^4y <f|T\left[\mathcal{L}_{int}(x)\mathcal{L}_{int}(y)\right]|i> + \ldots \tag{1.4}$$

The second expression in eq. (1.4) was derived using an assumption that the interaction Hamiltonian $H_{int} = \int d^3x\mathcal{H}_{int}(x)$ is equal to interaction Lagrangian $L_{int} = \int d^3x\mathcal{L}_{int}(x)$ up to the sign. This is mostly performed in the Standard Model. Further, a time ordering product T was introduced in eq. (1.4). It becomes clear that the interaction Lagrangian becomes crucial for quantum field theories.

Further, if one wants to compute the transition probability, one has to square the expression in eq. (1.4), which leads to several technical troubles considering the presence of time and space infinite intervals and the divergent expression at higher order of perturbative series. However it can be solved by the regularisation and the renormalization procedure. The basic ideas of those procedures will be mentioned later in 1.1.3 section.

1.1.2 The decay rate and the cross section

In this section two standard variables in the field theories: the decay rate and the cross section are discussed. Both of them are related closely to the squared matrix elements $|S_{fi}|^2$, which was introduced previously.

First we define the transition probability for the final state particles with a three momenta in interval $(\vec{p}_f, \vec{p}_f + d\vec{p}_f)$. There are $\tilde{n}_f = \frac{Vd^3p}{(2\pi)^3}$ possible states for each considered final state particle in such momentum interval. So, the production probability can be expressed as

$$dP_{fi} = |S_{fi}|^2 \cdot \prod_f \frac{V \cdot d^3p_f}{(2\pi)^3}, \tag{1.5}$$

[1] There are many field theories, but not all of them are used in the Standard Model.

where the product runs over all considered final state particles. Let us define the decay rate dw_{fi} representing a production probability per a unit time.

$$dw_{fi} = \frac{dP_{fi}}{T} \tag{1.6}$$

Further, an integrated decay rate is identified with the decay width Γ, which is quite often measured for the decaying particles, especially the partial decay width Γ_j for the considered decay channel and its relative probability P_i(decaying particle in ith channel) as

$$P_i(\text{decaying particle in } i\text{th channel}) = \frac{\Gamma_i}{\sum_j \Gamma_j}, \tag{1.7}$$

where, the index j runs over all possible decay channels. Consequently, the full decay width Γ is denoted here as a sum $\sum_j \Gamma_j$.

The cross section can be quantified as a ratio of the number of scattering events N times the production probability per unit time dw_{fi} to a density flux of incident particles as follows.

$$d\sigma = \frac{\#\text{ of scattering events per unit time}}{\text{density flux of incident particles}} = \frac{N dw_{fi}}{\frac{N}{V}|\vec{v}_1 - \vec{v}_2|} \tag{1.8}$$

It is expected here that velocities of both initial particles $\vec{v}_1$, $\vec{v}_2$ are parallel and they are opposite to each other. Now, let us take all together (using eq. (1.8), eq.(1.6), eq.(1.5) and including the S-matrix elements in eq. (1.4) involving the interaction Lagrangian $\mathcal{L}_{int}$ as a function of field variables) and let us integrate over space-time coordinates (which have an origin in the exponent of the exponential function in the S-matrix element presented in eq.(1.4)) to derive the cross section $d\sigma^{2\to n}$ for a process involving n particles as follows.

$$d\sigma_{2\to n} = K \cdot \frac{1}{|\vec{v}_1 - \vec{v}_2|} \frac{1}{2E_1} \frac{1}{2E_2} \cdot |\mathcal{M}_{fi}|^2 \cdot (2\pi)^4 \delta^{(4)}(P_1 + P_2 - \sum_{f=3}^{n} P_f) \cdot \prod_{f=3}^{n} \frac{d^3 p_f}{(2\pi)^3 2E_f} \tag{1.9}$$

The factor $\frac{1}{|\vec{v}_1 - \vec{v}_2|} \frac{1}{2E_1} \frac{1}{2E_2}$ is the so called flux factor, because it describes the flux of two initial particles going against each other. Those initial particles dispose with the energy and velocity E_1, $\vec{v}_1$ or E_2, $\vec{v}_2$, respectively. Further the square of the invariant amplitude $|\mathcal{M}_{fi}|^2$ involves kinematics of the considered process. The invariant amplitude will be discussed in more detail in next 1.1.3 subsection. Further, there is a four-dimensional delta function. The P_1, P_2 describe the four-momenta of the initial state particles and similarly P_f denotes the four-momentum of the final state particle with $f = 3, 4, 5 \ldots n$. The delta function $\delta^{(4)}(P_1 + P_2 - \sum_{f=3}^{n} P_f)$ describes the conservation law of energy and three-momenta in the interaction. Finally, there is a product of three-momentum differentials $d^3 p_f$ of all final state particles. The expression $\frac{dp_f}{(2\pi)^3}$ describes one quantum in the momentum space and $\frac{1}{2E_f}$ factor comes from the normalisation of the wave function. Finally, there is a K factor, which is almost 1. It acquires other values only when some of final states are identical, then $K = \prod_{r=1}^{k} \frac{1}{n_r!}$, where n_r is a number of identical particles of the rth kind.

It can be seen, that the cross section in eq. (1.9) has a dimension of [area^2]. Since, the common units are too huge, new one was introduced, the barn 1 b= 10^{-28} m^2 by E. Fermi. The barn represents an area of atom nucleus, however it is still quite large for rare processes such as a top quark decay, so the pb $=10^{-12}$b are most used in the thesis.

The formula in eq. (1.9) is completely general so it can be easily adapted to special cases. For example, the case of proton-proton cross section at the LHC, where protons are accelerated and collided parallel to each other at the main experiments. The total proton-proton cross section σ_{pp} is given by eq. (1.10) as a convolution of hard process cross section $d\sigma_{2\to n}$ and the parton distribution functions. The presented parton distribution functions $f_a^{p_1}(x_1, \mu_F)$ describe the probability, that there is a parton[2] a with the momentum fraction x_1 in the

[2]The terminology of the parton was introduded by R. Feynman and it represents the notation for intrinsic particles in nucleons, the quarks and gluons simultaneously.

proton p_1. The parton distribution functions are determined experimentally, therefore they depend on the factorisation scale μ_F, too. The parton distribution functions for gluon, quarks and anti-quarks in a proton can be seen in Fig. 1.2 at low ($Q^2 = 10$ GeV^2) and high ($Q^2 = 10^4$ GeV^2) factorization scales $\mu_F = Q^2$. Considering all possible partons a resp. b in the proton with arbitrary momenta x_1, resp. x_2, one can get the following proton-proton cross section formula σ_{pp}.

$$\sigma_{pp} = \sum_{a,b} \int_0^1 dx_1 dx_2 f_a^{p_1}(x_1, \mu_F) f_b^{p_2}(x_2, \mu_F) d\sigma_{ab\to n}(s, u, t, x_1, x_2, \mu_F) \tag{1.10}$$

The hard scattering process in QCD with the cross section $d\sigma_{ab\to n}$ can be computed using the formula in eq. (1.9), which depends on the set of Lorenz invariant Mandelstam variables u, t, s, momenta of the initial partons and the factorisation scale μ_F in general.

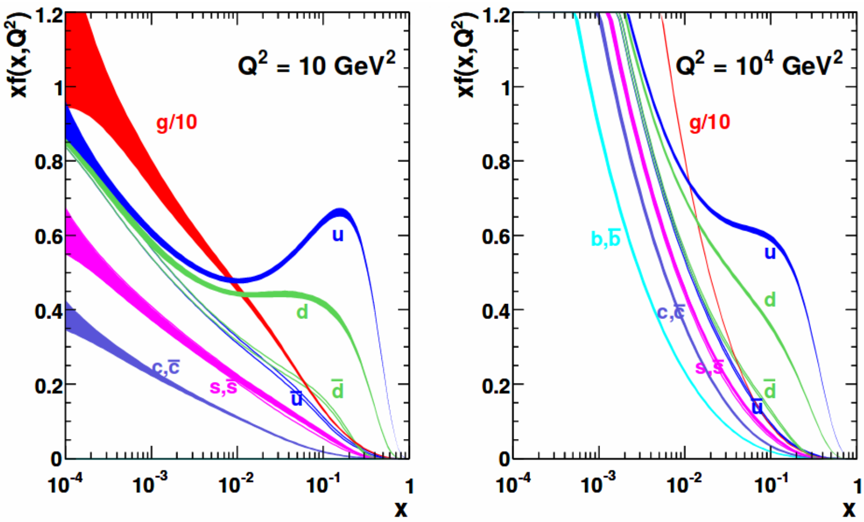

Figure 1.2: Parton distribution functions in proton for low factorization scale $Q^2 = 10$ GeV^2 and high factorization scales $Q^2 = 10^4$ GeV^2, taken from [16].

1.1.3 The invariant amplitude $\mathcal{M}_{fi}$

The invariant amplitude $\mathcal{M}_{fi}$ in eq. (1.9) caries a legacy of the perturbative expansion of the Dyson series in eq.(1.4). The basic ingredient for $\mathcal{M}_{fi}$ calculation at appropriate perturbative order is the interaction Hamilotonian, which is often equal to the interaction Lagrangian $\mathcal{L}_{int}$ up to the sign. The interaction Lagrangian $\mathcal{L}_{int}$ further provides our physical point of view of the interaction.

The exact computation of $\mathcal{M}_{fi}$ in the cross section $d\sigma$ or the partial decay width Γ_i can be simplified significantly by an introduction of Feynman rules and the set of Feynman diagrams. Examples of the Feynman diagrams are shown in Figs. 1.3 and 1.6. Each line in the Feynman diagram corresponds to an associated quantum field in the interaction Lagrangian $\mathcal{L}_{int}$. Basically, there are initial and final state particles as the input or output lines in the Feynman diagrams. However, intrinsic lines can appear in the higher orders of perturbation calculus. Such intrinsic lines represent intermediate fields, which mediate the interaction, thus they are not observed at the experiment. They are called propagators. The field variables in the Feynman diagram often enter and further go out from the crucial points so called interaction vertices. The algebraic structure connected with the vertex can be also derived from the interaction Lagrangian $\mathcal{L}_{int}$. Let us note, that any Feynman diagram always involves one vertex for each order of the perturbation expansion of the Dayson series in eq.(1.4). Then a set of Feynman diagrams can be constructed at the appropriate perturbation order using the set of initial, final state particles and the vertices and propagators. The invariant amplitude of the considered Feynman diagram can be then evaluated using so called Feynman rules. The full invariant amplitude is further obtained as a sum of all Feynman diagrams.

Now, let us mention here at least one Feynman rule from the whole set of Feynman rules. An advanced rule for Feynman diagrams, which involve an intrinsic closed loop of virtual particles. Such loops appear at higher order of perturbative calculus. The rule says:

1.) let us construct the algebraic factor from the vertex factors and the propagators of all associated field variables appearing in the closed loop

2.) let us integrate the algebraic factor obtained from 1.) over all possible momenta associated with the independent field variables in the closed virtual loop

Following this Feynman rule, one arrives at ultra-violet divergencies in the perturbative calculations. An example of the ultra-violet divergences can be found in the photon self-energy correction in spinor QED. Such a correction represents a connection of the closed fermion loop to a photon propagator. The Feynman diagram of the photon self-energy is shown in Fig. 1.3. Since, the algebraic vertex factor in spinor QED is equal to $-ie\gamma_\mu$ and the fermion (e.g. electron) propagator $\frac{1}{\not{q}-m}$, where $-e$ represents the electric charge of electron, γ_μ the gamma matrix, $\not{q} = q_\mu \gamma^\mu$ with electron four-momenta q_μ and electron mass m. Using above mentioned QED vertex factor and fermion (electron) propagator the photon self energy correction $i\Pi_{\mu\nu}(q)$ can be constructed as follows.

$$i\Pi_{\mu\nu}(q) = (-ie)^2 \int \frac{d^4 l}{(2\pi)^4} Tr \left\{ \gamma_\mu \frac{1}{\not{l} - m} \gamma_\nu \frac{1}{(\not{q} - \not{l}) - m} \right\} \tag{1.11}$$

$$\sim \int l^3 \cdot \frac{1}{l} \cdot \frac{1}{l} dl \sim l^2 \tag{1.12}$$

Here, the quadratic ultra-violet divergence has appeared.

In summary, the ultra-violet divergence occurs as a consequence of the integration over very high momenta $l \to +\infty$. As will be shown later in section 1.2.2, another type of divergence, the so called infra-red divergence, may arise when the resulting formula has a negative power of momentum and we wish to integrate from values close to zero. Nevertheless all those divergences can be solved using the so called regularization and renormalization.

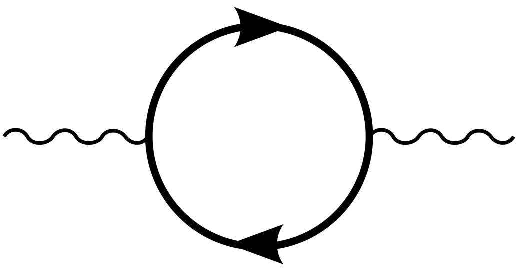

Figure 1.3: The Feynman diagram of the photon self-energy correction in QED.

The key idea of the procedure of regularization and renormalization lies in expressing the problematic divergent parts by unphysical parameters and further introducing new terms to the interaction Lagrangian, so called counter-terms. The counter-terms are designed to cancel the original unsuitable divergent parts of the matrix elements[3] by keeping the same structure of field variables but re-defining their constant parts (such as mass, electric charge, and couplings). The latter is also called "dressing" the original (undressed) objects.

[3]This is an idea of the so called Minimal subtraction scheme of the renormalization, but it is possible to subtract also other finite terms

1.2 Introduction to quantum chromodynamic

This theory describes our physical point of view of the strong interaction. The theory is based on a non-abelian $SU(3)_{color}$ gauge symmetry. The expression *chromos* comes from the Greek and it denotes a color, a newly introduced degree of freedom. The number of degrees of freedom N_c reflects the character of the color group, there are three possible color charges, which are denoted commonly as: red, blue and green. Thus, the strong interaction is mediated by the exchange of the color charge among the color particles. The color charge is carried by quarks and gluons where the latter also represent the intermediate gauge bosons of the strong interaction. The gluons are massless. Further the gluons carry both color and anti-color charge simultaneously. This is an important feature of QCD leading to the gluon self-interaction, unlike QED, the abelian gauge theory where photons are neutral and do not interact with each other.

1.2.1 QCD Lagrangian

The QCD Lagrangian is shown in the eq. (1.13). Here it is summed over quarks q, color index a and Lorentz index μ.

$$\mathcal{L}_{QCD} = \sum_q \left[i\bar{\psi}_q \gamma^\mu \left(\partial_\mu - ig_s \frac{\lambda^a}{2} A^a_\mu(x) \right) \psi_q - m_q \bar{\psi}_q \psi_q \right] + \mathcal{L}_{gauge} \tag{1.13}$$

The field function ψ_q represents here a three-component quark field distinguished by three possible color charges. There are two terms, the first introduces an interaction including quarks, whereas the second one, $\mathcal{L}_{gauge}$, contains kinematics of gluons.

The interaction among quarks and gluons was introduced using the principle of a covariant derivative in the first term in eq.(1.13). The form of the covariant derivative $D_\mu = \partial_\mu - ig_s \frac{\lambda^a}{2} A^a_\mu(x)$ has an origin in a requirement of the non-abelian gauge symmetry of the Yang-Mills fields. The gluon fields are presented here by $A^a_\mu(x)$, where the color index a runs from 1 to $N_c^2 - 1$. Consequently, there are 8 physical color gluons collected in one color octet for three possible colors $N_C = 3$. The matrices $\frac{\lambda^a}{2}$ denote generators of an appropriate color group and λ^a correspond to eight Gell-Mann 3×3 matrices. Further g_s denotes a coupling constant of the strong interaction. The second term in the squared brackets in eq.(1.13) describes a mass term of the quark.

The last term in eq. (1.13) it can be expressed as follows.

$$\mathcal{L}_{gauge} = -\frac{1}{4} G^a_{\mu\nu} G^{a\mu\nu}$$

$$= -\frac{1}{4} A^a_{\mu\nu} A^{a\mu\nu} - \frac{1}{2} g_s f^{abc} (\partial_\mu A^a_\nu - \partial_\nu A^a_\mu) A^{b\mu} A^{c\nu} - \frac{1}{4} g_s^2 f^{abc} f^{ajk} A^b_\mu A^c_\nu A^{j\mu} A^{k\nu} \tag{1.14}$$

Here again, we sum over repeating indices. $G^a_{\mu\nu}$ in eq.(1.14) corresponds to a gluon field strength tensor, which represents an analogue of the full anti-symmetric field strength tensor in QED $F_{\mu\nu}$, which describes an electric charged particle in electromagnetic fields. However, there is a significant difference: unlike QCD, the QED theory is connected with the abelian group $U(1)$. So, there are also so-called structure constants f^{abc} in QCD as a consequence of non-commutative generators of the color group $SU(3)_{color}$. Consequently, the $\mathcal{L}_{gauge}$ does not contain only the kinetic term $A^a_{\mu\nu} A^{a\mu\nu}$ (as in the case of QED), but there are new terms, as a consequence of the non-abelian structure. Thus, the gauge Lagrangian of QCD involves the terms proportional to three gluon fields $A^a_\mu(x)$ as it can be seen in the second term in eq. (1.14). Further, there is also the last term in eq. (1.14) involving four gluon fields. Consequently, the gluons are able to interact themselves forming a three-gluon vertex and four-gluon vertex, contrary to photons in QED.

All above discussed interactions of quarks and gluons are presented graphically in Fig. 1.4. Let us note here, that the QCD Lagrangian (1.13) also conserves the flavour as well as the parity unlike the Lagrangian of the weak interaction.

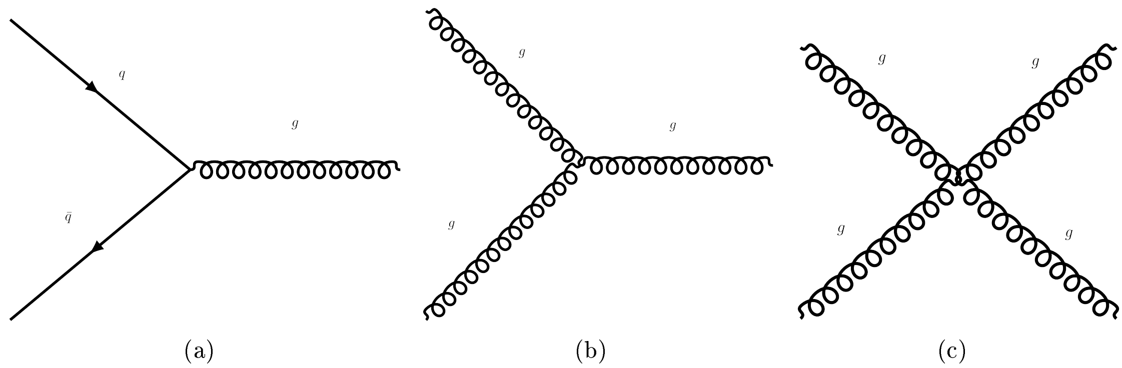

Figure 1.4: The interaction vertices generated by the Lagrangian $\mathcal{L}_{QCD}$ of the strong interaction: the quark anti-quark annihilation (a), gluon triple-vertex (b) and gluon four-vertex (c).

1.2.2 Additional gluon emission

All three QCD vertices as shown in Fig. 1.4 are important for a description of the initial and final state radiation, when the quark or the gluon can emit other gluons. It causes an additional gluon radiation, which represents another correction to the cross section calculus. However the additional gluon radiation may lead to infra-red and ultra-violet divergences, which can be seen in the following cross section formula for a gluon radiation from the quark.

$$d\sigma_{q\to qg} = \alpha_s \frac{C_F}{\pi} \frac{dE}{E} \frac{d\theta}{\sin\theta} \frac{d\phi}{2\pi} \tag{1.15}$$

Here, the cross section $d\sigma_{q\to qg}$ diverges for soft gluon emission with $E \to 0$ (infra-red divergence) and for the gluon emission at low angle $\theta \to 0$ (collinear divergence). Such effects are quite important when jet measurements are to be compared to theory predictions.

1.2.3 The running coupling parameter

The QED as well as QCD represent renormalizable field theories. It means, that there is a finite number of counter-terms to cancel all divergences in the invariant amplitude $\mathcal{M}_{fi}$ to all orders of the perturbative calculus. The existence of divergences was demonstrated on the photon-self energy in QED, and further the principle of the renormalization procedure was described briefly in 1.1.3 section. The final step of the renormalization turns to the redefinition of the undressed field variables, massed and charges to the dressed ones. Since, the coupling constant is proportional to square of the charge as $\alpha = \frac{e^2}{4\pi}$, the renormalization also leads to the evaluation of the so called running coupling constant $\alpha(Q^2)$ by eq. (1.16), which provides the information about the truth strength of the interaction.

$$\alpha(Q^2) = \frac{\alpha(Q_0^2)}{1 - B\cdot\alpha(Q_0^2)\ln\frac{Q^2}{Q_0^2}} \tag{1.16}$$

The running coupling parameter at a given squared transfer momentum Q^2 depends on the value of the coupling parameter at some initial value Q_0^2. The difference between the QCD and QED field theories is seen in the B parameter. Each of the theories predicts a different value for the B parameters:

$$B_{QED} = \frac{2}{3\pi}, \qquad B_{QCD} = -\frac{11N_c - 2N_f}{6\pi}. \tag{1.17}$$

Here, the N_c is the color number, $N_c = 3$ and N_f the flavour number. Consequently, the running coupling parameter $\alpha_{QCD}(Q^2)$ decreases with increasing momenta Q^2 for $N_f < 17$, unlike $\alpha_{QED}(Q^2)$. Let us note, that the Standard Model predicts six quarks, thus $N_f = 6$

[17], which will be discussed at the end of the section. The decreasing trend of the strong coupling parameter $\alpha_{QCD}(Q^2)$ also supports Fig. 1.5, which collects the information from different QCD processes.

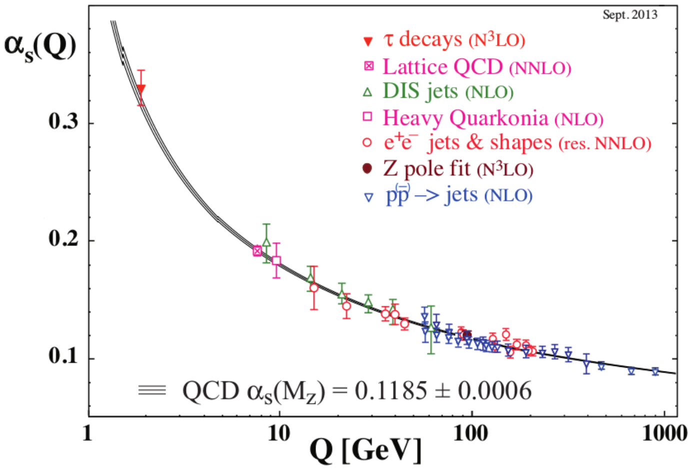

Figure 1.5: A collection of measurements of the running coupling parameter $\alpha_s(Q)$ at various Q points compared with calculations of $\alpha_s(Q)$ using eq. (1.16). Taken from [15].

This behaviour of $\alpha_{QCD}(Q^2)$ also reflects two other important QCD phenomena: asymptotic freedom and color confinement of strongly interacting objects with a color charge. The asymptotic freedom of quarks is seen at high energy scales Q^2 or in other words at low mutual distances of two considered quarks. Then $\alpha_{QCD}(Q^2)$ is too low so the strong force between two color objects is low, too. Thus, the quarks behave as free particles. However, the color-confinement of the quarks is observed at low scales Q^2 or at large mutual distances, respectively. Then $\alpha_{QCD}(Q^2)$ as well as the force between two color objects is so big that color objects cannot behave as free, on the contrary, they are forced to form a bound state of colorless objects: mesons and baryons.

These phenomena imply that partons exist like free particles immediately after the proton collision. However, they are not observed directly, because of the fragmentation of partons to hadrons and other particle, which are then detected in detectors.

Let us note, that the perturbative calculus posses a limited application at low Q^2, because of the divergences, which can no longer be regularized. Consequently, hadronization models or other approaches (e.g. lattice QCD) are applied at low Q^2 instead of the perturvative calculus.

1.2.4 Color number

The introduction of the new degree of freedom, the color charge, provides the whole spectrum of remarkable features of the strong interaction. The existence of color charge was postulated for the non-abelian gauge $SU(3)_{color}$ symmetry.

Examples of physical observables, which are proportional to N_C, are the integrated cross section of the electron-positron annihilation into two hadrons: $e^- + e^+ \to hadrons$ and the decay width of π^0 into two photons: $\pi^0 \to \gamma + \gamma$.

The cross-section $\sigma_{e^- + e^+ \to hadrons}$ can be calculated from the quantum field principles as it was described in 1.1 section. The dominant process is the $e^- e^+$ annihilation mediated by photon. Since, any guark pair can be expected in the final state, the cross section has to be proportional to the color number of appropriate quarks. In case of the pion decay width, the pion decays to two photons in the 3rd order of perturbative calculus involving a closed triangular fermion (quark) loop, consequently two $qq\gamma$ vertices are presented and both of them are proportional to N_C. In summary, the theory predicts

$$\sigma_{e^- + e^+ \rightarrow hadrons} \propto N_c, \qquad \Gamma_{\pi^0 \rightarrow \gamma + \gamma} \propto N_c^2$$

Such quantities were measured and color number was evaluated as $N_C = 2.99 \pm 0.12$. [18]

1.2.5 String hadronization model

The QCD theory works with color-rich physical objects, gluons and quarks. However, those physical objects are not stable and they hadronize. The hadronization can be understood as follows.

Let us assume a meson (a pair of quark and anti-quark, $q\bar{q}$) as a simple educative example. We can apply a lattice QCD calculation to evaluate a potential $V(r)$ for such a meson system as a function of a mutual distance r of the considered quark q and the anti-quark $\bar{q}$. There should be observed a coulomb potential $V(r) \sim -\frac{1}{r}$ at low r because of the electric charge of the quarks. Further, a linear potential at the higher distances r is observed. The linear potential $V(r) \sim r$ behaves as a string. Such an observation leads to the so called String model of the hadronization, which is used at low values of transition momentum Q^2 (or in other words at high r at the same time), where the perturbative QCD does not work. So, the linear string potential leads to an introduction of the color string, a gluonic force line, between the color-rich particles. The force of the color string does not decrease with increasing r like in QED according to section 1.2.3, but the force is rising equally with increasing r until a breaking point is reached, when the force is too high, then this color string is cut. Simultaneously if the potential attains a sufficient value, then it may participate in a new quark anti-quark pair formation from a vacuum. The new quark q is paired with the original anti-quark $\bar{q}$ and the new anti-quark $\bar{q}$ is connected to the interrupted color string similarly. Consequently, there are two mesons in the final state.

1.3 Top quark physics

The top quark represents the up-type quark in the 3rd quark generation. Its electric charge amounts to 2/3. The charge of the top quarks was measured experimentally as $0.64 \pm 0.02(\text{stat}) \pm 0.08(\text{syst})$.[7] Additionally, top quark represents the most massive fermion in the Standard Model, its pole mass was measured to be $m_t = 173.5 \pm 1.1$ GeV/c^2[3], which is approximately equal to a mass of the tungsten atom. The tungsten atom disposes with the size of $\sim 10^{10}$ m in comparison with almost point-like top quark. Further, the full decay width of the top quark is $\Gamma_{tot} = 2.0 \pm 0.5$ GeV [3], which means, that its mean life time is extremely short $\sim 10^{-25}$ s (compare with the mean life time of the b-quark[4], 10^{-13} s). Furthermore, the top quark does not create observable bound states, because of a typical required time for a hadron formation is at least two orders higher than top quark mean life time.[4] Thus it is possible to observe a bare quark. [5]

The large top mass is also responsible for large contributions to quantum loop corrections to electroweak observables. In addition the mass of the top quark and the Higgs boson are the two parameters that govern the shape of the Higgs potential at high energy, allowing to answer the fundamental question of the vacuum stability of our universe.[6] Consequently, the large top mass and especially its precise measurement, play a key role in explaining crucial questions in particle physics.

Last but not least, the large top mass also indicates a limited condition for a top quark systematic experimental research. In principle the top quark can be observed in high energy cosmic rays, however a detailed and systematic study can be performed only at accelerators. Nowadays there is only one device, which disposes with high enough energy for a such top quark research, the Large Hadron Collider (LHC).

[4]The b quark represent the second most massive quark in the Standard Model with mass $m_b = 4.18^{+0.04}_{-0.03}$ GeV [3].

1.3.1 Top quark prediction

The theoretical prediction of the 6th quark in the Standard Model relates closely to a detailed study of the processes at higher order of perturbative calculations. More precisely, with Feynman diagrams involving a virtual closed triangular fermion loop. Such processes can be described for example by Fig. 1.6. The presence of virtual closed triangular loop with

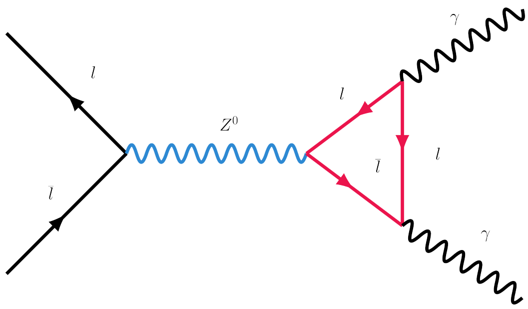

Figure 1.6: Feynman diagram involving a virtual closed triangular fermion loop.

one type of fermion leads to non-physical results. The invariant amplitude $\mathcal{M}_{fi}$ in such a process involves a linear divergence with the energy E and further such process causes a gauge dependent Glashow, Salam, Weinberg theory of electroweak interactions [8]. Those troubles can be resolved if one considers the loops involving all possible fermions. Then the total invariant amplitude leads to a formula, which is proportional to a sum of all fermion charges.

$$\mathcal{M}_{fi} \sim \sum_{fermion} Q_{fermion} \tag{1.18}$$

The above mention troubles can be solved by following this zero condition:

$$\sum_{fermion} Q_{fermion} = 0. \qquad [8] \tag{1.19}$$

Note that these calculations were done in times, when only four quarks u, d, s, c and four fermions $e^-, \mu^-, \nu_e, \nu_\mu$ were known. The zero equality can be verified easily considering the charges of all those fermions and three possible color states of the quark. However, the τ lepton was discovered in 1975, and the so called relation of closed generations in eq. 1.19 has become violated. It suggested an existence of other particles to satisfy the symmetry among the quarks and leptons. However, the condition presented in eq. 1.19 was not still fulfilled even when the b quark was discovered in 1977. Thus it was clear, that yet another quark has to exist to close the third generation of the quarks in the Standard Model. Those thoughts initiated the search for the top quark, which was discovered finally in 1995 by two independent experimental groups at $D0$ and CDF collaborations at the proton-antiproton Tevatron collider [9, 10].

1.3.2 Top quark decay

Contrary to the classical quantum mechanics the field theories are based on the Lagrangian formalism and therefore multi-particle processes can be described theoretically. The construction of the correct Lagrangian form represents one of the main tasks in the field theories. Nowadays, the theoretical construction is based on the symmetry principles (especially the Lorentz and the Gauge symmetry) with a unitarity requirement to reach a renormalizable theory, which further provides physical results of the observables such as the cross section, which does not involve any divergences.

Now, the charged current interaction Lagrangian for weak quark interaction will be introduced. Such an interaction is described as follows.

$$\mathcal{L}_{CC}^{quarks} = \frac{g}{2\sqrt{2}}(\bar{u}, \bar{c}, \bar{t})\gamma^{\mu}(1-\gamma_5)V_{CKM}\begin{pmatrix} d \\ s \\ b \end{pmatrix} W_{\mu}^{+} + h.c. \tag{1.20}$$

Here, the interaction of the up-type quarks u, c, t with the down one d, s, b, put in triplets is defined by eq. (1.20).The interaction is intermediated by the vector W boson of the weak interaction. The term $h.c.$ represents the hermitian conjugation, thus down-type quarks can change their nature to up-type quarks and vice versa. In other words, the weak interaction does not conserve a flavour, natural character of the quarks. Further g factor corresponds to the coupling constant and γ^{μ} are the Dirac gamma matrices 4×4. The index μ denotes the Lorentz index $\mu = 0, 1, 2, 3$ and further the γ_5 represents another "Dirac matrix", which anticommutes with all γ^{μ}, $\gamma_5 = -i\gamma_0\gamma_1\gamma_2\gamma_3$. The algebraic expression $1 - \gamma_5$ represents a typical character of the weak interaction, which does not conserve the parity. Consequently only left-handed particles and right-handed anti-particles are observed in the weak interactions. The most important term in eq. (1.20) is the V_{CKM} matrix, so called Cabibbo-Kobayashi-Maskawa (CKM) matrix.

The CKM matrix describes the mixing parameters of quarks. In fact it generalises the Cabibbo mixing model of three type quarks u, d, s and Glashow–Iliopoulos–Maiani (GIM) mechanism for four quarks u, d, s, c. The CKM matrix also plays an important role in explanation of CPT symmetry violation (combined discrete symmetry of charge-conjugation, parity and time-inversion) in weak interactions as well as in an introduction of the 3rd generation of quarks. Now, we will be interested in the numerical values of the CKM matrix elements, which were measured experimentally as follows.

$$V_{CKM} = \begin{pmatrix} V_{ud} & V_{us} & V_{ub} \\ V_{cd} & V_{cs} & V_{cb} \\ V_{td} & V_{ts} & V_{tb} \end{pmatrix} \approx \begin{pmatrix} 0.9745 & 0.2253 & 0.0041 \\ 0.225 & 0.986 & 0.041 \\ 0.0084 & 0.040 & 0.9991 \end{pmatrix} \tag{1.21}$$

The square of the individual CKM matrix element describes the probability of the transition between two considered quarks. Looking at the last line of the CKM matrix, it is clear, that the top quark decays almost only to the b quark, since the transition probability of the top quark into d and c quarks are negligible. This statement can be also expressed using the branching ratio for decaying top quark

$$\frac{\Gamma(t \to Wb)}{\Gamma(t \to Wq)} = \frac{|V_{tb}|^2}{|V_{td}|^2 + |V_{ts}|^2 + |V_{tb}|^2} = 0.99830^{+0.00004}_{-0.00009}, \qquad [3] \tag{1.22}$$

where the shorthand notation was used: q represents here all down-type quarks d, s, b.

Further, let us consider an unified Lagrangian of electromagnetic and weak interactions for the top quark decay. Such an interaction Lagrangian involves the interactions mediated by photon γ and Z boson. Such Lagrangian disposes with flavour-diagonal structure, consequently it does not violate the flavour.[8] So, the flavour-changing decays involving neutral-current of the top quark are suppressed and are predicted only in higher perturbative orders. The branching ratio for Z boson and photon were measured, too. However only the upper limits for a flavour-changing decays were measured:

$$\frac{\Gamma_{t\to\gamma+\tilde{q}}}{\Gamma_{tot}} < 2.1 \times 10^{-3}, \qquad \frac{\Gamma_{t\to Z+\tilde{q}}}{\Gamma_{tot}} < 5.9 \times 10^{-3}. \tag{1.23}$$

Here $\tilde{q}$ represents final state quarks u and c.[3]

The paragraphs above explain that the top quark decays mostly to b quark and W boson. However, the W boson is decaying, too. Consequently, there are three different decay channels of top quark according to how W boson decays: the single-lepton, di-lepton and full-hadronic channels. The branching ratio of the decaying W boson to hadrons is equal to:

$$\frac{\Gamma_{W\to hadrons}}{\Gamma_{tot}} = (67.41 \pm 0.27)\%. \qquad [3]$$

Consequently, the fully-hadronic top quark decay channel is the most probable one.

1.3.3 Top quark production

The relevant Feynman diagrams for single top quark production can be found in Fig. 1.7 and for top pair production in Fig. 1.8. Let us note here, the most dominant diagram represents t-channel for single top production. And similarly, the most important diagram for top pair production at the LHC is the s-channel with gluon fusion.

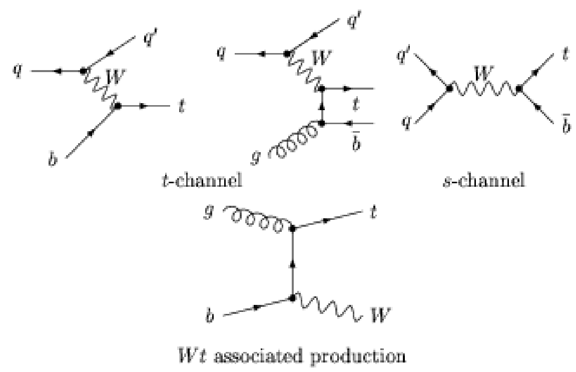

Figure 1.7: The dominant Feynman diagrams for a single top production.

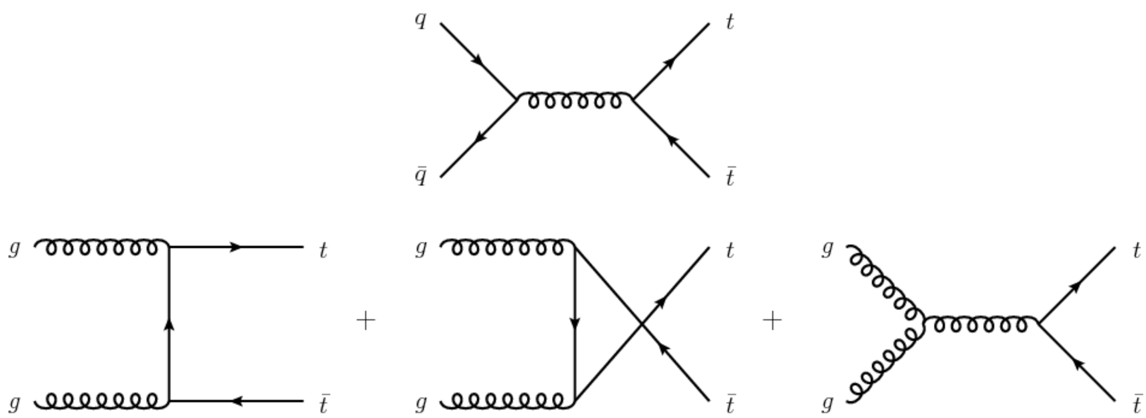

Figure 1.8: The dominant Feynman diagrams in leading order for a $t\bar{t}$ pair production.

1.4 Variables in high energy physics

In high energy physics, there are reactions and processes involving significant energies and momenta, which are much larger than the invariant mass of a given process. Consequently, it is quite important to consider a relativistic description of such processes. Additionally, it is crucial to define the Lorentz invariant variables or the variables with reasonable transformation under the change of frame at least.

Let us start with the relativistic relation between the energy E and the three-momentum $\vec{p}$.

$$E^2 = m^2c^4 + \vec{p}^2c^2,$$

where m is identified with invariant mass and c denotes a speed of light in vacuum with a magnitude $c = 299\,792\,458\ \mathrm{ms}^{-1}$. Using the standard units, where $c = 1$, the relativistic energy leads to:

$$E^2 = m^2 + \vec{p}^2$$

Now the four-momentum vector $P = (E, \vec{p})$ can be defined for the purpose of the relativistic calculations. One of common examples of the above mentioned Lorentz invariant variables is the square of four-momentum, $P^2 = m^2$.

Another useful kinematic variable represents the rapidity y, dimensionless variable, which is defined as follows.

$$y = \frac{1}{2} \ln \left(\frac{E + p_z}{E - p_z} \right) \tag{1.24}$$

Where E has the same meaning as above and p_z represents a three-momentum along z-axis. The z-axis is usually identified with the beam axis. Although the rapidity is not Lorentz invariant variable, it provides an elegant Lorentz transformation between two frames moving with constant relative velocity v with respect to each other.

$$y' = y - \tanh^{-1} \beta, \quad \text{, where} \quad \beta = \frac{v}{c}$$

Consequently, the change of rapidity is conserved under the Lorentz transformation:

$$\Delta y' = y_1' - y_2' = y_1 - y_2 = \Delta y \tag{1.25}$$

Another variable widely used in high energy physics is the pseudorapidity η, which is defined as follows:

$$\eta = -\ln \left[\tan \left(\frac{\theta}{2} \right) \right], \tag{1.26}$$

where θ is the polar angle, which is usually measured from the z-axis at the experiment. The psudorapidity η converges to rapidity y for zero mass $m \to 0$, or in other words in the high energy limit.

Another category of Lorentz-invariant variables are variables based on perpendicular components of three-momenta to the beam axis: p_x, p_y, which are not changed by the Lorentz boost. The examples of such observables are the transverse momentum p_t and azimuthal angle ϕ.

$$p_t = \sqrt{p_x^2 + p_y^2} \qquad \phi = \operatorname{arccotg} \frac{p_x}{p_y} \tag{1.27}$$

In conclusion, the Lorentz invariant variables become more natural for the collider physics. Thus, the thesis works with the coordinates (p_t, η, ϕ) as well as the other papers in high energy physics instead of the cartesian coordinates (x, y, z) or the momentum coordinates (p_x, p_y, p_z). In such a space we also often define a "metric" ΔR for a distance measurement of two objects i and j by the following formula:

$$\Delta R = \sqrt{(\eta_i - \eta_j)^2 + (\phi_i - \phi_j)^2} \tag{1.28}$$

The quantity ΔR is also often called the angular distance or the angular separation. It represents a dimensionless variable, which is often used in jets physics. Let us note, that pseudorapidity η is replaced by rapidity y sometimes. In this case ΔR becomes also Lorentz invariant considering eq. (1.25).

Finally we remind the transition between (p_x, p_y, p_z) coordinates and (p_t, η, ϕ) coordinates:

$$p_x = p_t \cos \phi \tag{1.29}$$
$$p_y = p_t \sin \phi \tag{1.30}$$
$$p_z = p_t \sinh(\eta) \tag{1.31}$$

Chapter 2

LHC and ATLAS detector

Predictions of the Standard Model or theories beyond the Standard Model have to be verified experimentally. This is usually done using sizable experimental apparatus (detectors) placed underground to shield the environment from radiation. Since predictions are manifold, such a detector is multi-purpose and hence often expensive. In the case of particle physics, cosmic ray observatories, and linear and circular colliders are used to provide fluxes of incident particles. An advantage of the cosmic ray observatories is quite a large range of energies, including ultra-high energy particles exceeding those achieved at accelerators. But such events are rather rare. Therefore accelerators are often used for a systematic research of particle interactions and of products coming from them. The most powerful accelerator of these days is Large Hadron Collider LHC, reaching energies of incident particles of 6.5 TeV and colliding frequencies of 10^8 Hz.

2.1 Large hadron collider

One of the main scientific center is represented by CERN (*l'Organisation européenne pour la recherche nucléaire)* at Franco-Swiss borders near Geneva. This scientific center contains many research devices connected to a number of cascading accelerators. The whole accelerating complex including the CERN experiments are shown in Fig. (2.1)

The beginning of the acceleration process starts at a hydrogen bottle. The hydrogen atom is a bound state of one proton and one electron. The hydrogen atoms are stripped of the electrons at a thin stripping foil to produce the protons. These protons can be accelerated now. There is linear accelerator Linac 2 to gain an energy of 50 MeV at the first accelerating step. Further, it follows a cascade of the circular accelerators. The protons continue to PSB (*Proton Synchrotron Booster*) to reach up an energy of 1.4 GeV. They are subsequently injected to PS (*Proton synchrotron*) accelerator, where the energy of protons increase to 25 GeV. The last preacceleration before the LHC injection is done in SPS (*Super Proton Synchrotron*) until the protons reach up 450 GeV of energy. Finally, the protons continue to the LHC (*Large Hadron Collidor*).

The LHC represents more than 27 km long circular accelerator, which dominates to the whole CERN complex. The proton injection to LHC is done using two beam pipes to provide two accelerating proton beams parallel to each other. It provides particle beam head on collisions at the interaction points, where four main experiments: ATLAS, CMS, LHCb and ALICE are located.

There are two general-purpose detectors ATLAS (*A Toroidal LHC ApparatuS*) and CMS (*Compact Muon Solenoid*). Both of them were designed to be able to study various topics at particle physic and also for finding the Higgs boson, the last missing particle of the Standard Model. The Higgs boson was discovered experimentally at both experiments in 2012. Further, there is LHCb (*Large Hadron Collider beauty*) focused on the study of b-hadrons and study of parity breaking phenomenon. The ALICE (*A Large Ion Collider Experiment*) was constructed to study heavy-ion collisions and quark-gluon plasma.

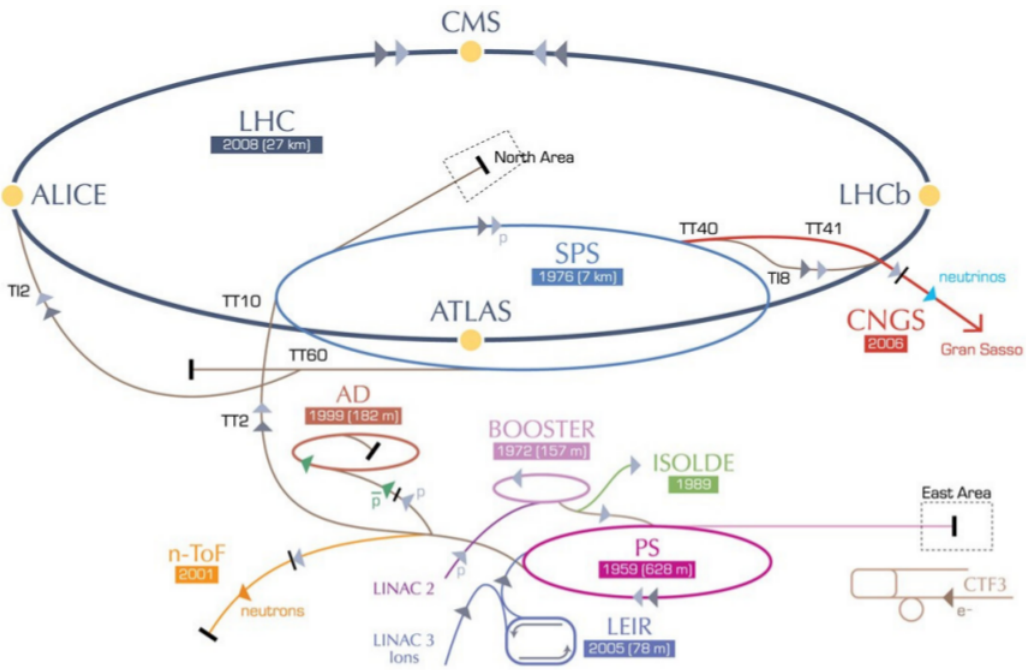

Figure 2.1: The CERN complex with all experimental devices and accelerators. Taken from [19]

As it was mentioned above, there are two accelerating tubes with two accelerating beams at the LHC. Both accelerating proton beams are able to gain 7 TeV, thus the LHC provides the protons with central mass energy s up to 14 TeV. The LHC was also designed for acceleration of Pb ions with energy 2.8 TeV per nucleon.

An acceleration of the charged particles is done by electric field in radiofrequency cavities. The charge particle beams are also focused by super-conductive quadrupole magnets with magnetic induction 8.33 T. The bending of the charge beam is done by dipole magnets along the LHC ring. The applied magnets are cooled down to 1.9 K by liquid helium. The tube covering the proton bunches is also filled by ultra-high vacuum to avoid the proton scattering and the following loss of the accelerated protons.

Since the proton dimension is quite small - of the order of 10^{-15} m, one-by-one collisions would be very inefficient, and therefore clouds of protons are collided instead. The proton clouds are chopped and focused to so called bunches. There are approximately 2800 bunches spaced along the 27 km long ring of LHC which is equivalent to a time separation between bunches of 25 ns. Each bunch contains $\sim 1.15 \times 10^{11}$ protons. Collisions of these bunches lead not only to a hard-scale scattering but also to additional scatterings with much softer scales. Such interactions are called pile-up.

An information about the colliding particles as well as the frequency of their collisions can be read from luminosity variable, main characteristic parameter of the accelerator. The luminosity is a proportional factor between the number of interactions per unit time dw_{fi} and the cross section σ. High instantaneous luminosities (accompanied by high pile-up) provide more data for a given period but at the same time, they also pose higher demands on the trigger, data acquisition and collection, and the following data processing.

2.2 ATLAS detector

The ATLAS detector is a cylindrical general-purpose detector designed for an investigation of various physic topics from the Higgs boson research to the extra dimensions and dark matter. The overview of the ATLAS detector is shown in fig. 2.2.

2.2.1 Inner detector

The inner detector ID is placed in the central part of the ATLAS detector. It represents a combination of the high-resolution semiconductor pixel detector Pixel, semiconductor tracker SCT, transition radiation tracker TRT. The geometrical concept of the ID consists of barrels and two two end-cups around the beam pipe. The inner detector is also immersed in a solenoidal magnet with magnetic induction 2 T. The magnetic field bends the trajectory of the charge particles by Lorentz force, which helps the vertex reconstruction and electron identification. [22]

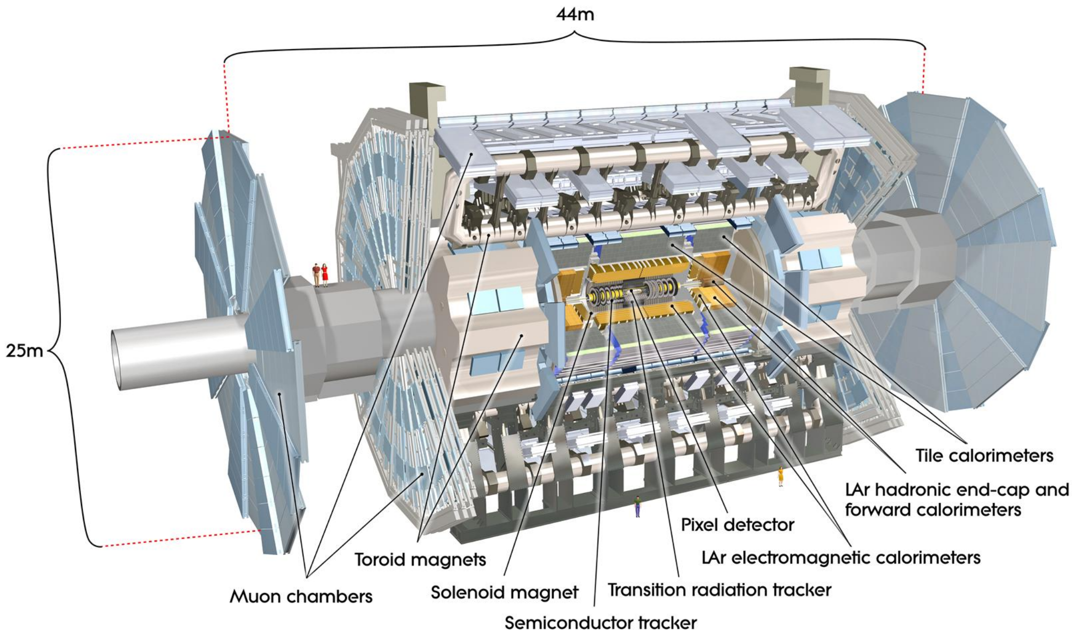

Figure 2.2: Schematic overview of the main parts of the ATLAS detector. Taken from [20].

2.2.2 Calorimeters

The calorimeters are constructed for a destructive energy measurement of the charge as well as the neutral particles. The particles are destroyed in interactions with a dense material in an absorber and the deposited energy is detected in an active material subsequently.

The calorimeters are located just behind the inner detector. There is high granularity liquid-argon electromagnetic sampling calorimeter LAr at first. The LAr covers the range of pseudorapidity $|\eta| < 1.475$. The electromagnetic calorimeters include lead as absorbers and LAr as active material. Further, the scinatilator-tile hadronic calorimeter surrounds the LAr with pseudorapidity ($|\eta| < 1.7$). The scintilator-tile hadron calorimeter is separated into a large barrel ($|\eta| < 1$) and two smaller extended barrels ($0.8 < |\eta| < 1.7$). The hadronic calorimeters use a steel at the absorber and scintilator as the active medium. The forward and backward sites of cylinder are covered, too. There are a combination of LAr electromagnetic end-cup EMEC ($1.375 < |\eta| < 3.2$), LAr hadronical end-cup HEC ($1.5 < |\eta| < 3.2$) and LAr forward calorimeter FCal ($3.1 < |\eta| < 4.9$). [22]

2.2.3 Muon spectrometer

The next main part of the ATLAS detector is a muon spectrometer, which measures the high penetrating muons with high transverse momenta. Such muons pass the inner detector and calorimeter system without a capture. The muon spectrometer uses a magnetic deflection of muon trajectories in a magnetic field of large superconducting air-core toroidal magnet. The magnet system consists of two end-cup toroids and one barrel toroid placed symmetrically around the beam axis. Each toroidal magnet is built from eight super-conductive coils. The measurement is provided by four subdetectors. There is a combination of two detectors for a measurement of the track coordinates: multi-wire proportional chamber called Cathod strip Chamber CSC and Monitored Drift Tube and finally two trigger subdetector: Resistive Plate Chambers RPC and Thin gap Chambers TGC. [22]

2.2.4 Trigger system

An indispensable part of the ATLAS detector is also the data trigger system and data collection system. Each event provides ~ 3 MB of data in a data storage. The proton collisions happen with a rate about 40 MHz at the interaction point, thus it is crucial to collect only interesting events for future analyses. These interesting events are found by the data trigger system. The ATLAS data trigger system was designed to have three levels: Level-1 L1, Level-2 L2 and event filter. At first, the L1 trigger takes into account the information from the muon spectrometer and calorimeter systems. In the (η, ϕ)-coordinate system, regions of interests (RoI) are defined which contain potentially interesting objects such as photons, jets, $\tau-$leptons with high p_t or events with significantly high missing transverse energy E_t^{miss}. The L1 trigger reduces the event rate to ≈ 75 kHz during 2 μs. Further, the L2 trigger reads out an available information from the RoI's, which amounts to ≈ 2 % of data in the whole event. The RoI's are evaluated and the rate of potentially interesting events is reduced to roughly 3.5 kHz. Finally in the last level of the trigger system, a fast part of the offline analysis is applied, so called event filter which is able to reduce the rate down to 200 MHz. [22] [23] [24]

Chapter 3

Data analysis techniques

3.1 Theory of jets

The basic principles of QCD were described in chapter 1.2. Color-rich objects described by QCD do not represent stable particles and they are hadronized. Thus quarks and gluons can not be observed directly. However, it is possible to observe the colorless particles at the end of hadronization. The colorless hadrons created in the process of hadronization of partons are collimated and focused in one direction, so they go out as a spray of particles, the so called jet, which can be detected in a detector and identified with a quark or gluon.

3.1.1 Jet algorithms

Jets are found using the so called jet algorithms which can be classified into two main categories. The first category is represented by the cone algorithms and the second one by the clustering algorithms.

The basic idea of the cone algorithms is that it tries to surround a significant flow of particles by a cone with radius R. Whereas the clustering algorithm tries to combine particles for finding an original object which stays at the beginning of QCD branching. In more detail, the clustering algorithms always combine two objects i, j retrospectively using an appropriate recombination scheme. This recombination scheme is applied on all considered objects repeatedly. The clustering algorithm is mostly based on the comparison of two distance variables denoted as d_{ij} and d_{iB}. The variable d_{ij} represents a mutual distance of two considered clusters i and j, whereas d_{iB} describes a jet-beam distance with respect to the cluster i.

Currently the most common used clustering algorithms in the hadron-hadron colliders are described by formula (3.1) using the common kinematic variables: transverse momentum p_t, rapidity y, azimuthal angle ϕ and a set of input parameters: jet radius R and parameter p, which is explained below.

$$\begin{gathered} d_{min} = \min(d_{ij}, d_{iB}) \quad \text{where} \quad d_{iB} = p_{t_i}^{2p}, \qquad d_{ij} = \min(p_{t_i}^{2p}, p_{t_j}^{2p}) \cdot \frac{\Delta R_{ij}}{R}, \\ \Delta R_{ij} = \sqrt{(y_i - y_j)^2 + (\phi_i - \phi_j)^2} \end{gathered} \tag{3.1}$$

The parameter p determines a weight of the transverse momenta p_t. The p parameter also distinguishes different methods for the particle assignment to a jet. Basically it is possible to differentiate the k_t algorithm ($p = 1$), anti-k_t algorithm ($p = -1$) and Cambridge/Aachen algorithm ($p = 0$) according to the value of p parameter.

The clustering itself is described by the following steps.

1.) determine the distance variables d_{ij} and d_{iB} of all clusters i and j

2.) determine $\min(d_{ij},\, d_{iB})$ of all clusters i and j

  a.) if $d_{ij} = \min(d_{ij},\, d_{iB})$, then:

I. cluster j is megred with cluster i

II. recalculate the cluster 4-momentum again according to the recombination scheme

b.) else if $d_{iB} = \min(d_{ij}, d_{iB})$, then:

I. denote object i as a jet

II. remove all merged particles (clusters) from the datalist

3.) repeat the procedure from point 1.) until the list of clusters is empty

Note here that the indices i and j correspond to different clusters at each passage of the clustering loop. Therefore all jets are found collectively at the same time, not one by one like in the case of the cone algorithms. Moreover the clustering procedure is infra-red unsafe at the moment. For example a well separated soft gluon radiation can create a soft gluon jet, thus another input parameter is necessary for the clustering jet algorithms, namely a minimal transverse momentum of the jet, $p_{t_{min}}^{jet}$.

Let us note that the clustering jet algorithms were designed to comply with the conditions of collinear and infra-red safety. Those two properties are crucial for the comparison of experimental results with theoretical calculations. The main disadvantage of the cone algorithms is the collinear and infra-red unsafety. The original clustering algorithms are both collinear and infra-red safe. The so called SIS Cone algorithm was developed to cope with the infra-red and collinear unsafeties.

Let us further remark that the clustering loop works with any clusters in general, not only with particles. The incoming objects for a clustering procedure can be for example tracks from the inner detector, clusters or towers of the calorimeter for a data analysis. The MC particles can be also considered for an analysis involving the MC generators. And interestingly, even small-R jets can be used in the case of the re-clustering algorithm, as we will see later.

k_t algorithm

Since the k_t algorithm is described by $p = 1$, hence the k_t algorithm clusters soft particles first and hard particles at the end. It causes an irregular output in the detector space of rapidity and azimuth angle (y, ϕ). By far most important properties of the anti-k_t algorithm are the infra-red and collinear safety, i.e. insensitivity to soft and collinear particles. The irregular output may complicate a loading data from special types of detectors, similarly it can make complications in an application of the nonperturbative corrections. Consequently it makes the k_t algorithm less suitable for experimental usage.[25]

Nevertheless, the k_t algorithm is often used for pile-up subtraction methods, trimming technique and filtering procedure of soft particles. Such procedures will be described below.

Cambridge/Aachen algorithm

Cambridge/Aachen algorithm is characterized by $p = 0$, thus Cambrige/Aachen clustering formulas are reduced to $d_{ij} < \frac{\Delta R_{ij}}{R}$ and $d_{iB} = 1$. It modifies the clustering condition as follows

$$\Delta R_{ij} < R. \tag{3.2}$$

Accordingly the Cambridge/Aachen algorithm does not consider the transverse momenta of the clusters like k_t or anti-k_t algorithms, but it respects only their mutual distances. Therefore, Cambridge/Aachen represents the basic algorithm of all category of the sequence clustering algorithms.

anti-k_t algorithm

The p parameter is equal to -1 in the case of the anti-k_t algorithm. Thus it leads to several important properties. Firstly, hard particles are clustered first. Parameter $p = -1$ also relates with a symmetrical output in a detector space coordinates $(y \times \phi)$. Those facts including the collinear and infra-red safety makes the anti-k_t algorithm currently most widely used and the safest algorithm. [26]

3.1.2 Trimming

Trimming technique is based on the application of the k_t algorithm. This method requires two input parameters: radius R_{sub} and f_{cut}.

Let us consider an original jet with radius R at the beginning of the trimming procedure. The original jet is re-clustered again using the k_t algorithm during the trimming procedure. The k_t algorithm is applied for finding the small soft sub-jets with a radius R_{sub}, where $R_{sub} < R$. Since the k_t algorithm merges soft particles first, sources of the soft particles can be localized. If the p_t fraction of the sub-jet is reasonably small with respect to the original jet, smaller than f_{cut} fraction, then the sub-jet is denoted as a source of soft particles, which influences the original jet resolution negatively. So the soft sub-jet is removed from the original jet. The trimming procedure is shown graphically in Fig. 3.1.

Consequently the condition for a subtraction of soft sub-jet from the original jet can be described as follows:

$$p_{t_i}^{sub} / p_t^{jet} < f_{cut}$$

where $p_{t_i}^{sub}$ denotes the transverse momentum of the i-th sub-jet with radius R_{sub} and the variable p_t^{jet} denotes the transverse momentum of the original R jet.

The trimming procedure is used to reduce pile-up and multiparton interactions without changing hard components in the final state. Low-mass jets ($m_{jet} < 100$ GeV) from a light-quark or gluon lose typically $30 - 50\%$ of their mass in the trimming procedure, while jets containing the decay products of a boosted object lose less of their mass, with most of the reduction due to the removal of pile-up or underlying event.[27]

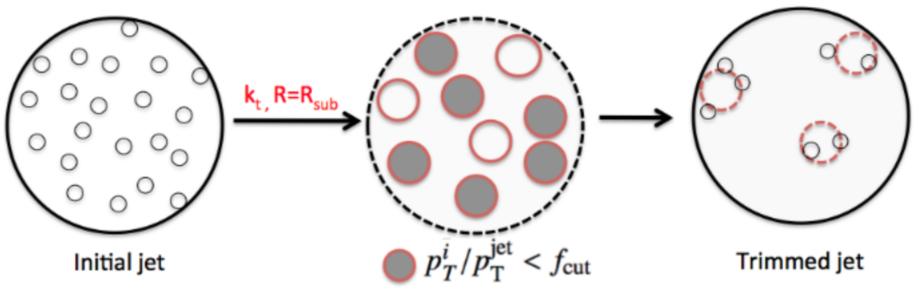

Figure 3.1: Schema of the jet trimming procedure. Taken from [27]

3.2 Unfolding

The detector disposes with a limited resolution and limited detector acceptance. Consequently those effects influence the measured physical distributions, thus advanced techniques for data analysis are necessary. This section introduces the unfolding technique whose application corrects for detector effects.

3.2.1 Motivation for the unfolding procedure

Let us assume the continuous measured function $g(s)$ in an experiment. The $g(s)$ function will be called the reconstructed function at the detector level. However the reconstructed function

$g(s)$ is influenced by detector effects, thus it is different from the $f(t)$ function describing the truth level. From a mathematical point of view, the relation between the reconstructed function $g(s)$ and the truth one $f(t)$ is described by the following Fredholm integral equation of the first kind.

$$g(s) = \int R(s,t)f(t)dt + b(s) \tag{3.3}$$

where the $R(s,t)$ function represents the kernel of the integral equation and it describes the response function involving "smooth" effects of the detector. Further the $b(s)$ function corresponds to the background distribution, which provides a source of fake events. The fake events correspond to different physical processes with respect to the studied one. The method for determination of the true physical function $f(t)$ from the measured one $g(s)$ is called the unfolding.

Since eq. (3.3) is usually solved numerically, it is necessary to discretize the integral equation. Let us recast the continuous measured function $g(s)$ to an vector $\vec{y}$ with final set of components. Let us assume an m-component vector $\vec{y}$ and similarly let us rewrite the background function as an m-component vector $\vec{b}$. Further the continuous true function $f(t)$ can be discretized as an n-component vector $\vec{x}$. Thus the response function $R(s,t)$ will be represented by a $m \times n$ response matrix $\mathbb{R}$. Consequently the Fredholm integral equation is discterized to m linear equations as follows.

$$y_i = \sum_{j=1}^{n} \mathbb{R}_{ij} x_j + b_i \tag{3.4}$$

Let us note that the vectors $\vec{x}$, $\vec{y}$ and $\vec{b}$ can be represented by histograms and similarly the response matrix $\mathbb{R}$ by a two dimensional histogram. The response matrix $\mathbb{R}$ describes how the truth level is connected with the detector level. Considering the perfect detector the response matrix would be a unit matrix (in case of $m = n$). However the response matrix is neither unit nor diagonal in general. Some events generated in the bin i could be reconstructed in another bin j, $i \neq j$. This phenomenon is called migration.

In order to distinguish smearing effects of the response matrix $\mathbb{R}$, it is possible to express the response matrix as a multiplication of efficiency correction ϵ_{eff}, migration matrix $\mathbb{M}$ and the inverse fiducial correction f_{acc}, the so called acceptance, as follows.

$$\mathbb{R}_{ij} = \frac{1}{f^i_{acc}} \cdot \mathbb{M}_{ij} \cdot \epsilon^j_{eff}$$

The above mentioned smearing effects can be simulated. First the signal events are simulated by Monte Carlo generator involving Standard Model prediction. Such Monte Carlo events provide the events at truth level T. Then a full detector simulation is applied to get the events at so called reconstructed level R. The idea of simulation as well as the interpretation of acceptance f_{acc} and efficiency ϵ_{eff} corrections can be found in Fig. 3.2.

Using the results of simulation one can evaluate acceptance f_{acc} and efficiency ϵ_{eff} corrections.

$$f^i_{acc} = \left.\frac{R \cap T}{R}\right|_{\text{bin } i} = \frac{\text{number of events in bin } i \text{ at reconstracted level passing the selection criteria at truth and reconstructed level}}{\text{number of events in bin } i \text{ passing selection criteria at reconstructed level}} \tag{3.5}$$

$$\epsilon^j_{eff} = \left.\frac{R \cap T}{T}\right|_{\text{bin } j} = \frac{\text{number of events in bin } j \text{ at truth level passing the selection criteria at truth and reconstructed level}}{\text{number of events in bin } j \text{ passing selection criteria at truth level}} \tag{3.6}$$

Further, the smearing matrix elements can be estimated as

$$M_{ij} = \frac{\text{number of events in both bin } i \text{ at reconstructed level and bin } j \text{ at truth level passing the selection criteria at truth and reconstructed level}}{\text{number of events in bin } j \text{ at the truth level passing selection criteria at reconstructed and truth levels}}. \tag{3.7}$$

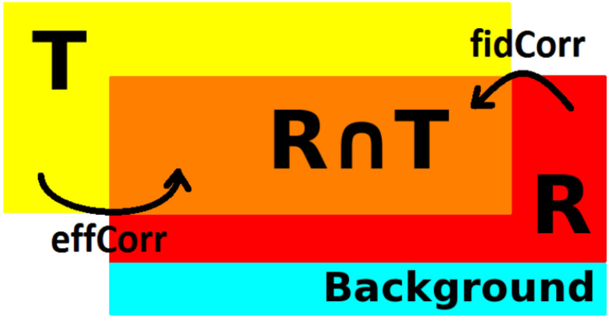

Figure 3.2: Schema of the relation between the truth, reconstructed level and background. The background is subtracted from data to reach a reconstructed distribution R, where all events pass the selection criteria at reconstructed level. T represents truth level, where all events pass the truth selection criteria. If some event pass both reconstructed and truth selection criteria, then it is found in the intersection of both sets $R \cap T$. The acceptance correction is denoted here as $fidCor$ and efficiency correction as $effCor$. Both corrections describe dependence between the intersection $R \cap T$ and individual sets of R or T. Taken from [28]

Consequently the efficiency ϵ_{eff} correction provides the probability that events which pass the selection at truth level also pass the selection at reconstructed level. And similarly, the acceptance f_{acc} describes the probability that a signal event which passes the selection at reconstructed level also passes the selection at truth level. The matrix element M_{ij} describes the probability that an event generated and selected in the bin j at truth level is reconstructed in the bin i at reconstructed level. [28]

3.2.2 The Bayesian theorem

Let us assume probability functions $P(A)$, $P(B)$ of some phenomena A and B and their conditional probabilities $P(A|B)$ and $P(B|A)$. Then Bayesian theorem reads

$$P(A|B) = \frac{P(B|A)P(A)}{P(B)}. \tag{3.8}$$

Using the so called law of total probability $P(B) = \sum_i P(B|A_i)P(A_i)$ of the subset A_i, one can recast the conditional probability $P(A|B)$ as follows.

$$P(A|B) = \frac{P(B|A)P(A)}{\sum_i P(B|A_i)P(A_i)} \tag{3.9}$$

The importance of the Bayesian theorem for the data analysis appears if one replaces A and B by the *hypothesis* and *data*, thus

$$P(hypothesis|data) \propto P(data|hypothesis) \times P(hypothesis). \tag{3.10}$$

The expression $P(hypothesis)$ is often called the prior probability and it represents our knowledge about the truth of the hypothesis.

3.2.3 Bayesian iterative unfolding

The Bayesian iterative unfolding is the most used unfolding technique at the field of the experimental particle physics. The method is based on the Bayesian theorem of the conditional probability, which was introduced in the previous section.

Let us assume causes C and effects E with n_C possible causes and n_E possible effects. The causes C correspond to the truth level distribution, whereas the effects E are connected with the reconstructed level distribution. Both causes C and effects E are presented at $R \cap T$ as a intersection phase-space of reconstructed and truth level. The variables $n(C_j)$, resp. $n(E_i)$ denote the number of events in the jth bin at truth level, resp. the ith bin at reconstructed level.

The number of events $n(E_j)$, which enter the migration matrix at the reconstructed level can be evaluated from data distribution D_i at the reconstructed level as follows.[28]

$$n(E_i) = (D_i - B_i) \cdot f^i_{acc} \tag{3.11}$$

where B_i describes the number of events in the background distribution in the bin i and f^i_{acc} the appropriate acceptance correction.

The number of events of causes $n(C_j)$ coming from the migration matrix at the truth level is proportional to truth distribution μ_j and the appropriate efficiency correction ϵ^j_{eff}.

$$n(C_j) = \mu_j \cdot \epsilon^j_{eff} \tag{3.12}$$

Considering the intersection phase-space, where all events passed both reconstructed and truth level selection criteria, one can define the total number of events N_{tot} and probabilities $p(E_i)$ and $p(C_j)$.

$$N_{tot} := \sum_{i=1}^{n_E} n(E_i) = \sum_{j=1}^{n_C} n(C_j) \tag{3.13}$$

$$p(E_i) := \frac{n(E_i)}{N_{tot}} \tag{3.14}$$

$$p(C_j) := \frac{n(C_j)}{N_{tot}} \tag{3.15}$$

For the determination of $p(C_j)$ the iterative approach can be used in the Bayesian theorem as follows.

$$p_n(C_j|E_i) = \frac{p(E_i|C_j) \cdot p_{n-1}(C_j)}{\sum_{k=1}^{n_C} p(E_i|C_k) \cdot p_{n-1}(C_k)}, \tag{3.16}$$

where $p(E_i|C_j)$ is a conditional probability, that we find the effect in the bin i if it is the cause in the bin j. Such a probability is equal to the smearing matrix element $\mathbb{M}_{ij}$, which can be simulated using the signal truth Monte Carlo sample and full detector simulation using GEANT4 [49]. The index n represents the nth iteration. Further the prior distribution $p_0(C_j)$ has to be chosen at the first iteration. A common choice of prior is Monte Carlo distribution:

$$p_0(C_j) = \frac{\text{number of events bin } j \text{ at truth level passing the selection criteria at truth and reconstructed levels}}{\text{number of events passing the selection criteria at truth and reconstructed levels}}. \tag{3.17}$$

In the case of a higher iteration $n+1$, the result of the previous one is used as a prior, namely:

$$p_n(C_j) = \sum_{i=1}^{n_E} p_n(C_j|E_i) \cdot p(E_i). \tag{3.18}$$

In this study four iterations turned out to be optimal. The final result of unfolded distribution μ_j is reached using eqs. 3.12, 3.15 and 3.18 as

$$\mu_j = p_n(C_j) \cdot N_{tot} \cdot \frac{1}{\epsilon^j_{eff}} \tag{3.19}$$

3.2.4 Fiducial cross section at the experiment

So far we have discussed distributions, however the analyses often aim at the so called fiducial cross-section, the cross-section corresponding to a chosen kinematic region. The cross-section can be obtained from the unfolded distribution at particle level and some proportional factor, which can be denoted as $\frac{1}{\mathcal{L}_{INT}}$. The introduced $\mathcal{L}_{INT}$ variable is called the integrated luminosity and it describes basically properties of the accelerator.

Considering the integrated luminosity $\mathcal{L}_{INT}$, one can evaluate the differential fiducial cross-section $\frac{d\sigma^{fid}}{dX^i}$ for an observable X at ith bin as follows.

$$\frac{d\sigma^{fid}}{dX^i} = \frac{1}{\mathcal{L}_{INT} \cdot \Delta X^i} \cdot \mu^i, \tag{3.20}$$

where the unfolded distribution of events μ^i (including the acceptance f_{acc} and efficiency ϵ_{eff} corrections) at particle level is obtained using eq. 3.19 and ΔX_i is the bin width.

So, taking all together we get a final expression for the differential cross-section formula at the fiducial phase-space.

$$\frac{d\sigma^{fid}}{dX^i} = \frac{1}{\mathcal{L}_{INT} \cdot \Delta X^i} \cdot \frac{1}{\epsilon^i_{eff}} \cdot (\mathcal{U}[I])_i. \tag{3.21}$$

where the Bayesian unfolding procedure was denoted schematically as functional $\mathcal{U}[I]$, which is obtained from the distribution I as data distribution D after the background subtraction B and application of acceptance correction f_{acc}. Each ith bin of such I distribution is read as follows:

$$I_i = f^i_{acc} \left(D_i - B_i \right). \tag{3.22}$$

3.3 Jet and jet substructure variables

3.3.1 Jet mass

The jet algorithms try to reconstruct the original four-momenta of the parent particles staying at the beginning of the QCD branching. Considering this idea and the conservation laws of energy and three-momenta, it is natural to define the jet mass m_J as follows.

$$m_J = \sqrt{\left(\sum_{k \in J} E_k \right)^2 - \left(\sum_{k \in J} \vec{p}_k \right)^2} \tag{3.23}$$

Here it is summed over all constituents k in the jet J. Consequently $\sum_{k \in J} E_k$ and $\sum_{k \in J} \vec{p}_k$ correspond to the total energy and three-momentum of the original parent particle before the decay.

3.3.2 k_t splitting scale

The k_t splitting scale represents a variable describing the distance between two considered proto-jets i and j. The k_t clustering algorithm is used for the jet reconstruction, thus the hardest constituents are combined at last. The splitting scale is defined as follows

$$\sqrt{d_{ij}} = \min(p_{t_i}, p_{t_j}) \times \Delta R_{ij}, \tag{3.24}$$

where the p_{t_i} and p_{t_j} correspond to the transverse momenta of the last ith and jth constituents during the jet clustering. Further the ΔR_{ij} variable denotes the mutual distance of two considered proto-jets using the common variable: pseudorapidity η and azimuth angle ϕ, thus $\Delta R_{ij} = \sqrt{(\eta_i - \eta_j)^2 + (\phi_i - \phi_j)^2}$.

The last step of clustering leads to $\sqrt{d_{12}}$ observable and similarly the $\sqrt{d_{23}}$ can be reached at the second-last step of the clustering. Those $\sqrt{d_{12}}$ and $\sqrt{d_{23}}$ quantities can be used to distinguish a heavy particle decay, which tends to be reasonably symmetric, when the decay is to like-mass particles, from the largely asymmetric splittings that originate from a QCD radiation in light quark or gluon jets.[27] It is expected that $\sqrt{d_{12}} \approx \frac{m^{parent}_{particle}}{2}$ for a heavy parent particle decaying to two bodies, whereas the splitting scale $\sqrt{d_{12}}$ for light quarks or gluon reaches smaller values and falls steeply.

3.3.3 N-subjettiness τ_N

The N-subjettiness τ_N provides an information about the multiplicity of subjets in a considered jet, so it can be used to distinguish two-prong and three-prong jet produced from a heavy particle decay.

First the jet is reconstructed by an arbitrary jet algorithm with the jet radius R. Further N subjet candidates are identified, forcing to return exactly N subjets.[37]. It can be done using for example the exlusive k_t clustering algorithm. The τ_N can be evaluated subsequently via eq. 3.25 with those N subjet candidates.

$$\tau_N = \frac{1}{d_0} \sum_k p_{t_k} \times \min\left(\Delta R_{1_k}, \Delta R_{2_k}, \dots \Delta R_{N_k}\right), \quad \text{where} \quad d_0 = \sum_k p_{t_k} \cdot R \tag{3.25}$$

Here the index k runs over all constituents of the jet. The p_{t_k} in eq. (3.25) corresponds to the transverse momenta of the constituent k. ΔR_{ik} is a distance between the axis of subjet i and the constituent k. The distance ΔR_{ik} is again described in the $(y \times \phi)$ space as well as the jet radius R.[27, 37]

It is observed that the τ_N represents a positive and decreasing function of N subjet candidates, thus

$$0 < \frac{\tau_N}{\tau_{N-1}} < 1. \tag{3.26}$$

3.3.4 Top tagging

The top-tagging represents a procedure, which provides an information, whether a jet can be identified with the top quark. The current top-tagging algorithm is based on a jet mass estimation around the invariant mass of top quark and a τ_{32} variable, which will be introduced below.

As it was discussed previously quarks and qluons are not observed directly but as jets. Therefore a question may arise how to distinguish a quark jet from a gluon one. Here the N-subjettiness τ_N may help.

It is known that the top quark provides three quarks in the finale state. Those three quarks are observed as three jets. On the other hand the gluon splits into two quarks or two quark jets. Then, one can consider the fractions τ_3 and τ_2, which still satisfy eq. (3.26). Consequently, the τ_{32} variable defined as a simple fraction

$$\tau_{32} = \frac{\tau_3}{\tau_2} \tag{3.27}$$

can evaluate the probability, that a jet involves three rather than two subjets. In other words τ_{32} gives the provability that the jet can be identified with a quark jet.

This thesis uses a standard top-tagging in the ATLAS collaboration making use of both discussed criteria, namely

$$|m_{jet} - m_{top}| < 50 \text{ GeV} \quad \text{,where} \qquad m_{top} = 172.5 \text{ GeV} \tag{3.28}$$

$$\tau_{32} > 0.5. \tag{3.29}$$

3.3.5 B-tagging

The identification of a jet which originate from heavy flavour quarks, represents a necessary procedure for a data analysis at the high-energy particle physics. Considering the b-jet identification then we are talking about the so called b-tagging, which becomes necessary for the top quark data analysis.

The b-tagging is based on a set of variables, which are able to discriminate between different jet flavours. The variables reflect the characteristic properties of b-hadrons such as the relatively high mass ($\approx$ 5 GeV with respect to the decay products), specific decay multiplicity ($\approx$ 5 charge tracks per decay) and a mean lifetime or the impact parameter.

There are three different b-tagging algorithms at the ATLAS experiment: *Impact parameter based algorithm*, *Inclusive secondary vertex reconstruction algorithm* and *Decay chain multi-vertex reconstruction algorithm*, which provide a complementary information. The information from all these algorithms is combined in a multivariable MVA discriminant.[34]

Due to a long lifetime of b-hadrons, tracks originated from b-hadron decay products tend to have large impact parameters. Such observation is a baseline for impact parameter based algorithm. The inclusive secondary vertex reconstruction algorithm tries to reconstruct a single secondary vertex per jet using a list of tracks inside the cone. The last mentioned algorithm tries to reconstruct a weak decay chain of a b-hadron produced at the primary vertex which subsequently decays to a charm hadron, which produces a tertiary vertex finally. The algorithm identifies the b-hadron flight path using an assumption that the tertiary vertex of charm hadron lies along the same flight path.[35]

Considering the MVA discriminant a jet is classified as the b-jet if the MVA value is greater than a certain threshold. An example of such MVA discriminant is a MV2c10, which was also applied in the $t\bar{t}$ pair analysis with rejection factors for charm quarks and light jets as 12 and 380, respectively, and the b-tag efficiency of 77 %.[36]

3.4 Background estimation for $t\bar{t}$ production

As we described in the previous section, background has to be subtracted from the data before the unfolding procedure is used. In general, the background can be estimated using the MC simulation or the real data.

The analysis of all-hadronic $t\bar{t}$ events have to consider the background sources arising from non all-hadronic processes, single top-quark production, associated production of $t\bar{t}$ pair $W/Z/H$ boson. All these processes can be evaluated using the MC simulations. Details can be found in 4.1.3. An example of data driven technique will be demonstrated on multijet background, which becomes the most dominant in the analysis of the $t\bar{t}$ pairs in full-hadronic events.

3.4.1 Multijet background estimation

Thanks to its relatively sizable cross section and non-zero top tagging inefficiency, we have to study in detail the contribution of the multi-jet background where one of u, d, c, s, b quarks or gluon can be misidentified as a top-jet candidate.

It was shown that Monte-Carlo predictions of multijet events suffer from large uncertainties coming from the relatively poorly understood higher-order contributions that produce a pair of massive jets.[36, 38, 39] Consequently a data driven technique has to be used. The applied data driven method is called ABCD method and it will be described below.

Basic concept of ABCD method in 4 regions

The ABCD method is based on the data categorization according to two uncorrelated variables. Considering two statistically independent variables i and j, which reach up two discrete values e.g. $i, j \in \{0, 1\}$, the data can be classified into four regions, denoted as A, B, C and D. This example is also shown in Tab. (3.1).

	$j = 0$	$j = 1$
$i = 0$	A	B
$i = 1$	C	D

Table 3.1: The four regions of the ABCD method as a toy example for multijet background estimation. The given data are classified into four A, B, C, D regions according to two independent variables i, j. The region D describes the signal region.

Since the variables i and j are independent, the total number of events in the signal region D can be evaluated as a fraction of the total number of events in the remaining regions A, B, C.

$$D = B \cdot \frac{C}{A}$$

Since we are mostly interested in a differential distribution of x variable, let us extend the previous model to histograms. Let us assume that the variable x disposes with the same shape in all regions. In other words the parameters i, j do not influence the shape of the x distribution. Let us note the number of events in the bin k of appropriate histograms as $A[k]$, $B[k]$, $C[k]$ and $D[k]$. Then it is possible to estimate a differential distribution of the variable x in a signal region D as follows.

$$D[k] = B[k] \cdot \frac{C[k]}{A[k]} \tag{3.30}$$

3.4.2 ABCD method in 16 regions

This subsection explains an extended ABCD method to 16 region, which was developed for the analysis of $t\bar{t}$ full-hadronic decay events. Here i, j parameters introduced in the previous section represent the leading and subleading jets. Considering the top-tagging and b-matching of those large-R jets as a discrete parameters of the leading and sub-leading large-R jets, a table similar to Tab. 3.1 can be constructed for the following multijet background calculus.

The b-matching of large-R is based on the angular distance condition

$$\Delta R(b\text{-jet}, \text{large-}R \text{ jet}) < 1.0.$$

In other words the considered large-$R = 1.0$ jet includes at least one b-jet.

Each region from A to O in Tab. (3.2) is associated with a number of multi-jet events with an appropriate top-tagging and b-matching of two highest-p_t large-R jets. An expected number of multijet background events $N_{multijet}$ in each region from A to O is evaluated as follows.

$$N_{multijet} = N_{data} - N_{signal_{MC}} - \sum_{i \in bg\, MC} N_i \tag{3.31}$$

Here N_{data} denotes the reconstructed number of events in data. Further $N_{signal_{MC}}$ represents a number of Monte Carlo signal events. And finally the background events of all relevant processes, which are predicted by Monte Carlo simulations, are denoted as $\sum_{i \in bg\, MC} N_i$.

Using the ABCD method, the multijet distribution $N_{multijet}$ can be estimated as a simple fraction $S = \frac{J \times O}{A}$, however it was shown that the top-tagging and b-matching variables are not entirely independent, thus corrections were introduced involving a dependence on the other regions.[36] Further it was shown that the blue regions K, L, M, N in Tab. (3.2) contain too much of the signal and propagate high systematic uncertainties.[36] Thus blue regions K, L, M, N have not been used for the final multi-jet background estimation, and white ones

2nd leading large-R jet				
1t1b	J	K	L	S
0t1b	B	D	H	N
1t0b	E	F	G	M
0t0b	A	C	I	O
	0t0b	1t0b	0t1b	1t1b
	1st large-R jet			

Table 3.2: The events are classified by assigning discrete parameters to the leading and subleading jet in a given event after the top-tagging and b-matching is finished. So for example $1t1b$ of the leading jet means it is top-tagged and contains at least one b-tagged jet, while $0t1b$ means the jet contains at least one b-tagged jet. Identically for the subleading jet. The blue regions K, L, M and N contain too much signal and therefore they are not used in the final ABCD method formula.

were used as it is denoted in Tab. (3.2). The final formula for the multi-jet background estimation in the bin k of an appropriate distribution in the signal region S then reads:

$$S_k = \frac{J_k \times O_k}{A_k} \cdot \frac{D_k \times A_k}{B_k \times C_k} \cdot \frac{G_k \times A_k}{E_k \times I_k} \cdot \frac{F_k \times A_k}{E_k \times C_k} \cdot \frac{H_k \times A_k}{B_k \times I_k} = \frac{J_k \times O_k \times H_k \times F_k \times D_k \times G_k \times A_k^3}{(B_k \times E_k \times C_k \times I_k)^2} \tag{3.32}$$

Chapter 4

Measurement of all-hadronic $t\bar{t}$ differential cross section

In this chapter we will describe the measurement of the differential cross-section of highly boosted $t\bar{t}$ pairs as a function of various kinematic observables. The analysis was performed on the complete data sets collected by the ATLAS detector at $\sqrt{s}$ = 13 TeV of pp collisions in years 2015 and 2016 with the integrated luminosity 36.1 fb^{-1}. Similar measurements have been performed previously at lower energies and lower luminosities by ATLAS [36] [42] [43] [44] [45] and CMS [46] [47] experiments at central mass energy $\sqrt{s}$ = 7 TeV and $\sqrt{s}$ = 8 TeV in pp collisions.

The presented analysis is based on the framework developed by the working group at the ATLAS experiment called: *Differential ttbar cross-sections at 13 TeV all-hadronic boosted group*. The main goal of the thesis is to investigate the properties of re-clustered top quark jets to see whether they provide a better estimation of systematic uncertainties using the framework of the working group specified above. The motivation for such an analysis is supported by previous studies of re-clustered jets [30] and the study of close-by effects of Large-R jets in [40], [41].

4.1 Event selection

The boosted topology is considered primarily because it provides well separated and well defined objects. Collision energies reached at LHC attain such values, that the momentum transfer of interacting partons in both protons acquire high values. In such cases top quark pairs may be produced. Most of time, the two high-p_t top quark jets move in opposite directions to each other. Thanks to the high value of transverse momentum both jets are significantly influenced by Lorentz boost. That means that usually instead of six jets, two jets with large radii (typically $R \geq 1.0$) are observed, each containing all top quark decay products.

The boosted topology approach in events with all-hadronic top quark jets is based on requiring at least two high-p_t large-R jets and no leptons. The two large-R jets are then tested, whether they can be identified with the top-jet candidates.

4.1.1 Data selection criteria

The individual pre-selection criteria are shown in Tab. 4.1. Since, we are interested in the boosted topology, only high p_t-jet triggers are considered. Each event has to have a primary vertex reconstructed from five or more associated tracks. Further we require no high-p_t leptons to reject $t\bar{t}$ pair events arising from the leptonic and semileptonic decays. The large-R jets are found using anti-k_t algorithm with radius R = 1.0. Those large-R jets are also trimmed using R_{sub} = 0.2 and f_{cut} = 0.05 for suppression of QCD radiation and mitigation of pileup-effects. Description of the trimming procedure is described in section 3.1.2. In addition, since jets

cut	Event pre-selection
hadronic trigger	`HLT_j360_a10r_L1J100` or `HLT_j420_a10r_L1J100`
primary vertex	≥ 5 tracks with $p_t > 0.4$ GeV
no isolated leptons	muons: $p_t > 25$ GeV, $\lvert\eta\rvert < 2.5$ electrons: $p_t > 25$ GeV $0 < \lvert\eta\rvert < 1.37$ or $1.52 < \lvert\eta\rvert < 2.47$
anti-kt $R = 1.0$ jets	≥ 2 jets with $p_t > 350$ GeV, $\lvert\eta\rvert < 2.0$ ≥ 1 jets with $p_t > 500$ GeV, $\lvert\eta\rvert < 2.0$
anti-kt $R = 0.4$ jets	≥ 2 jets with $p_t > 25$ GeV, $\lvert\eta\rvert < 2.5$

Table 4.1: Pre-selection criteria.

corresponding to b-quarks are a part of the boosted topology, we reconstructed small-R jets using anti-k_t algorithm with $R = 0.4$ and require at least one of them to be b-tagged. The cut on pseuropadity $|\eta|$ ensures that top-quark jets as well as the b-tagged jets are reconstructed in a central detector. Finally the p_t of large-R jets is tested, we require at least two anti-k_t large-R jets with $p_t > 350$ GeV and at least one of them to have $p_t > 500$ GeV. Then the two jets with highest p_t are identified with the top-jet candidates using criteria summarised in Tab. 4.2.

Further, each top-jet candidate has to contain at least one b-jet, which is verified by the condition on angular separation ΔR(large R jet, b-jet) < 1.0. However, the small-R anti-k_t jets have to be tested first, whether they can be identified as b-jets. The b-jet criteria are summarized in Tab. 4.3, where the most important part is denoted as b-tagging, which is described briefly in section 3.3.5.

cut notation	requirement
p_t	$p_t > 250$ GeV
η	$\lvert\eta\rvert < 2.0$
mass	$m > 50$ GeV
b-matching	ΔR(large R jet, b-jet) < 1.0
top-tagging	$\lvert m_{Jet} - m_{top}\rvert < 50$ GeV $\tau_{32} > 0.5$

Table 4.2: Identification criteria for top-jet candidates.

cut notation	requirement
b-tagging	with efficiency > 0.77 %
p_t	$p_t > 25$ GeV
η	$\lvert\eta\rvert < 2.5$

Table 4.3: Identification criteria for a b-tagged anti-k_t $R = 0.4$ jet for finding the b-jet candidates.

The two top-jet candidates with highest p_t (denoted as leading and subleading jet) then form the so called signal region. The rest of the events is utilized for an estimate of the multijet background using the data driven technique. Finally, the $t\bar{t}$ system is defined as a sum of momenta of four-vectors of leading and subleading top-jet candidates.

4.1.2 Particle level definition

The particle level is defined by the following set of requirements. All those criteria were required on Monte Carlo events.

- at least 2 anti-k_t large-$R = 1.0$ jets with $p_t > 350$ GeV
- at least 1 anti-k_t large-$R = 1.0$ jet with $p_t > 500$ GeV
- at least 2 anti-k_t small-$R = 0.4$ jets with $p_t > 25$ GeV
- mass of both leading large-$R = 1.0$ jets to be within 50 GeV of top quark mass
- both leading anti-k_t large-R to have a b-hadron in the final state (using ghost-matching technique)

- no electrons or muons with $p_t > 25$ GeV

4.1.3 Data modelling and the background estimation

The ATLAS data have been processed and compared with theoretical predictions of Monte Carlo simulations, which are summarized here.

Signal samples

The signal sample of $t\bar{t}$ pair production was generated by NLO QCD generator POWHEG together with an interface of the hadronization model and parton showering of PYTHIA8. Such a combination of Monte Carlo generators is called POWHEG+PYTHIA.

Background estimation

The multijet background comes from events, where large-R jet coming from gluon g or u, d, s, c, b quark were misidentified as top-jet candidates. This background was first evaluated by Monte Carlo, but significant differences between various Monte Carlo generators were observed, which caused large systematic uncertainties. For example, QCD dijet samples POWHEG+PYTHIA predict less than half of amount in comparison with PYTHIA 8. A large discrepancy of dijet events suggests that the MC samples are inaccurately normalized.[50] Consequently, a data driven technique was developed for the multijet background estimation called the 16 regions ABCD method, which is described in section 3.4.1.

Let us summarize here all relevant background processes for all-hadronic $t\bar{t}$ decay channel, and techniques used to estimate them. The backgrounds are ordered according to the significance.

- multijet background: 16 regions ABCD method
- non all-hadnonical processes: POWHEG+PYTHIA8
- single top production: POWHEG+PYTHIA6
- associated production of $t\bar{t}$ with $W^{\pm}$, Z^0 and H boson: aMC@NLO+PYTHIA8

All listed processes except the multijet background were simulated by Monte Carlo generators whose names are specified in the list.

The weakly decaying top quark gives a b quark and W boson, which decay subsequently. The W boson may provide also a lepton and an appropriate neutrino, not only the wanted quarks. Thus, the leptonic and semileptonic processes represent another background of all-hadronic $t\bar{t}$ pair production. Such processes are classified together as non all-hadronical processes in the analysis. The non all-hadronic $t\bar{t}$ processes have become the second largest background. The $t\bar{t}$ non all-hadronic processes were simulated by POWHEG generator together with an interface of the hadronization model and parton showering of PYTHIAv6.425. The non all-hadnonic background contributes by ~ 4% to the signal region.

Another considered background source comes from the single top-quark production in the Wt channel. The single top production was simulated similarly as the non all-hadnonic processes by the combination of POWHEG+PYTHIA6 Monte Carlo generators.

The final relevant background source represents an associated production of the $t\bar{t}$ pair with $W^{\pm}$ boson, Z^0 boson or H boson. Such events were simulated by aMC@NLO Monte Carlo generator coupled with a shower and hadronization model of PYTHIA8. The same set of PDF as at the $t\bar{t}$ samples was used. The cross-sections for those processes $t\bar{t} + W^{\pm}$, $t\bar{t} + Z$ and $t\bar{t} + H$ were computed by MadGraph5_aMCNLO MC generator as follows: 0.603 pb, 0.586 pb and 0.231 pb.[36] Consequently, the cross section of the associated production $t\bar{t} + W/Z/H$ is less than one percent of the $t\bar{t}$ signal region.

Full detector simulation

Events in the Monte Carlo samples were simulated using a full detector simulation via GEANT4[49] and scaled to the integrated luminosity of the measured data $\mathcal{L}_{int}^{lumi} = 36.1\ \mathrm{fb}^{-1}$.

4.2 Systematic uncertainties

The total systematic uncertainty of measurement consists of various components, which can be classified in three categories according to their origin such as Monte Carlo modelling, background estimation and object reconstruction and calibration.

4.2.1 Object reconstruction and calibration

The object reconstruction and calibration uncertainty is dominated by the jet energy scale, which is derived using a combination of simulations, test beam data and in situ measurements [53] [54] [55] [56] [36]. The jet flavour composition, calorimeter response to different jet flavours as well as pile-up are considered. Uncertainties in the jet energy resolution are estimated using the in situ measurement of the jet response asymmetry in dijet events.[57] The associated systematic uncertainties with b-jets are computed as in [58] [59] [60] [61]. The list of large-R jet systematics uncertainties can be found in [36].

4.2.2 Signal modelling uncertainties

The modelling uncertainties arise from the following sources: parton-shower models, hadronization models, inital and final state radiation and matrix elements calculations.

The uncertainty arising from parton-shower and hadronization models are based on Powheg+Herwig7 generators using the same PDF set as the nominal Powheg+Pythia8 sample.

The uncertainty connected with the initial and final state radiation (ISR/IFR) is based on two samples Powheg+Pythia8. Considered samples increase or decrease the amount of ISR and FSR by a certain amount compared to the original signal Monte Carlo sample.

The uncertainty of matrix-element calculation was simulated with by MadGraph5_aMC@ NLO generator interfaced to Pythia8. The MC@NLO+Pythia8 sample suffers from a known mismodelling in several observables (such as p_t of $t\bar{t}$ system $p_t^{t\bar{t}}$ or azimuthal angle between both leading and subleading top-jets candidates $\Delta\phi$).[36]

4.2.3 Propagation of systematic uncertainties

The covariant matrices are evaluated using the so called pseudo-experiments, which combine both statistical and experimental systematic uncertainties including their correlations and correlations introduced by the unfolding procedure.[36] Detail description of pseudo-experiments can be found in Appendix J in [62].

4.3 Detector level plots

Let us now discuss the detector level distribution of all-hadronic $t\bar{t}$ pair decay. All presented plots are connected with the signal region, where both leading and subleading large-R = 1.0 anti-k_t jets were classified as top jet candidates. The first distributions can be seen in Fig. 4.1, where the multiplicity of jets are shown as main objects in the analysis. In Figs. 4.1(b) and 4.1(c), multiplicities of b-jets and large-R = 1.0 jets, respectively, are shown. It can be seen that an MC overestimates the data in all spectra of Fig. 4.1. Such an observation can be found also in the other experiments. This trend governs the whole analysis and it causes an overestimation of predicted differential cross section with respect to the data. In detail, 2015+2016 ATLAS data provides 3537 ± 59 $t\bar{t}$ pair all-hadronic events. This is approximately 20 % less than it was predicted (using the combination of data driven technique and MC

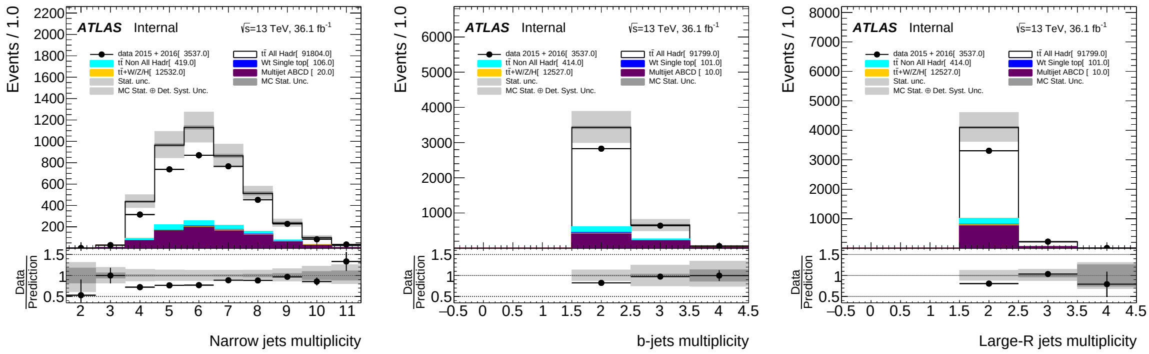

(a) (b) (c)

Figure 4.1: The jet multiplicity at detector level in the signal region: narrow $R = 0.4$ anti-k_t jets 4.1(a), anti-k_t $R = 0.4$ b-jets 4.1(b), large-$R = 1.0$ anti-k_t jets 4.1(c). The data containing the background are shown by black points. The theoretical signal prediction of the $t\bar{t}$ pair in all-hadronic decay is provided by POWHEG+PYTHIA. Color histograms represent predictions of background contributions while white histogram shows the sum of signal and background. The statistical uncertainty is shown by dark grey bands and the combination of statistical and detector systematic uncertainty is displayed by the light gray bands. The numbers of events normalized to the luminosity in data are shown in square brackets in the legend.

simulations). The prediction provides 4322 ± 35 events. The mentioned uncertainties of event yields are only statistical.

Let us continue with mass distributions, which can be found in Fig. 4.2. The mass distributions of leading and subleading large-R jets provide an expected mass peak around the top quark mass $m_{top} = 172.5$ GeV as it can be seen in Fig. 4.2(a) and Fig. 4.2(b).

Further the mass spectrum of the 3rd leading large-R jet is shown in Fig. 4.2(c). The 3rd leading large-R jet mass falls down without any suggestions of peaks or resonances predicted by Breight-Wigner distribution. It supports a fact that the 3rd leading large-R can not originate from the top quark but from another parent particle, probably from a gluon. This explanation is supported by the spectrum of k_t splitting scale $\sqrt{d_{12}}$ variable in Fig. 4.3(c). The massive decaying particles cause a symmetric shape of k_t splitting scale $\sqrt{d_{12}}$ around the half value of invariant mass of the parent particle. Exactly this dependence is seen for the leading and subleading Large-R jets in Fig. 4.3(a) and Fig. 4.3(b), while the 3rd leading large-R jet disposes with steeply falling and asymmetric distribution in Fig. 4.3(c) presumed to come from jets corresponding to light quarks or gluon.

In addition, there are also mass distributions of first subjets in those large-R jets (see Figs. 4.2(d) and 4.2(e)). The subjets are parametrised as small-$R = 0.4$ anti-k_t jets. Namely there are first subjet in the leading large-R jet and first small-R subjet in the subleading large-R jet. The term first subjet means the subjet with the highest p_t in whole jet. The provided mass distribution of the first subjet in leading and subleading large-R jets shows an obvious mass peak of W boson around the mass $m_W \approx 80$ GeV. Although there is also a visible second peak at low mass scale around 25 GeV, the peak was not identified unambiguously. It may be a resonance, however this peak is still predicted by the MC simulation. Consequently, we make a conclusion that the peak is created artificially due the event selection criteria in the analysis.

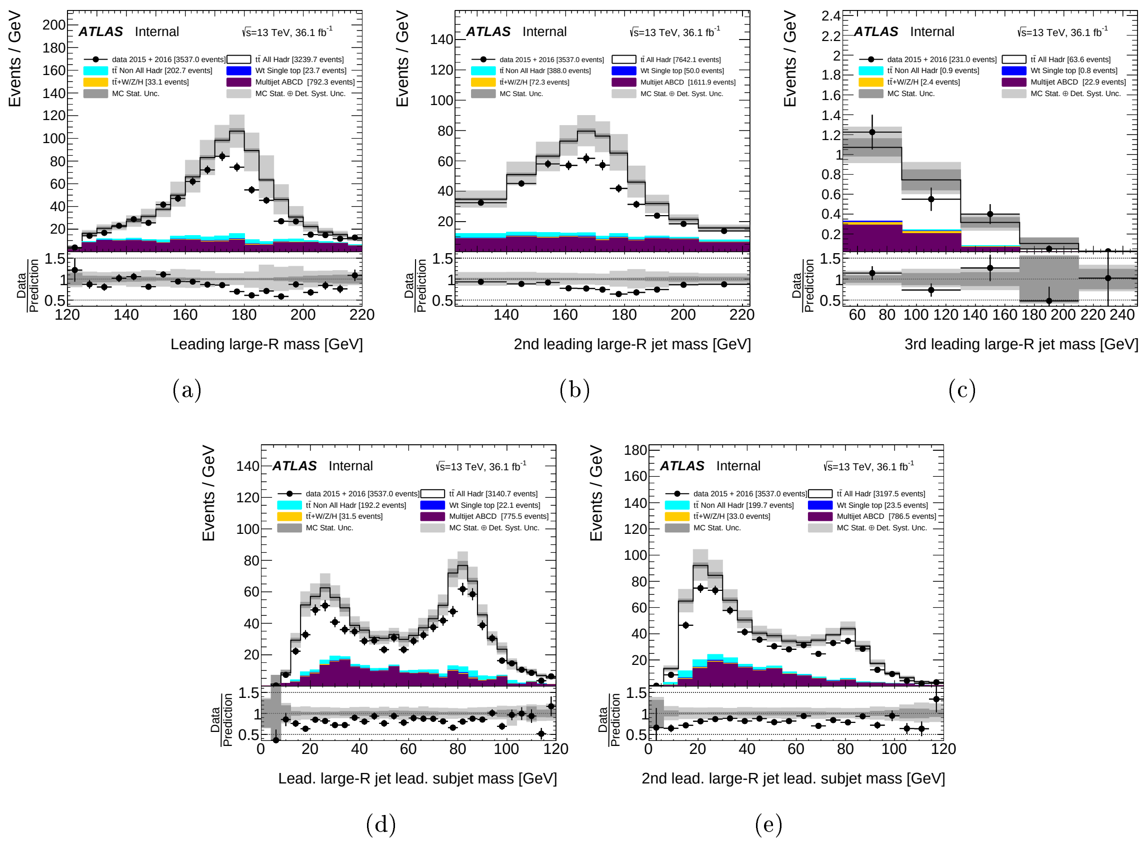

Figure 4.2: The jet mass at detector level in the signal region: leading large-R jet 4.2(a), subleading large-R jet 4.2(b) and 3rd leading large-R jet 4.2(c), first small-R subjet in leading large-R jet 4.2(d) and first small-R subjet in subleading large-R jet 4.2(e). The data containing the background are shown by black points. The theoretical signal prediction of the $t\bar{t}$ pair in all-hadronic decay is provided by POWHEG+PYTHIA. Color histograms represent predictions of background contributions while white histogram shows the sum of signal and background. The statistical uncertainty is shown by dark grey bands and the combination of statistical and detector systematic uncertainty is displayed by the light gray bands. The numbers of events normalized to the luminosity in data are shown in square brackets in the legend.

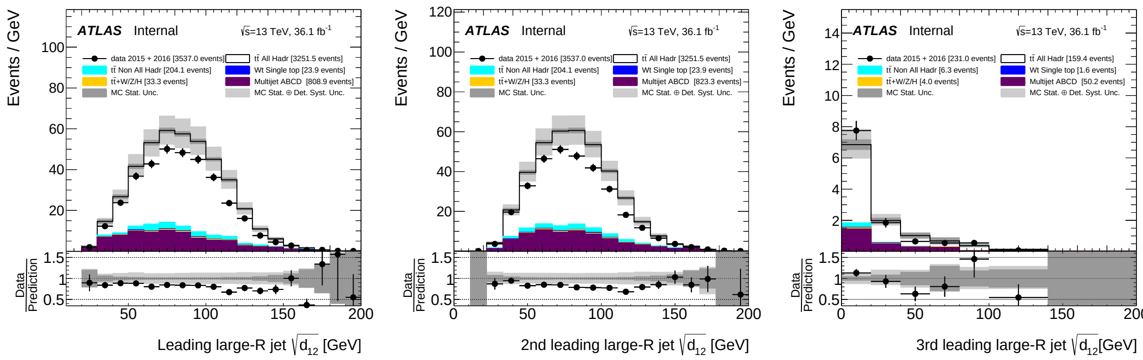

(a) (b) (c)

Figure 4.3: The jet splitting scale $\sqrt{d_{12}}$ at detector level in the signal region for: leading large-R jet 4.3(a), subleading large-R jet 4.3(b) and 3rd leading large-R jet 4.3(c). The data containing the background are shown by black points. The theoretical signal prediction of the $t\bar{t}$ pair in all-hadronic decay is provided by POWHEG+PYTHIA. Color histograms represent predictions of background contributions while white histogram shows the sum of signal and background. The statistical uncertainty is shown by dark grey bands and the combination of statistical and detector systematic uncertainty is displayed by the light gray bands. The numbers of events normalized to the luminosity in data are shown in square brackets in the legend.

4.4 Analysis of re-clustered jets

The application of re-clustered jets for data analysis forms the main part of the thesis. The section describes an implementation of re-clustering procedure into the ttbar analysis framework and it provides a description of an analogical analysis simultaneously, as it was discussed above, to investigate changes in the systematic uncertainties.

This section introduces a notation *original* for objects of interest involved in the original $t\bar{t}$ pair analysis, which was described in previous sections. The large-R jets in the previous analysis are called *the original large-R jets* to distinguish *re-clustered large-R jets* arising from the re-clustering procedure. The set of small-R jets remains the same for both analyses.

4.4.1 The re-clustering

The original small-R = 0.4 anti-k_t jets are used for the re-clustering first. The small-R jets were clustered again using the anti-k_t algorithm and jet radius R = 1.0 was used to construct new re-clustered large-R jets. The anti-k_t clustering algorithm was implemented using `FASTJET` package [63]. The re-clustering method was implemented following the ATLAS note [30].

Since systematic uncertainties of jets with R = 0.4 are usually smaller than those for R = 1.0, one believes that they will also be smaller for re-clustered jets, since they are propagated during the re-clustering procedure, as well as calibrations. Such new re-clustered large-R jets are tested subsequently in a similar way as it was described in section 4.1. However, it was necessary to implement a few changes in the event selection as will be explained below.

4.4.2 The selection criteria modifications

All objects for the data analysis are taken from samples, which do not provide full information about the events. For example, tracks, vertices and constituent particles are not present. Thus the variables reflecting an inner structure of jets can not be calculated exactly. An example of such variables is a ratio of N-subjetiness: τ_{32} variable, which is necessary for the top-tagging. In other words, the top-tagger is not performed with re-clustered jets. Thus τ_{32}, τ_{21} variables as well as the top-tagging informations have to be inherited from the original large-R jets.

If a new re-clustered large-R jet can be matched with the original large-R jet according to a quite small angular separation $\Delta R < 0.25$, then the values of τ_{32}, τ_{21} variables and top-tagging information of the original large-R jet are inherited by re-clustered large-R jet. Such modifications may cause a bias and a modification of the fiducial phase space evidently.

The comparison of data cut flows can be found in Fig. 4.4 for both analyses involving the original and re-clustered large-R jets. Only most important selection criteria are shown in Fig. 4.4. Last four bins in the data cut flows are identified with the top-tagging requirements of leading and sub-leading large-R jets. The top-tagging artificial variable t reaches two possible values true or false: $t \in \{0, 1\}$. The first two characters are connected with leading large-R jet, whereas third and fourth characters belong to the subleading large-R jet. So, $1t1t$ denotes the signal region, where both leading and subleading jets are top-tagged.

We observe that the re-clustering increases the event yield in the signal region by 27 %. The reason of such increase is rather difficult to find mainly because of the possible bias mentioned above. The unbiased approach would be to identify top-jet candidates using a top-tagger based directly on re-clustered jets. Some explanations may be given by taking into account the following:

- the phase space may have changed due to modified selection criteria as explained above
- the efficiency of the trimming procedure and pile-up subtraction for re-clustered jets has not yet been studied to see if it stays similar as for the original jets
- as it will be shown later, the re-clustering decreases the mean p_t of jets and make the p_t spectrum narrower
- the energy, p_t and mass of a re-clustered jets is calculated using information about whole small-R jets, not from their constituents, which means that in principle this small-R jets lie outside the $R = 1.0$ distance from the re-clustered jet
- jet structure variable τ_{32}, τ_{21} used in the top tagger are calculated from the original large-R jets

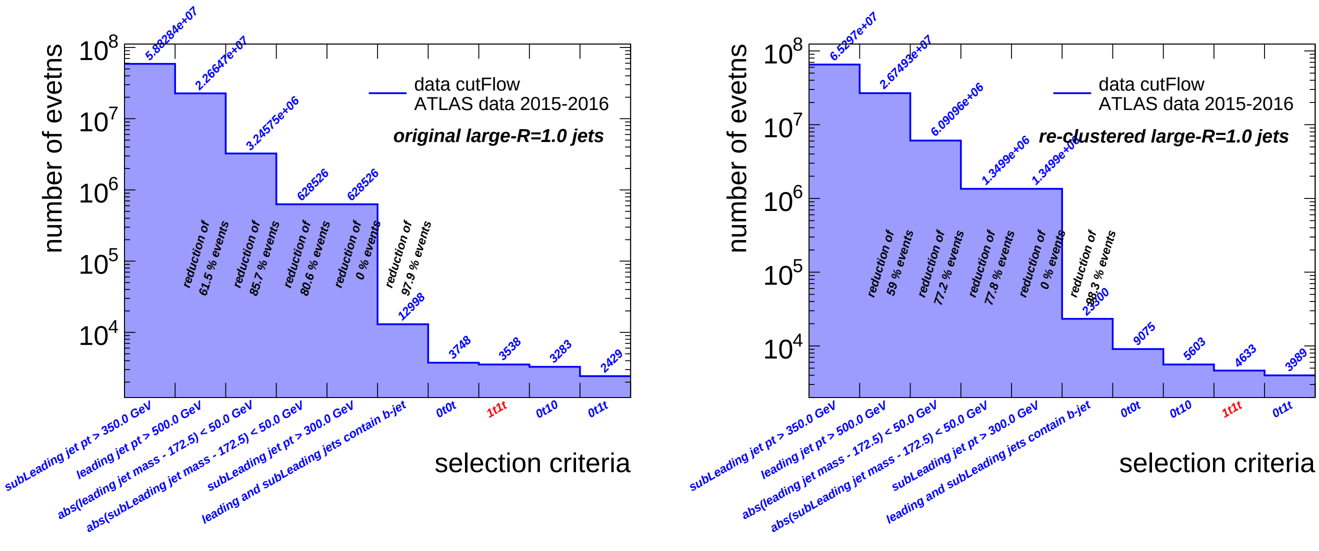

(a) (b)

Figure 4.4: Data cut flow for the all-hadronical $t\bar{t}$ pair analysis: for the original analysis 4.4(a) and the analysis of re-clustered large-R jets 4.4(b).

An increase of event yields is documented in detail in Tabs. 4.4 and 4.5. The tables compare the event yields in data and prediction, which consists of the $t\bar{t}$ all-hadronic signal and all relevant background sources for both original and re-clustered large-R jets.

data/sample	yield	±	err.
$t\bar{t}$ All hadronic	3251	±	16
$t\bar{t}$ non-All hadronic	204	±	12
Wt single top	23	±	3
$t\bar{t}$ + H/W/Z	33	±	1
Multijet events	809	±	28
Prediction	4322	±	35
data (36.1 fb^{-1})	3537	±	59

Table 4.4: Event yields with statistical uncertainties for original large-R jets.

data/sample	yield	±	err.
$t\bar{t}$ All hadronic	3632	±	17
$t\bar{t}$ non-All hadronic	223	±	13
Wt single top	28	±	3
$t\bar{t}$ + H/W/Z	34	±	1
Multijet events	1011	±	24
Prediction	4928	±	32
data (36.1 fb^{-1})	4632	±	68

Table 4.5: Event yields with statistical uncertainties for re-clustered large-R jets.

4.4.3 Comparison of plots at detector level

This section deals with a comparison of kinematic distributions at detector level between the original and the re-clustered large-R jets. All shown spectra represent the results in the signal region of $t\bar{t}$ all-hadronic channel.

A very useful information on the effect of re-clustering procedure is brought by comparing mass spectra of the leading (Figs 4.5(a) and 4.5(b)) and subleading Large-R jets (Fig. 4.5(c) and 4.5(d)) at detector level. The prediction of $t\bar{t}$ signal and all relevant backgrounds are summed together into one stack. The same variable, now for individual contributions of the data, signal and multijet background are shown in Fig. 4.6(a) for leading and 4.6(b) for subleading jets.

From Figs.4.5 we conclude that re-clustered jets show a better agreement between the data and prediction. The MC predictions are found to agree with data within the ranges of total uncertainties at the measured mass range. Re-clustered jets provide a more stable ratio of the data with respect to the prediction meaning that no holes or excessive deflections from unity are observed in the ratio plots in the case of re-clustered jets. In addition the mass peak became narrower for re-clustered jets. The re-clustered jets also provide less multijet background at the lower edge of the mass spectra.

An increase of statistic in data and signal can also be seen in Fig 4.6. In addition, the mass peak of re-clustered jets moves to higher values consistently. Namely the mean mass of re-clustered jets moves about +10 GeV in data and +5 GeV in signal in case of leading large-R jet. In similar way the subleading re-clustered large-R jet mass distribution moved by +5 GeV for both data and signal.

The comparison of detector p_t spectra can be found in Figs. 4.7 4.8 for leading as well as subleading large-R top-jet candidates. A detail comparison of data, signal and multijet backgound distributions shows Figs. 4.8(a) and 4.8(b), where it can be seen, that the re-clustered jet provides higher yield of events at low p_t range, whereas the event yields became lower at higher p_t range in comparison with original large-R jets. Further, the re-clustered jets provide a narrower and higher "peak" in p_t specta of subleading top-jet candidate in Fig. 4.8(b).

The rapidity distributions are show in Figs. 4.9 4.10. Here, again a better agreement between the data and prediction have been reached. In addition, an increased statistic of data can be seen in ratio plots in Figs. 4.10(a) 4.10(b).

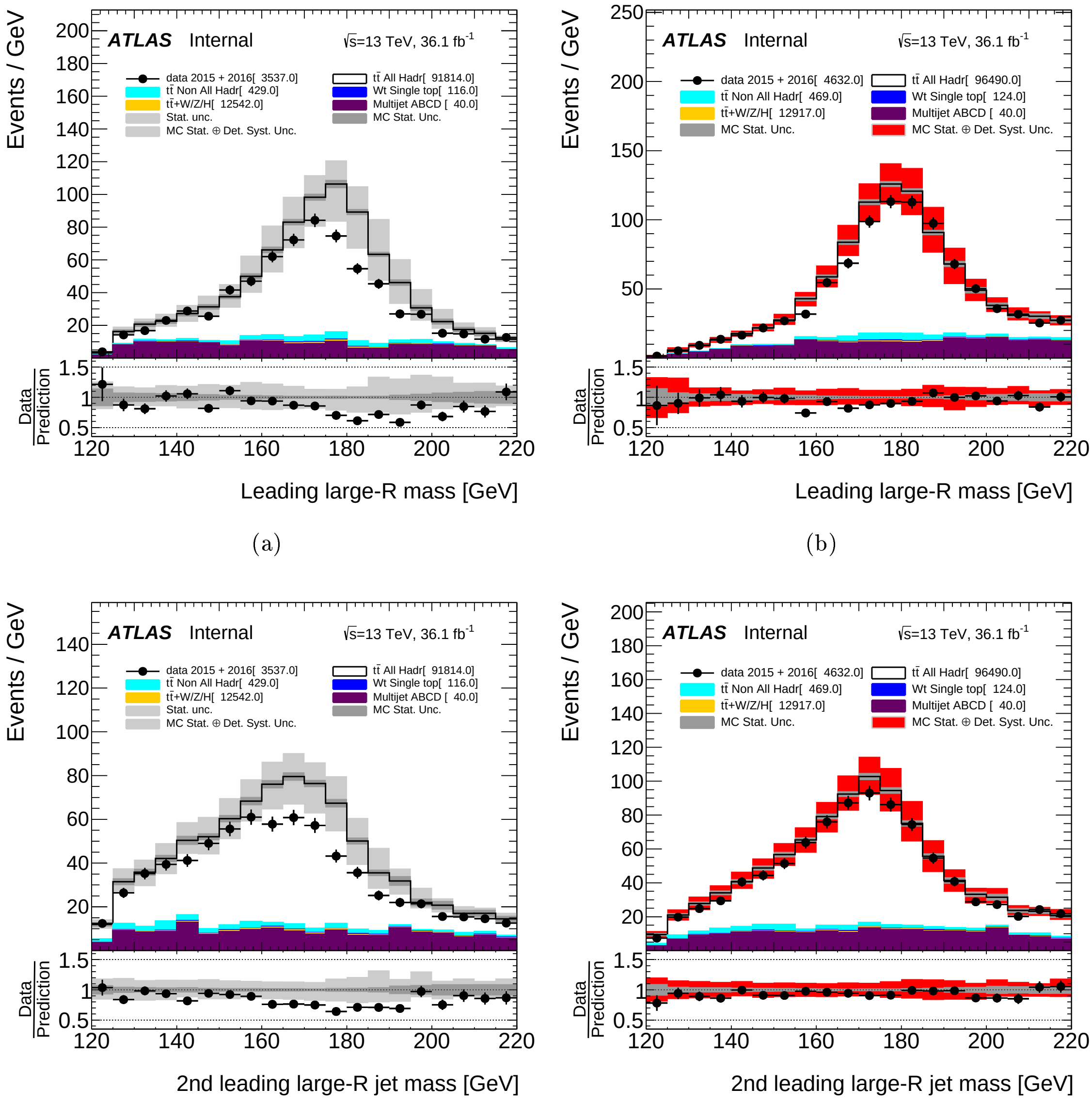

(d)

Figure 4.5: The comparison of jet mass spectra of the original (a) and re-clustered (b) leading large-R jets at detector level in the signal region. Similarly for the subleading large-R jets, the original jets are shown in (c), the re-clustered in (d).

4.4.4 Comparison at particle level

This section discusses a comparison of original and re-clustered jets at particle level. The main purpose of the section is to check that the unfolding procedure is under control also for the re-clustered jets. The Bayesian iterative unfolding with four iterations was applied on the data after the background subtraction.

The rapidity of the $t\bar{t}$ system and p_t of leading top-quark jet (leading top-jet candidate in a signal region) were chosen as two illustrative candidates for the comparison. The comparison of smearing matrices and correction factors of acceptance and efficiency can be found in Figs. 4.11 and 4.12 for both observables. The smearing matrices of re-clustered jets become slightly more diagonal. It causes less migration of events between neighbouring bins. The comparison of acceptance and efficiency is shown for the nominal sample Powheg+Pythia8. Both corrections factors are a little bit lower for re-clustered jets in general.

The unfolded data are shown in Figs. 4.13 and 4.14, where differential cross section as a function of $|y^{t\bar{t}}|$ and $p_t^{t,1}$ can be found. Re-clustered jets provide a better agreement between

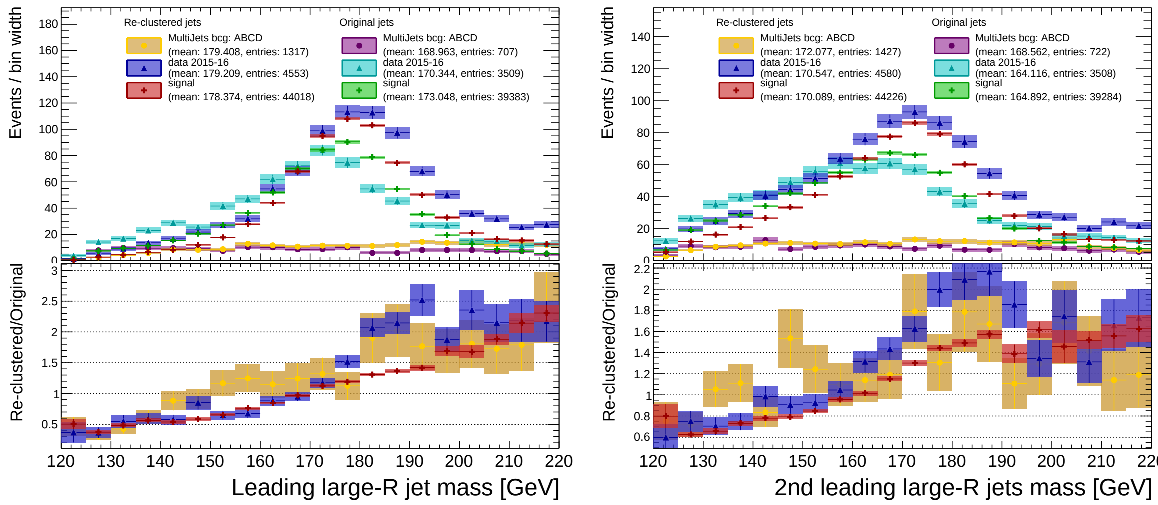

(a) (b)

Figure 4.6: A detailed comparison of jet mass spectra of the original and re-cluster large-R jets for leading large-R jet 4.6(a) and subleading large-R jet 4.6(b) for data, signal and multijet background.

data and all considered predictions including the nominal prediction of Powheg+Pythia8. Similarly, better agreement was observed also for other observables, which are not published here. Considering the ratio plot of $|y^{t\bar{t}}|$ in fig. 4.13(a), the original large-R jets predictions gave higher cross sections with respect data, while this trend has vanished for re-clustered jets in Fig. 4.13(b).

4.4.5 Comparison of systematic uncertainties at particle level

This section deals with the comparison of systematic uncertainties, which are considered in the differential cross sections at particle level. The systematic uncertainties were shortly described in section 4.2. The most significant uncertainties were collected into the following seven groups:

- Large-R jet energy scale and Tagging (JES + TopTagging)
- Flavour tagging
- Hard scattering
- Parton shower
- MC stat. uncertainties
- Stat. uncertainties
- Total uncertainties

The other uncertainties amount to less than 1 % and they are not listed here. Although they are considered in the evaluation of the Total uncertainty.

The comparison of relative uncertainties associated with differential cross section at particle level (in Figs. 4.13 and 4.14) as a function of the rapidity of the $t\bar{t}$ system and leading top-quark p_t can be found in Figs. 4.15 and 4.16. Figs. 4.15(c) and 4.16(c) show ratios of relative JES+Top Tagging and total uncertainties of re-clustered to original jets since the JES+Top Tagging uncertainty is the dominant source.

The steps in Fig. 4.16(c) in Total uncertainty are caused by fluctuation of Hard scattering because of low statistics and improper modelling of some variables as it was mentioned in section 4.2. If we omit the contribution of Hard scattering, then we see approximately 15–20 % improvement of Total and JES+Top tagging systematic, which is almost independent off $t\bar{t}$

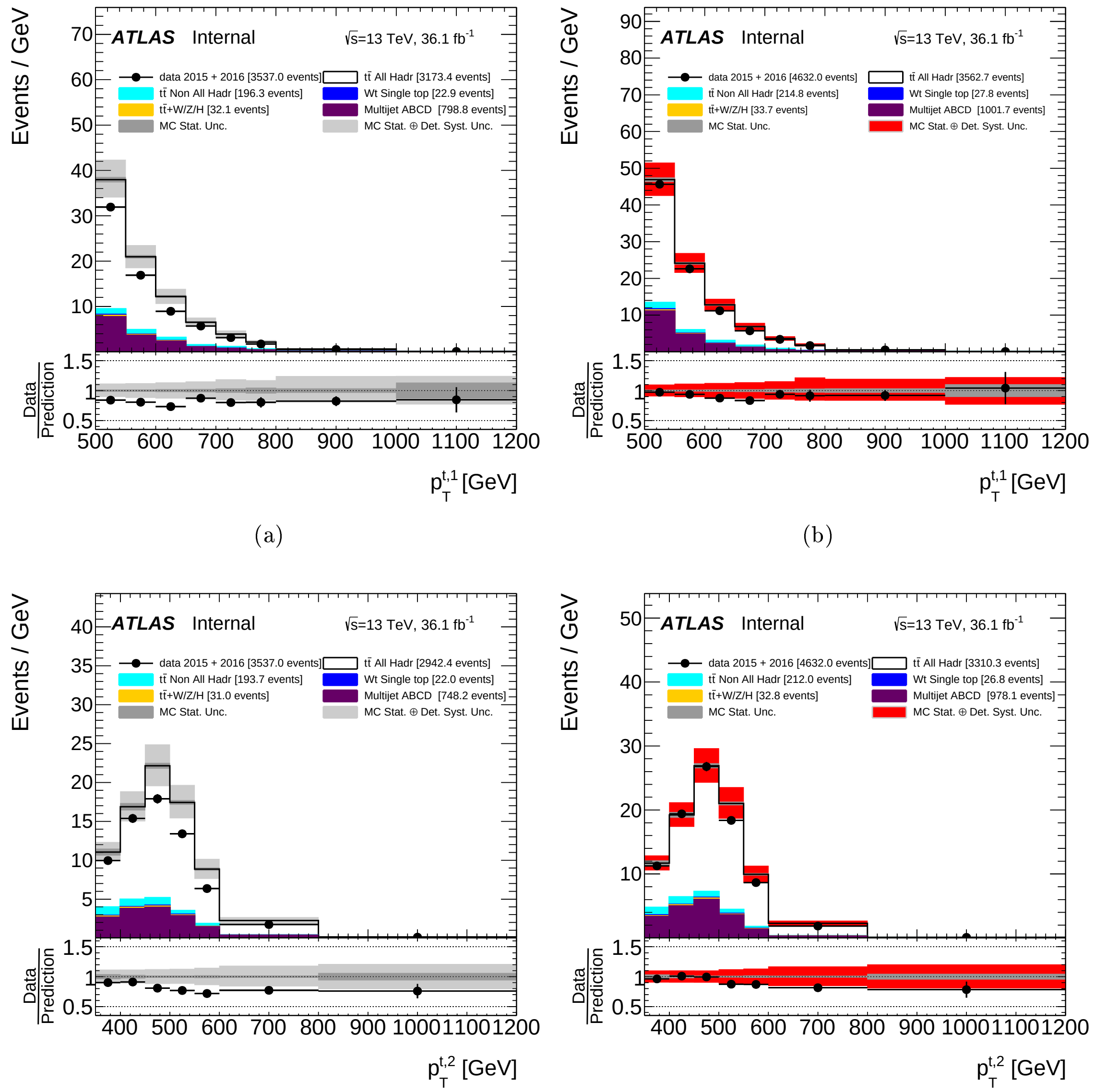

(c) (d)

Figure 4.7: The comparison of jet p_t spectra of the original (a) and re-clustered (b) leading large-R jets at detector level in the signal region. Similarly for the subleading large-R jets, the original jets are shown in (c), the re-clustered in (d).

system rapidity $|y|^{t\bar{t}}$ as well as p_t of leading top-quark jet $p_t^{t,1}$. Other ratios of Total and Large-R jets systematic continue in Figs. 4.17, and 4.18. The results provide a consistent global improvement not only for presented variables but also for the other observables such as p_t, y of random top quark, which is introduced because one is not able to distinguish top quark from anti-top quark presently in the data.

[1] $\chi^{t\bar{t}}$ variable is defined as follows: $\chi^{t\bar{t}} = e^{2|y^{\star}|}$, where $y^{\star}$ is a rapidity of $t\bar{t}$ system in central mass frame, so $y^{\star} = \frac{1}{2}\left(y^{t,1} - y^{t,2}\right)$

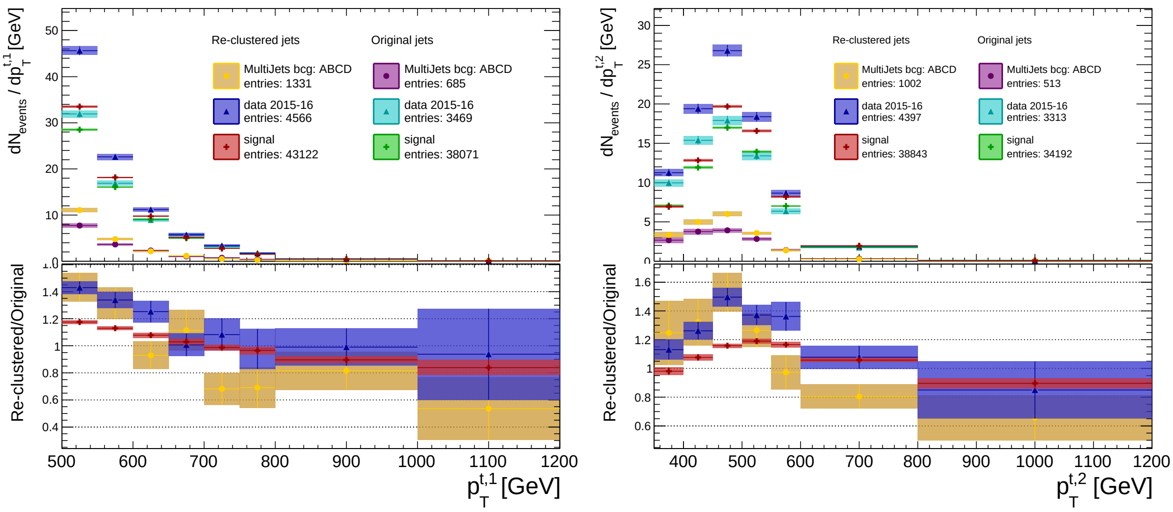

(a) (b)

Figure 4.8: A detailed comparison of jet p_t spectra of the original and re-cluster large-R jets for leading large-R jet 4.8(a) and subleading large-R jet 4.8(b) for data, signal and multijet background.

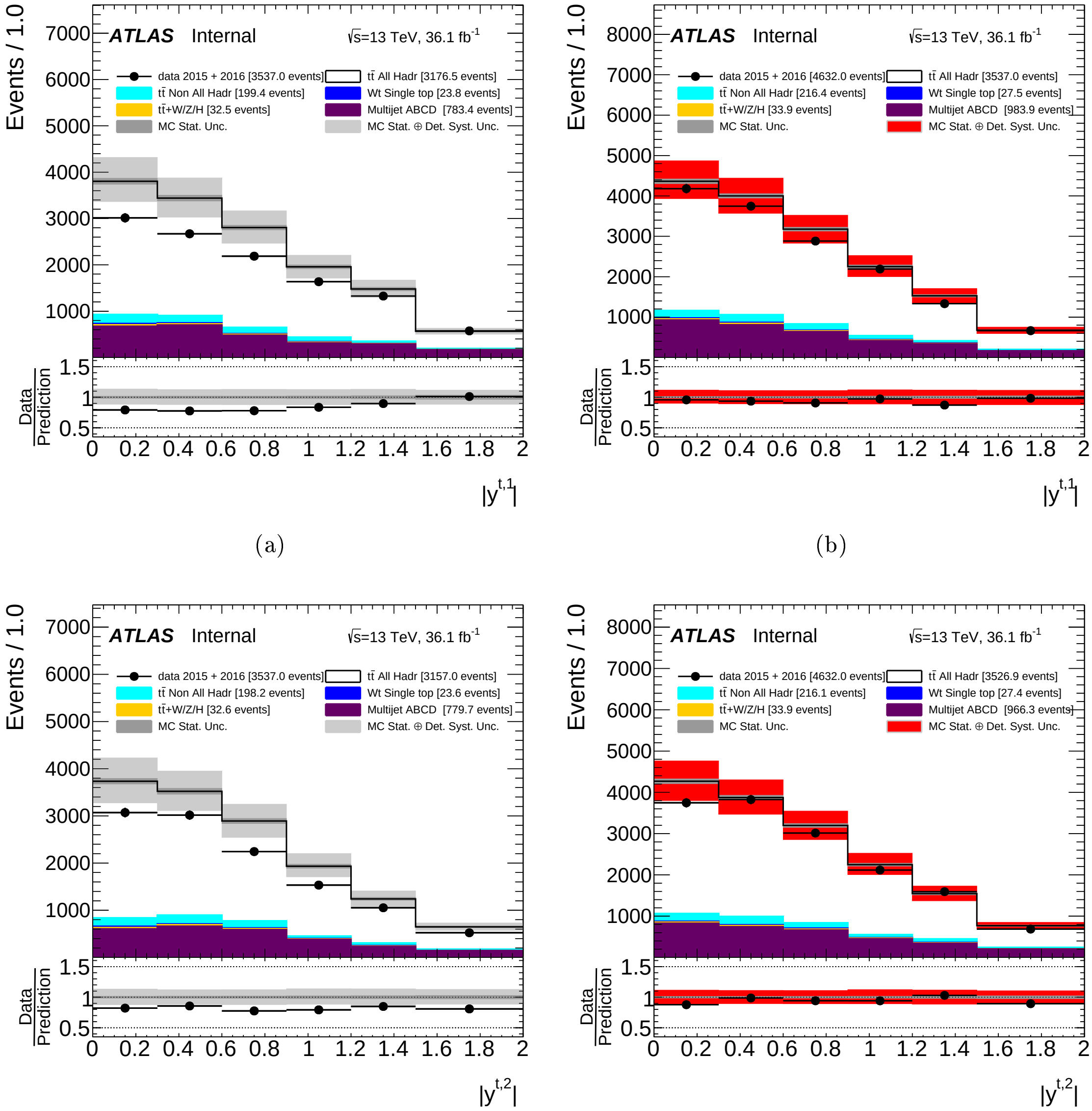

(a) (b)

(c) (d)

Figure 4.9: The comparison of jet rapidity spectra of the original (a) and re-clustered (b) leading large-R jets at detector level in the signal region. Similarly for the subleading large-R jets, the original jets are shown in (c), the re-clustered in (d).

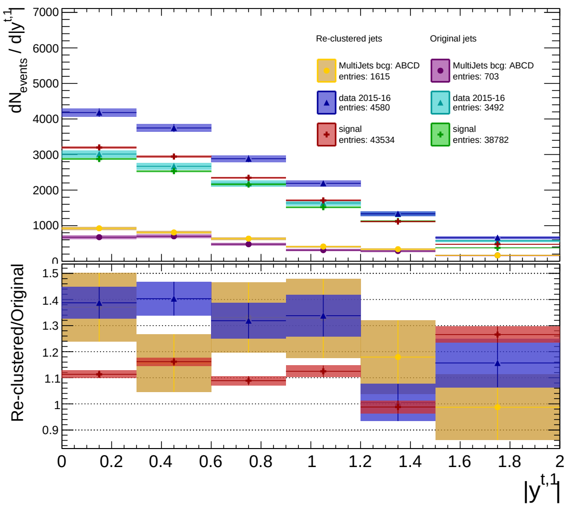

(a)

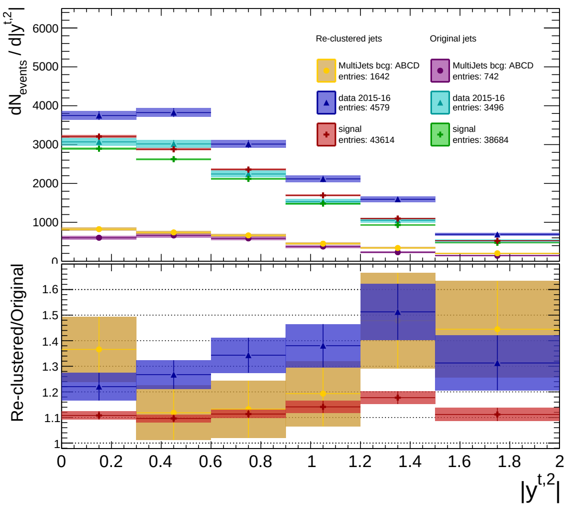

(b)

Figure 4.10: A detailed comparison of jet rapidity spectra of the original and re-cluster large-R jets for leading large-R jet 4.10(a) and subleading large-R jet 4.10(b) for data, signal and multijet background.

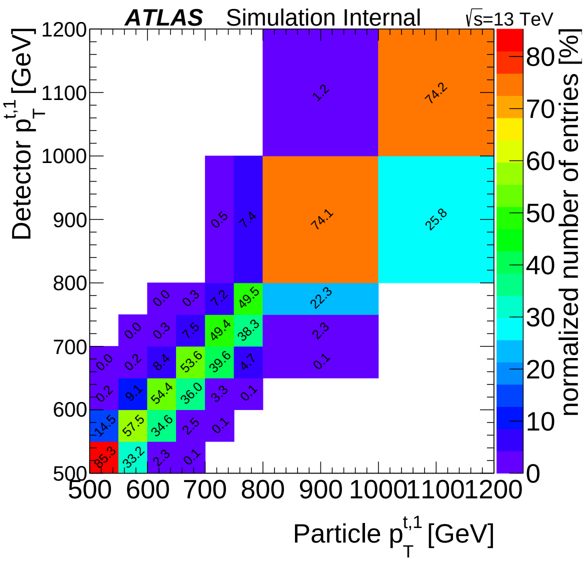

(a)

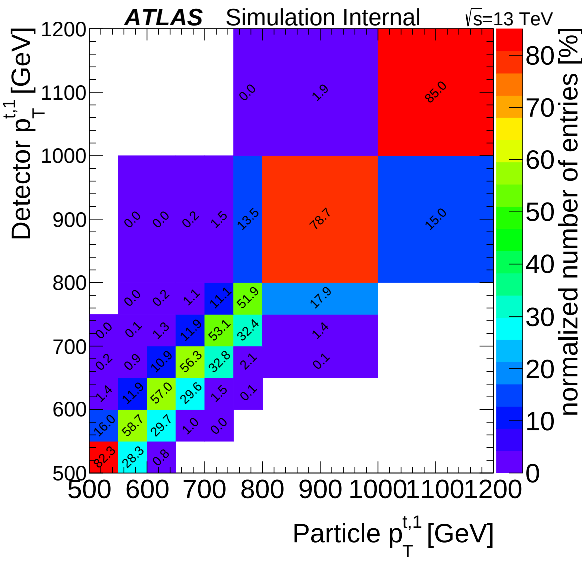

(b)

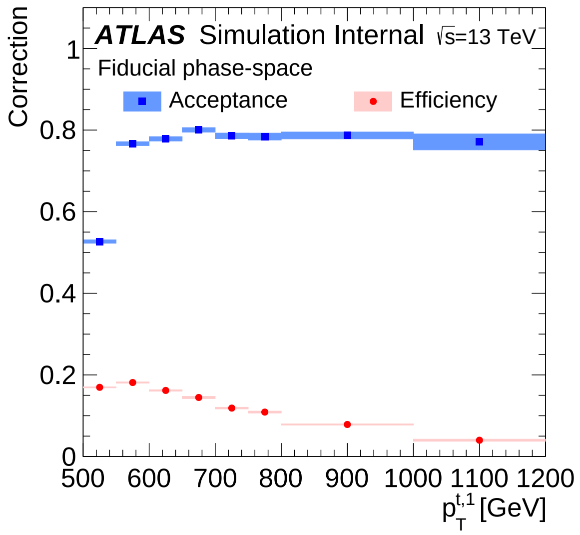

(c)

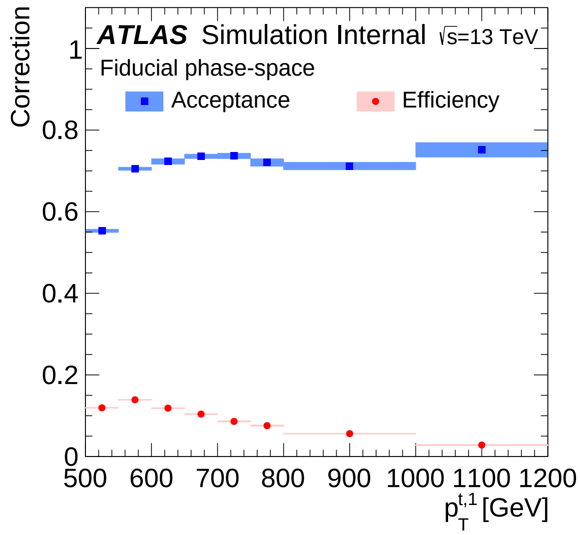

(d)

Figure 4.11: A comparison of unfolding procedure of the original and re-cluster large-R jets for variable: p_t of leading top-quark jet $p_t^{t,1}$. The smearing matrix of the original analysis is shown in 4.11(a) and its acceptance and efficiency corrections in 4.11(c) to be compared with smearing matrix of re-clustered jets in 4.11(b) and corresponding acceptance, efficiency corrections in 4.11(d). The acceptance and efficiency corrections are derived from the nominal sample of Powheg+Pythia8.

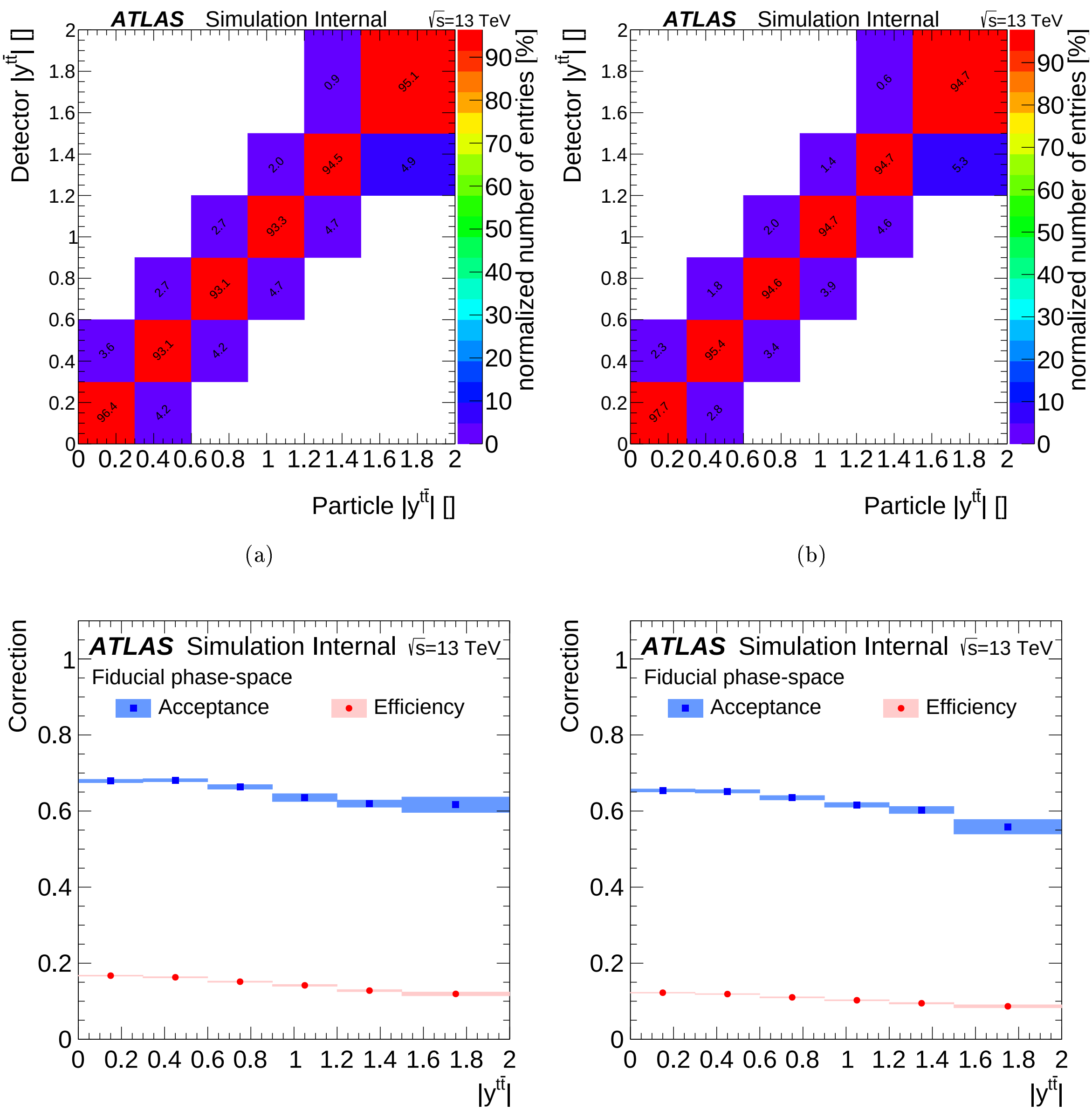

(a) (b) (c) (d)

Figure 4.12: A comparison of unfolding procedure of the original and re-cluster large-R jets for variable: rapidity of the $t\bar{t}$ system $|y^{t\bar{t}}|$. The smearing matrix of the original analysis is shown in 4.12(a) and its acceptance and efficiency corrections in 4.12(c) to be compared with smearing matrix of re-clustered jets in 4.12(b) and corresponding acceptance, efficiency corrections in 4.12(d). The acceptance and efficiency corrections are derived from the nominal sample of Powheg+Pythia8.

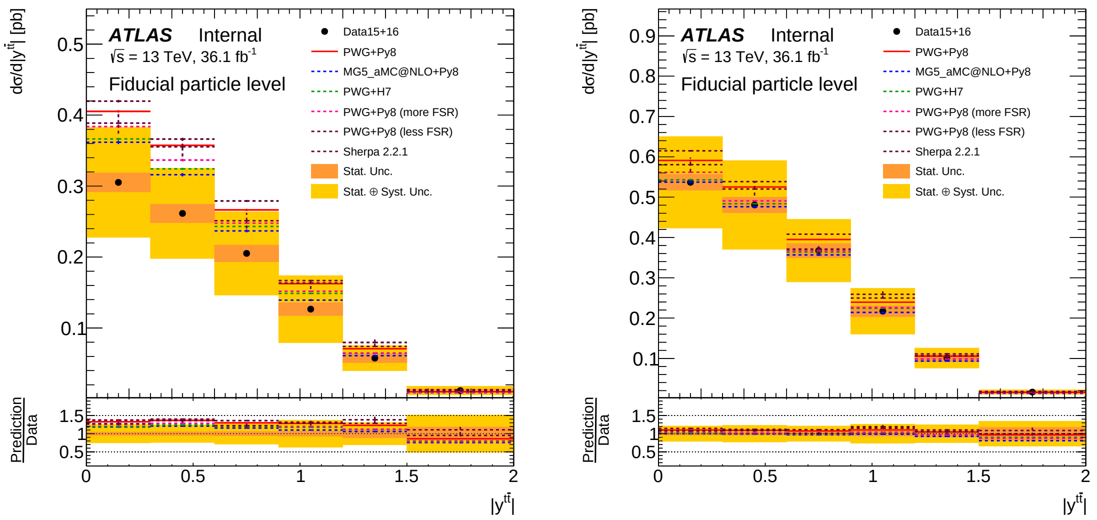

(a) (b)

Figure 4.13: A comparison of differential cross section as a function of the $t\bar{t}$ system rapidity for original 4.13(a) and re-cluster large-R jets 4.13(b) at particle level. Data are shown by black points and compared with red line of nominal prediction of Powheg+Pythia8 and other Monte Carlo predictions, namely: blue line of MadGraph_aMC@NLO+Pythia8 (modification of Matrix element), green line of Powheg+Herwig7 (modification of parton shower and hadronisation models), pink and brown lines of Powheg+Pythia8 (modification of final state radiation).

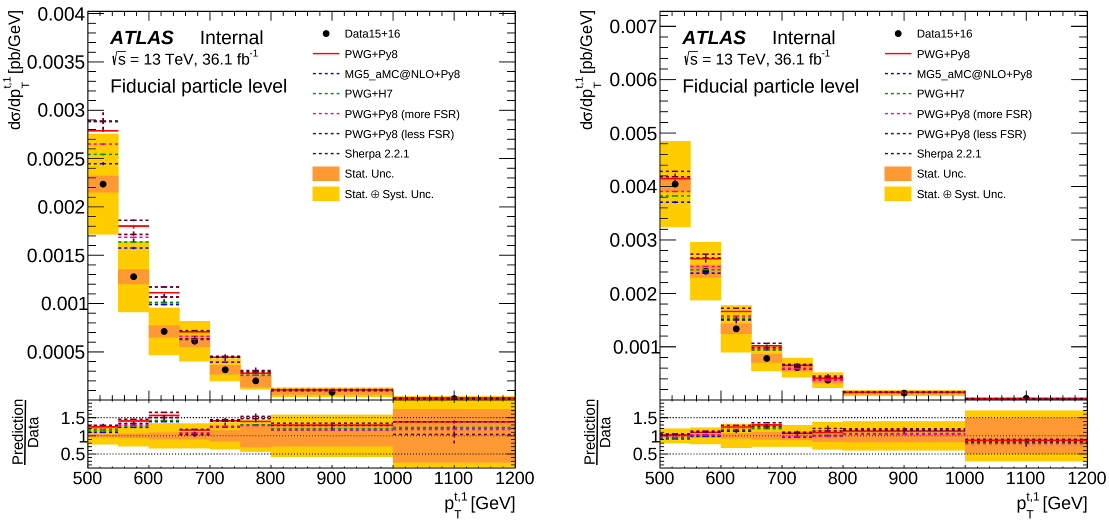

(a) (b)

Figure 4.14: A comparison of differential cross section as a function of the leading top-quark p_t for original 4.14(a) and re-cluster large-R jets 4.14(b) at particle level. Data are shown by black points and compared with red line of nominal prediction of Powheg+Pythia8 and other Monte Carlo predictions, namely: blue line of MadGraph_aMC@NLO+Pythia8 (modification of Matrix element), green line of Powheg+Herwig7 (modification of parton shower and hadronisation models), pink and brown lines of Powheg+Pythia8 (modification of final state radiation).

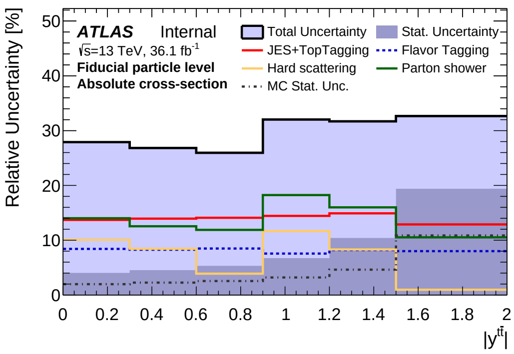

(a)

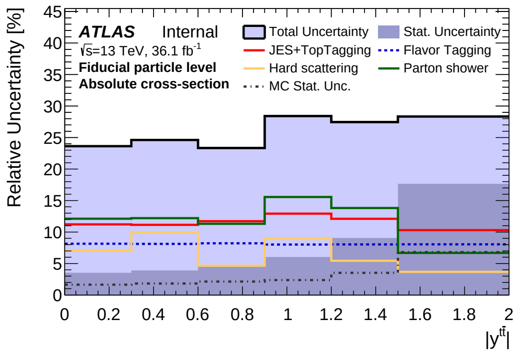

(b)

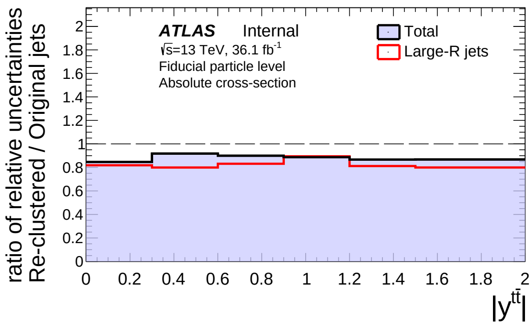

(c)

Figure 4.15: A comparison of relative systematic uncertainties for the $t\bar{t}$ system rapidity of the original 4.15(a), re-cluster large-R jets 4.15(b) and ratio of re-clustered to original large-R jets for the Total Uncertainty and JES+TopTagging uncertainty 4.15(c).

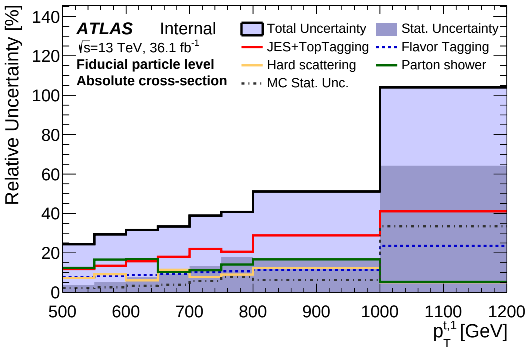

(a)

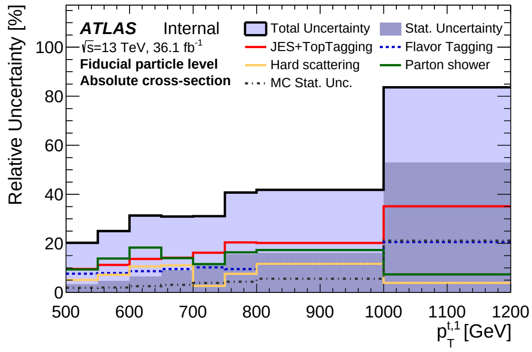

(b)

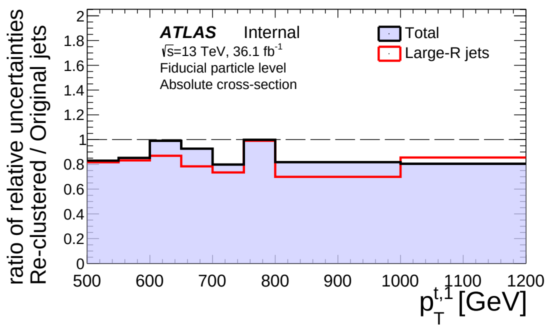

(c)

Figure 4.16: A comparison of relative systematic uncertainties for the leading top-quark p_t of the original 4.16(a), re-cluster large-R jets 4.16(b) and ratio of re-clustered to original large-R jets for the Total Uncertainty and JES+TopTagging uncertainty 4.16(c).

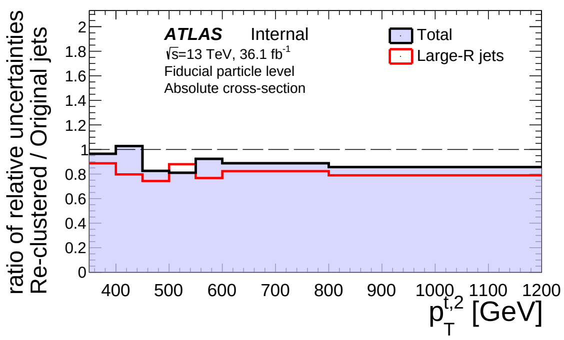

(a)

Figure 4.17: Relative Total and relative JES+TopTagging uncertainty ratios of re-clustered and original large-R jets for subleading top-quark p_t 4.17(a).

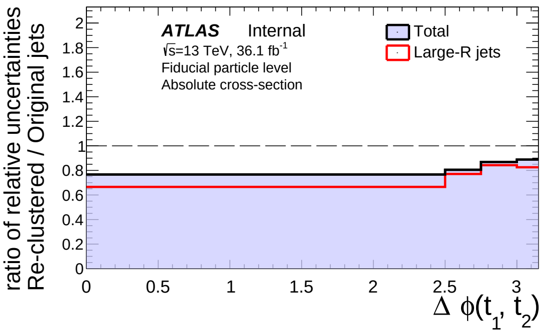

(a)

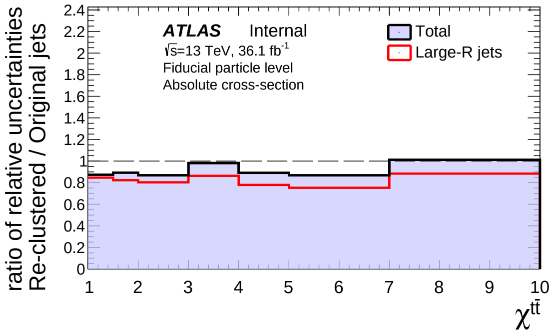

(b)

Figure 4.18: Relative Total and relative JES+TopTagging uncertainty ratios of re-clustered and original large-R jets for: azimuthal angle between both leading and subleading top-quark 4.18(a), $\chi^{t\bar{t}}$ variable 4.18(b) defined in the text[1].

Chapter 5

Z' sample analysis

The $t\bar{t}$ pair can originate also as a decay product of the hypothetical Z' boson, a particle predicted by an extend electroweak symmetry theory beyond the Standard Model. The Z' boson is classified as a spin-1 boson with neutral electric charge just like the Z bosons in the original electroweak theory of Standard Model. The Z' boson appears in many scenarios beyond Standard Model such as superstring-inspired models, grand unified models or models involving extra dimensions, all unified into one term: New Physics (NP). [65] [64]

The study is based on the framework used in the working group *Differential ttbar cross-sections at 13 TeV all-hadronic boosted group* and described in the previous chapter. Since the existence of the Z' boson can emerge from new terms of the Standard Model interaction Lagrangian, new Monte Carlo samples of events were generated based only on these new terms. We have studied 14 different mass points, ranging from 400 to 5000 GeV. However we are showing only results for four of them, which are most relevant for the current study: 1500, 2000, 2250 and 2750 GeV. The reason is that LHC data set lower mass thresholds as follows:

- $\tau^+\tau^-$ channel at 8 TeV data: 2.0 TeV
- $e^\pm\tau^\mp$ and $\mu^\pm\tau^\mp$ channel at 8 TeV data: 2.2 TeV
- $t\bar{t}$ channel at 8 TeV data: $2 - 2.5$ TeV
- jj channel at 13 TeV data: 1.5 TeV

Thus we have decided to focus on Monte Carlo samples with predicted $m_{Z'} \geq 1.5$ TeV. The region above $m_{Z'} = 3000$ GeV is not studied because of the fiducial region of the current analysis ends around masses of 3000 GeV.

All prepared comparisons are done using the re-clustered large-$R = 1.0$ jets, which are identified with the top quarks as it was described in chapter 4. The presented distributions are shown at detector level.

Figs. 5.1, 5.2 and 5.3 show absolute cross sections as functions of mass, rapidity and p_t of the $t\bar{t}$ system in a linear and logarithmic scales.

The comparison of the uncorrected data with predictions of models including New Physics is done in the following way. Since the NP terms are extra terms in the SM Lagrangian, we sum the existing Powheg+Pythia8 signal sample with the new NP samples generated by Pythia8 at a given mass point. This sum is then compared with the data. The background predictions stay the same as in the previous analysis.

Again, the mass, p_t and rapidity of the $t\bar{t}$ system are chosen for this comparative study in Figs.5.4, 5.5 and 5.6. From this comparison we conclude that the sum of SM and NP prediction does not give a better description of the data hence a signal of New Physics is not observed for the $t\bar{t}$ final state decaying fully hadronically in the studied kinematic region of $1 - 3$ TeV.

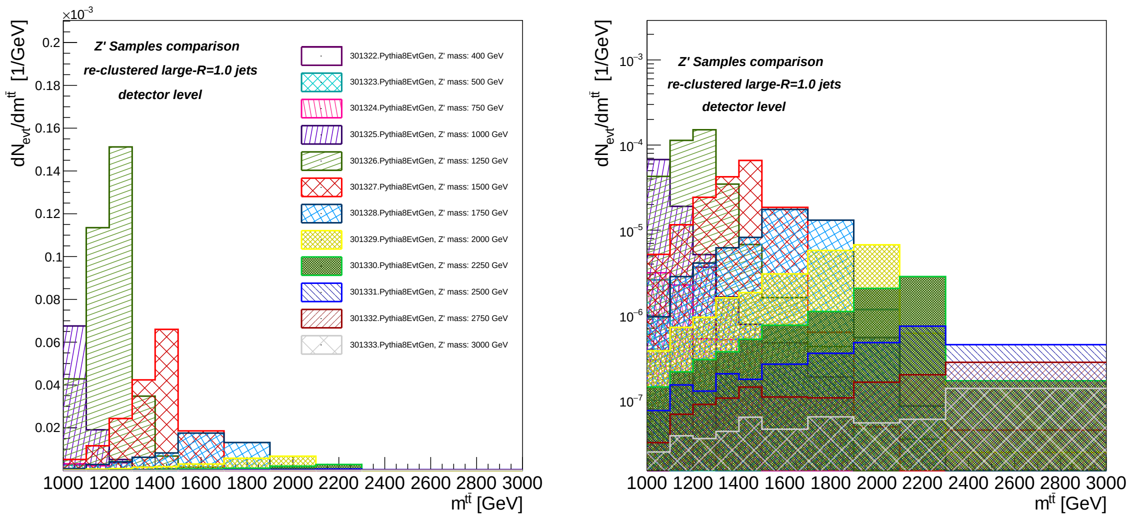

Figure 5.1: PYTHIA 8 predictions of absolute spectra of the mass of the $t\bar{t}$ system, $m^{t\bar{t}}$, for 12 of 14 generated $m_{Z'}$ mass points in linear scale (a) and logarithmic scale (b).

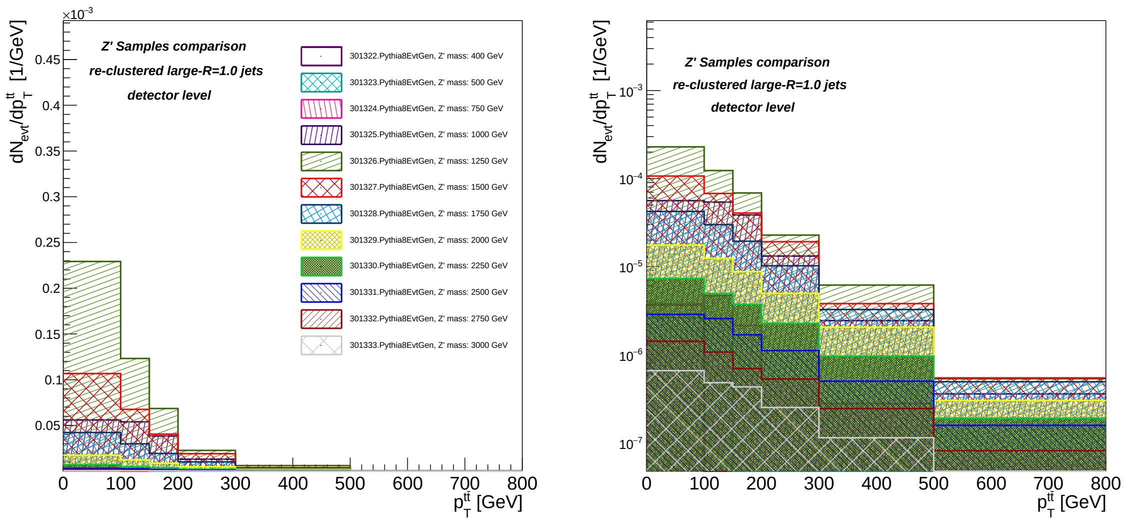

Figure 5.2: PYTHIA 8 predictions of absolute spectra of the p_t of the $t\bar{t}$ system, $p_t^{t\bar{t}}$, for 12 of 14 generated $m_{Z'}$ mass points in linear scale (a) and logarithmic scale (b).

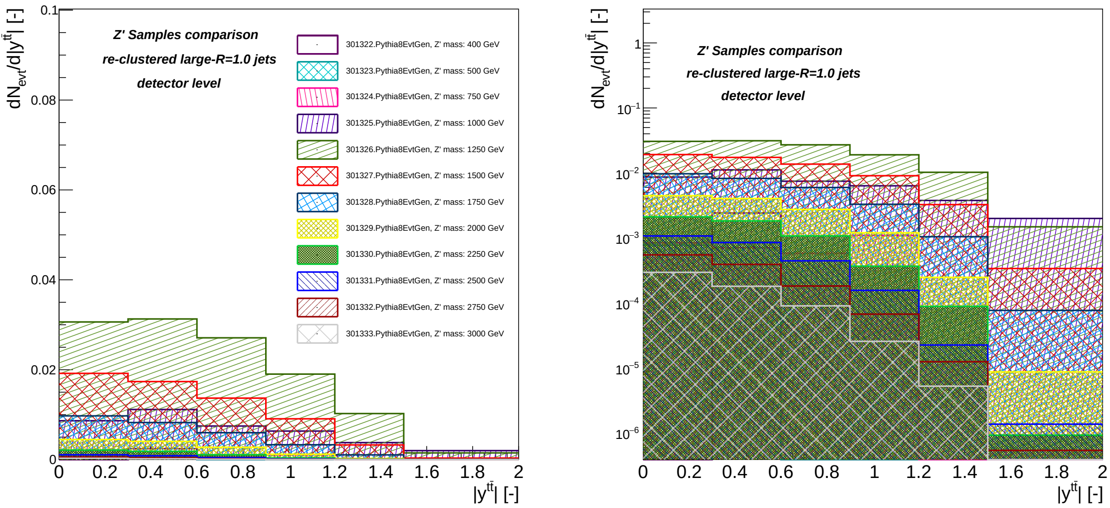

Figure 5.3: PYTHIA 8 predictions of absolute spectra of the rapidity of the $t\bar{t}$ system, $|y^{t\bar{t}}|$, for 12 of 14 generated $m_{Z'}$ mass points in linear scale (a) and logarithmic scale (b).

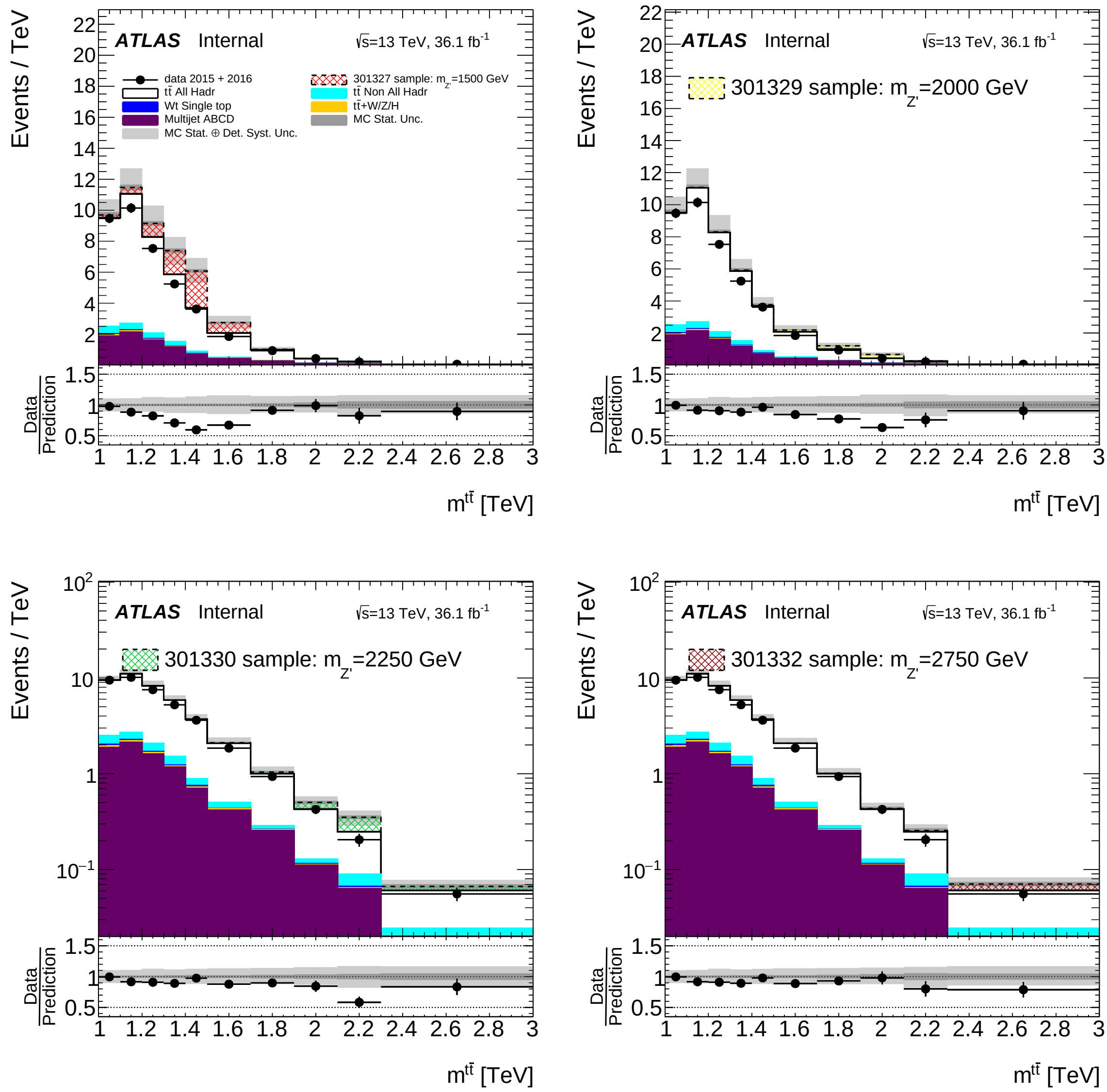

Figure 5.4: Comparison of $t\bar{t}$ mass distributions including a contribution of hypothetical Z' boson with generated mass : $m_{Z'}$ = 1500 GeV (top-left), $m_{Z'}$ = 2000 GeV (top-right), $m_{Z'}$ = 2250 GeV (bottom-left), $m_{Z'}$ = 2750 GeV (bottom-right). All distributions were performed using re-clustered jets and they show spectra at detector level in the signal region of $t\bar{t}$ all hadronic channel. The individual Z' sample is added on top of Standard Model predictions.

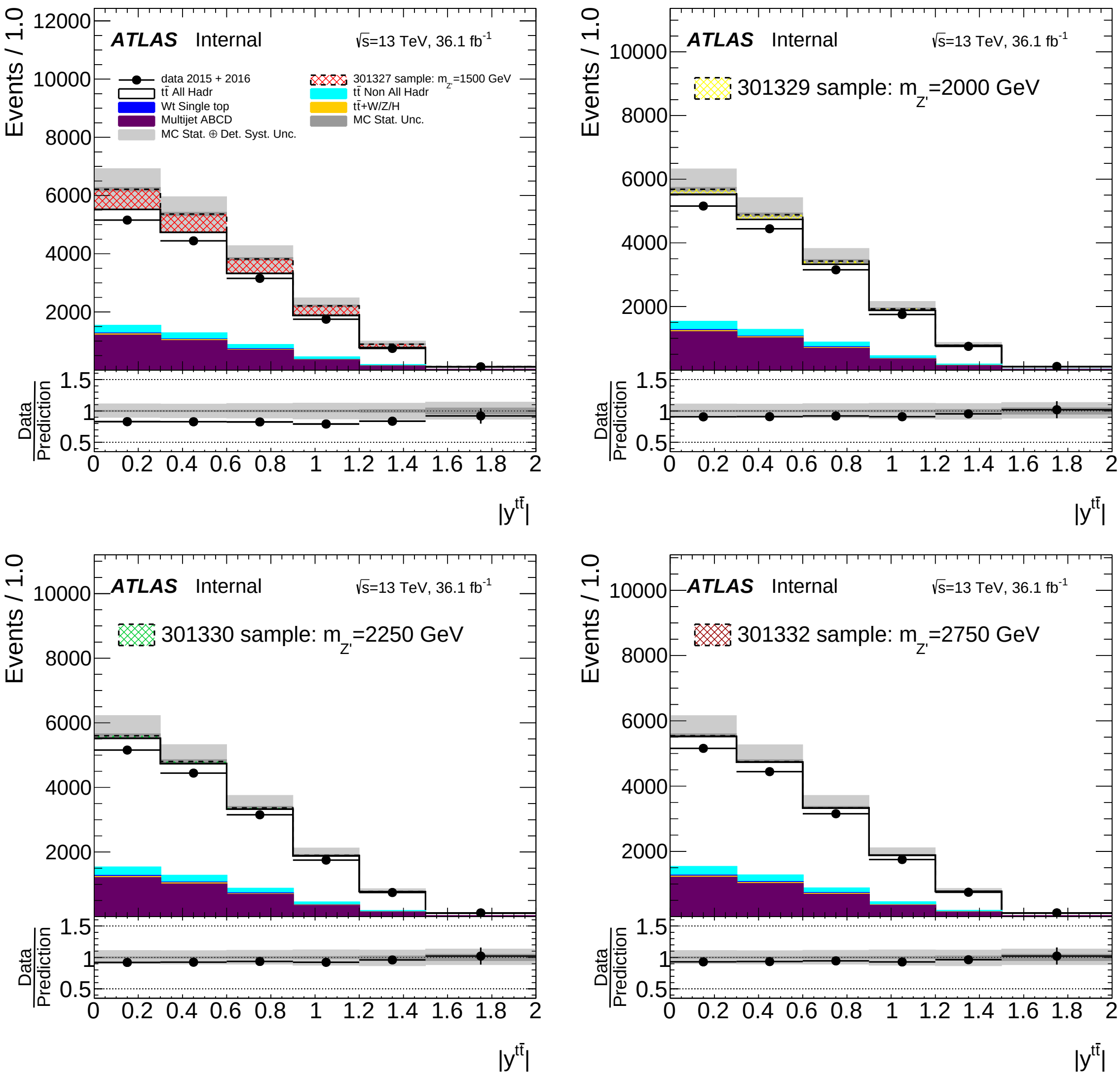

Figure 5.5: Comparison of $t\bar{t}$ rapidity distributions including a contribution of hypothetical Z' boson with generated mass : $m_{Z'}$ = 1500 GeV (top-left), $m_{Z'}$ = 2000 GeV (top-right), $m_{Z'}$ = 2250 GeV (bottom-left), $m_{Z'}$ = 2750 GeV (bottom-right). All distributions were performed using re-clustered jets and they show spectra at detector level in the signal region of $t\bar{t}$ all hadronic channel. The individual Z' sample is added on top of Standard Model predictions.

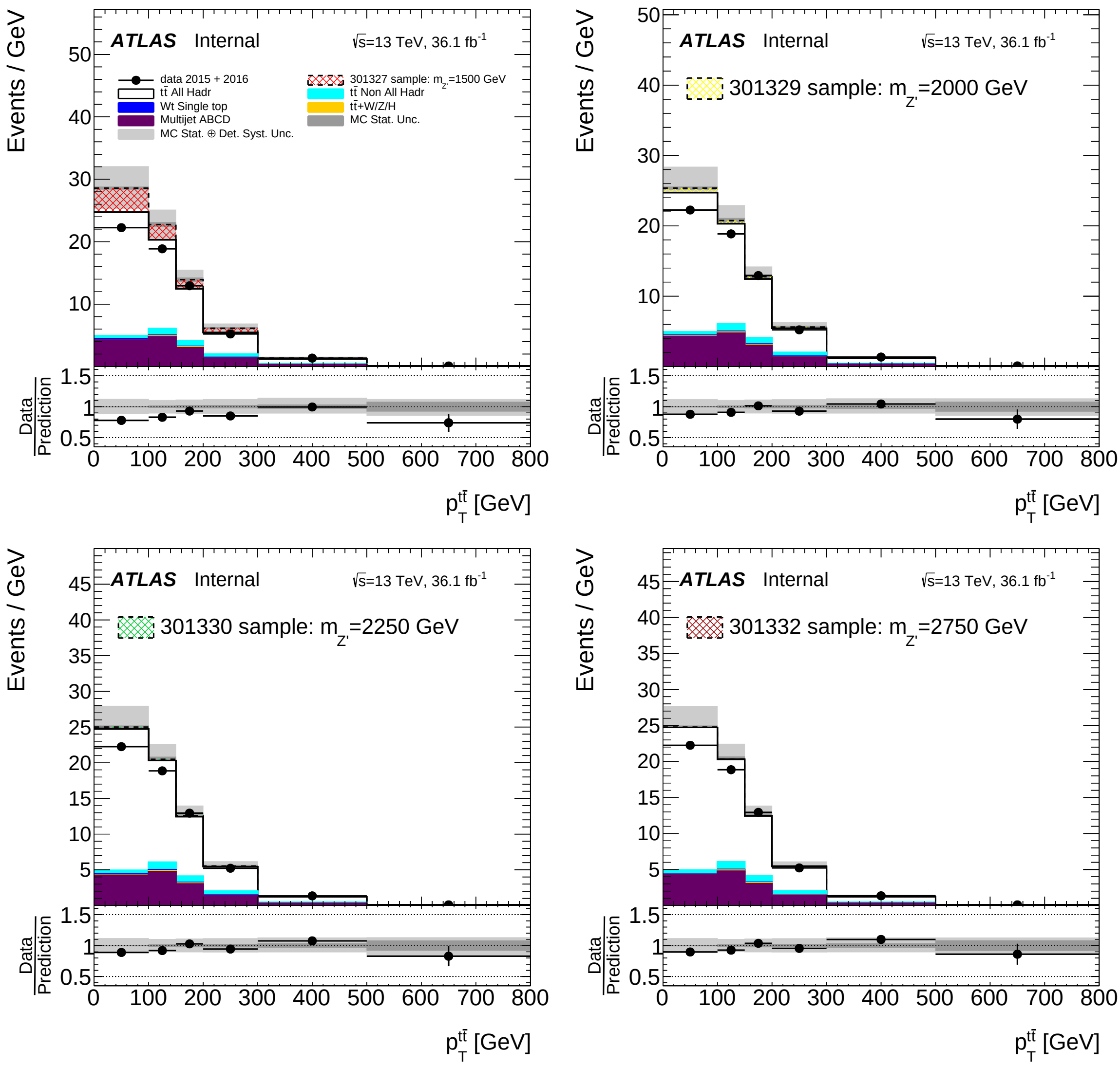

Figure 5.6: Comparison of $t\bar{t}$ transverse momenta distributions including a contribution of hypothetical Z' boson with generated mass : $m_{Z'}$ = 1500 GeV (top-left), $m_{Z'}$ = 2000 GeV (top-right), $m_{Z'}$ = 2250 GeV (bottom-left), $m_{Z'}$ = 2750 GeV (bottom-right). All distributions were performed using re-clustered jets and they show spectra at detector level in the signal region of $t\bar{t}$ all hadronic channel. The individual Z' sample is added on top of Standard Model predictions.

Chapter 6

Summary

The master thesis deals with properties of the top quark and briefly describes the measurement of the $t\bar{t}$ pair production in the so called all-hadronic decay channel at 13 TeV in proton-proton collisions using data collected by the ATLAS experiment at LHC. The measurement is based on the boosted topology when all decay products of the $t\bar{t}$ system can be collected by only two jets with large radii R.

A short theory introduction regarding the top quark was given and also the experimental procedure of the measurement of top quarks decaying fully hadronically was briefly described. Considering the all-hadronic channel, the top quark can not be measured directly but it can be identified using its decay products, quarks, which hadronize subsequently to form the jets. Thus the jets physics becomes essential for the $t\bar{t}$ all-hadronic decay channel. The jets and jet substructure techniques were also discussed together with necessary experimental techniques such as Bayesian unfolding and multijet background estimation.

The thesis briefly describes the $t\bar{t}$ pair analysis, which is based on the framework developed by the working group at the ATLAS experiment called: *Differential ttbar cross-sections at 13 TeV all-hadronic boosted group*. The results published in the note [36] have been reproduced using the ATLAS data from years 2015 and 2016. Then new approach of jet construction, the so called jet re-clustering, was implemented to existing framework to investigate the re-clustered jets and their properties in the $t\bar{t}$ events. The re-clustering method of reconstructing jets with large radii ($R \sim 1.0$) is based on clustering jets with small radii ($R \sim 0.4$) by anti-k_t algorithm. Since the existing framework does not provide full information about the events, and since the top-tagger is not based on re-clustered jets, some modifications of selection criteria had to be done. After performing the whole analysis chain including the event selection, unfolding using smearing matrices and various background estimate techniques, we conclude the following. First the re-clustered jets improve the agreement between the data and prediction. Second the re-clustered jets improve the total systematic uncertainty as well as its dominant part, called jet energy scale, by about 10 – 20 % in all studied variables which are leading and sub-leading jet p_t, rapidity of the $t\bar{t}$ system as well as the azimuthal angle between the leading and sub-leading jets.

We have also studied the prediction of Pythia8 Monte Carlo generator with an implemented signal of New Physics, the Z' boson, embedded as a new term in the SM Lagrangian and which can also decay to the $t\bar{t}$ system. By comparing predictions for 14 mass points in the range 0.4 – 5.0 TeV with data at detector level and in the all-hadronic decay mode, we conclude that none of the relevant mass points in the 1 – 3 TeV mass region studied in this thesis improves a description based on predictions by Standard Model only.

Bibliography

[1] P. Higgs, *Broken Symmetries and the Masses of Gauge Bosons*, Phys. Rev. Lett. 13, (1964).

[2] F. Englert and R. Brout, *Broken Symmetry and the Mass of Gauge Vector Mesons*, Phys.Rev.Lett. 13 (1964) 321-323, (1964).

[3] Particle Data Group, *Particle data book 2012*, Phys. Rev. D86, 010001, (2012).

[4] J. Hořejší, http://www-ucjf.troja.mff.cuni.cz/ horejsi/popular/kvarky.html.

[5] M. Owen, *Top quark properties at the LHC*, arXiv:1705.09089v1 [hep-ex], (2017).

[6] F. Déliot, *Properties of the Top Quark*, arXiv:1803.00656v1 [hep-ex], (2018).

[7] ATLAS Collaboration, *Measurement of the top quark charge in pp collisions at* $\sqrt{s}$ = 7 *TeV with the ATLAS detector*, arXiv:1307.4568 [hep-ex], (2013).

[8] J. Hořejší, *The elementary of the electro-weak interactions*, Prague, (2002).

[9] CDF Collaboration, *Observation of Top Quark Production in* $\bar{p}p$ *Collisions with the Collider Detector at Fermilab*, Phys. Rev. Lett. 74, 2626, (1995).

[10] D0 Collaboration, *Observation of the Top Quark*, Phys. Rev. Lett. 74, 2632, (1995).

[11] K. Kroniger, A.B. Meyer, P. Uwer, *Top-quark physic at the LHC*, arXiv:1506.02800[hep-ex], (2015).

[12] F.P.Schilling, *Top quark physic at the LHC: A review of the first years*, arXiv:1506.4484[hep-ex], (2012).

[13] https://twiki.cern.ch/twiki/bin/view/AtlasProtected/TopWorkingGroup.

[14] J.A. Aguilar-Saavedra et al., Acta. Phys. Polon. B 115, (2004).

[15] Particle Data Group, S. Bethke, G. Dissertori and G. Salam, *Quantum Chromodynamics*, Chin. Phys. C38 (2014) 090001, (2014).

[16] A.D. Martin, W.J. Stirling, R.S. Thorne and G. Watt, *Parton distributions for LHC*, carXiv:0901.0002v3 [hep-ph], (2009).

[17] J. Chýla, A course in the phenomenology of the quark-parton model and Quantum Chromodynamics: *Partons and quarks and an introduction to Quantum Chromodynamics*, https://www.fzu.cz/ chyla/lectures/text.pdf.

[18] C. Luci, presentation: *Introduction to Paricle Physics-Color and QCD*, Sapienza, unitetsitá di Roma, http://www.roma1.infn.it/people/luci/fns/2017/Colour_QCD.pdf, (2017).

[19] CERN, *CERN accelerator complex*, https://bigscience.web.cern.ch/bigscience/en/lhc/lhc2.html, (2018).

[20] ATLAS Collaboration, *Studies of the performance of the ATLAS detector using cosmic-ray muons*, Eur. Phys. J. C 71 (2011) 1593, arXiv:1011.6665v1 [physics.ins-det], (2011).

[21] J. Pequenao, P. Schaffner, *An computer generated image representing how ATLAS detects particles*, CERN-EX-1301009, (2013).

[22] A. Breskin, R. Voss, *The CERN Large Hadron Collider: Accelerator and Experimets*, CERN Geneva 2008 JINST 3 S08001- S08007, (2008).

[23] R. Podškubka, Master thesis: *Production of high pT jets at LHC*, https://is.cuni.cz/webapps/zzp/detail/127861/?lang=en, (2014).

[24] O. Hladík, Master thesis: *Partonic showers and jets*, https://is.cuni.cz/webapps/zzp/detail/104695/?lang=cs, (2013).

[25] G. P. Salam, *Towards Jetography*, arXiv:0906.1833v2 [hep-ph], (2010).

[26] M. Cacciari, G. P. Salam, *The anti-k_t jet clustering algorithm*, arXiv:0802.1189v2 [hep-ph], (2008).

[27] ATLAS Collaboration, *Performance of jet substructure techniques for large-R jets in proton-proton collisions at $\sqrt{s}$ = 7 TeV using the ATLAS detector*, arXiv:1306.4945v [hep-ex], (2013).

[28] T. Herrmann, Master thesis: *Study of Different Unfolding Methods of Kinematic Distributions of the $WZ \to WZ$ Scattering with Data and Simulations of the ATLAS Detector at the LHC*, CERN-THESIS-2017-053, (2017).

[29] M. Cacciari and G. P. Salam, *Pileup subtraction using jet areas*, arXiv:0707.1378 [hep-ph], (2008).

[30] ATLAS Collaboration, *Jet Re-clustering in ATLAS*, ATL-COM-PHYS-2014-1117, (2014).

[31] J. Heinrich, *Reconstruction of boosted $W^{\pm}$ and Z^0 bosons from fat jets*, CERN-THESIS-2014-152, (2014).

[32] ATLAS Collaboration, *Search for dark matter in events with a hadronically decaying W or Z boson and missing transverse momentum in pp collisions at $\sqrt{(s)} = 8$ TeV with the ATLAS detector*, arXiv:1309.4017 [hep-ex], (2014).

[33] J. M. Butterworth et al., *Jet substructure as a new Higgs search channel at the LHC*, Phys. Rev. Lett. 100 (2008) 242001, arXiv:0802.2470 [hep-ph], (2008).

[34] ATLAS Collaboration, *Expected performance of the ATLAS b-tagging algorithms in Run-2* ATL-PHYS-PUB-2015-022, (2015).

[35] ATLAS Collaboration, *Performance and calibration of b-tagging with the ATLAS experiment at LHC Run-2*, EPJ Web of Conferences 164, 07025, (2017).

[36] ATLAS Collaboration, *Measurements of $t\bar{t}$ differential cross-sections in the all-hadronic channel with the ATLAS detector using highly boosted top quarks in pp collisions at $\sqrt{s} = 13$ TeV with the full 2015+2016 dataset*, ATL-COM-PHYS-2016-1696, (2017).

[37] J. Thaler, K. V. Tilburg, *Identifying Boosted Objects with N-subjettiness*, arXiv:1011.2268v3 [hep-ph], (2011).

[38] ATLAS Collaboration, *Measurement of the inclusive jet cross-section in proton-proton collisions at $\sqrt{s} = 7$ TeV using 4.5 fb^{-1} of data with the ATLAS detector*, arXiv: 1410.8857 [hep-ex] (2015).

[39] ATLAS Collaboration, *ATLAS measurements of the properties of jets for boosted particle searches*, Phys. Rev. D 86 (2012) 072006, arXiv: 1206.5369 [hep-ex] (2012).

[40] J. Hejbal, R. Lysak, *Close-by jets studies in multijet events*, ATL-COM-PHYS-2017-067, (2017).

[41] O. Zaplatilek, Research task: *Preparation for a measurement of jets with various radii at the ATLAS experiment*, https://physics.fjfi.cvut.cz/publications/ejcf/VU_Ota_Zaplatilek.pdf (2017).

[42] ATLAS Collaboration, *Measurements of top quark pair relative differential cross-sections with ATLAS in pp collisions at $\sqrt{s=7}$ TeV*, Eur. Phys. J. C 73 (2013) 2261, arXiv: 1207.5644 [hep-ex], (2013).

[43] ATLAS Collaboration, *Measurements of normalized differential cross-sections for ttbar production in pp collisions at $\sqrt{s} = 7$ TeV using the ATLAS detector*, Phys. Rev. D 90 (2014) 072004, arXiv: 1407.0371 [hep-ex], (2014).

[44] ATLAS Collaboration, *Differential top-antitop cross-section measurements as a function of observables constructed from final-state particles using pp collisions at $\sqrt{s} = 7$ TeV in the ATLAS detector*, JHEP 06 (2015) 100, arXiv: 1502.05923 [hep-ex], (2015).

[45] ATLAS Collaboration, *Measurements of top-quark pair differential cross-sections in the lepton+jets channel in pp collisions at $\sqrt{s} = 8$ TeV using the ATLAS detector*, arXiv: 1511.04716[hep-ex], (2015).

[46] CMS Collaboration, *Measurement of differential top-quark-pair production cross sections in pp collisions at $\sqrt{s} = 7$ TeV*, Eur. Phys. J. C 73 (2013) 2339, arXiv: 1211.2220 [hep-ex], (2013).

[47] CMS Collaboration, *Measurement of the differential cross section for top quark pair production in pp collisions at $\sqrt{s} = 8$ TeV*, arXiv: 1505.04480 [hep-ex], (2015).

[48] ATLAS Collaboration, *Search for resonances decaying into top-quark pairs using fully hadronic decays in pp collisions with ATLAS at $\sqrt{s} = 7$ TeV*, arXiv: 1211.2202 [hep-ex], (2013).

[49] S. Agostinelli et al., *GEANT4: a simulation toolkit*, Phys. A 506 (2003) 250, CERN-IT-2002-003, (2002).

[50] P. Jačka, Master thesis: *Measurement of the kinematic properties of top-antitop pairs*, (2016).

[51] H. B. Prosper and L. Lyons, Proceedings, *PHYSTAT 2011 Workshop on Statistical Issues Related to Discovery Claims in Search Experiments and Unfolding* (p. 313-318), (2011).

[52] M. Cacciari, G. P. Salam and G. Soyez, *The Catchment Area of Jets*, JHEP 04 (2008) 005, arXiv: 0802.1188 [hep-ph], (2008).

[53] ATLAS Collaboration, *Jet Calibration and Systematic Uncertainties for Jets Reconstructed in the ATLAS Detector at $\sqrt{s} = 13$ TeV*, ATL-PHYS-PUB-2015-015, (2015).

[54] ATLAS Collaboration, *Jet energy measurement and its systematic uncertainty in proton-proton collisions at $\sqrt{s} = 7$ TeV with the ATLAS detector*, Eur. Phys. J. C75 (2015) 17, arXiv: 1406.0076 [hep-ex], (2015).

[55] ATLAS Collaboration, *Jet energy measurement with the ATLAS detector in proton-proton collisions at $\sqrt{s} = 7$ TeV*, Eur. Phys. J. C 73 (2013) 2304, arXiv: 1112.6426 [hep-ex], (2013).

[56] ATLAS Collaboration, *Single hadron response measurement and calorimeter jet energy scale uncertainty with the ATLAS detector at the LHC*, Eur. Phys. J. C73 (2013) 2305, arXiv: 1203.1302 [hep-ex], (2013).

[57] ATLAS Collaboration, *Jet energy resolution in proton-proton collisions at* $\sqrt{s} = 7$ *TeV recorded in 2010 with the ATLAS detector*, arXiv: 1210.6210 [hep-ex], (2013).

[58] ATLAS Collaboration, *Optimization of the ATLAS b-tagging performance for the 2016 LHC run*, ATL-PHYS-PUB-2016-012, (2016).

[59] ATLAS Collaboration, *Calibration of b-tagging using dileptonic top pair events in a combinatorial likelihood approach with the ATLAS experiment*, ATLAS-CONF-2014-004, (2014).

[60] ATLAS Collaboration, *Measurement of the b-tag Efficiency in a Sample of Jets Containing Muons with* 5 fb^{-1} *of Data from the ATLAS Detector*, ATLAS-CONF-2012-043, (2012).

[61] ATLAS Collaboration, *Measurement of the Mistag Rate of b-tagging algorithms with* 5 fb^{-1} *of Data Collected by the ATLAS Detector*, ATLAS-CONF-2012-040, (2012).

[62] Arguin, J. F. et al., *Measurement of the top-antitop pair differential fiducial cross-section as a function of the top quark* p_T *in the boosted topology*, ATL-COM-PHYS-2013-1093, (2015).

[63] M. Cacciari, G. P. Salam and G. Soyez, *FastJet user manual*, Eur. Phys. J. C **72** (2012) 1896 [arXiv:1111.6097 [hep-ph]], (2012).

[64] C.S. Kim, Xing-Bo Yuan, Ya-Juan Zheng *Constraints on Z′ Boson within Minimal Flavor Violation*, arXiv:1602.08107v2 [hep-ph], (2016).

[65] P. Langacker, *The Physics of Heavy Z' Gauge Bosons*, arXiv:0801.1345 [hep-ph], (2009).